Discrete-Dipole-Approximation (DDA) study of the plasmon resonance in single and coupled spherical silver nanoparticles in various configurations

Mamoun Wahbeh

A Thesis

in

The Department

of

Physics

Presented in Partial Fulfillment of the Requirements

for the Degree of Master of science at

Concordia University

Montreal, Quebec, Canada

November 2011

CONCORDIA UNIVERSITY

School of Graduate Studies

This is to certify that the thesis prepared

By: Mamoun Wahbeh

Entitled: Discrete-Dipole-Approximation (DDA) study of the dipole plasmon resonance in single and coupled spherical silver nanoparticles in various configurations

and submitted in partial fulfillment of the requirements for the degree of

Master of Science

complies with the regulations of the University and meets the accepted standards with respect to originality and quality.

Signed by the final Examining Committee:

Prof. Truong Vo-Van	Chair
Prof. Mojtaba Kahrizi	Examiner
Prof. Laszlo Kalman	Examiner
Prof. Truong Vo-Van	Supervisor
Prof. Sushil K. Misra	Supervisor

Approved by Prof. Truong Vo-Van

Chair of Department or Graduate Program Director

December 13th 2011 Prof. Brian Lewis

Dean of Faculty

ABSTRACT

Discrete-Dipole-Approximation (DDA) study of the plasmon resonance in single and coupled spherical silver nanoparticles in various configurations

Mamoun Wahbeh

Using the Discrete-Dipole-Approximation (DDA) the influence of the substrate on the dipole and multipolar plasmon resonances in spherical and sphere-like silver nanoparticles has been studied in depth. The effects of the contact area, the substrate material, the substrate thickness, the surrounding environment and the particle size on the plasmon resonance bands have been examined.

We studied in particular the validity of extending the so-called "universal scaling law", derived for a pair of particles in previous works, to a linear chain of any size consisting of silver nanospheres. Details of the variation of the dipole plasmon resonance parameters with component particle size, interparticle separation and host medium, under parallel and perpendicular polarization directions of the incident light, have been studied in a systematic way. In a two-dimensional array of silver nanospheres, the interparticle separation dependency of the maximum absorption cross-section is presented. The variation of the absorption efficiency has been also investigated as a function of the component particle size and the surrounding medium. The effect of the host medium on the absorption cross-section has been found to be dependent on the component particle size. The sensitivity of the longitudinal dipole plasmon resonance wavelength to the refractive index of the host medium and the component sphere radius has been also expressed as a function of the interparticle separation.

Finally, the effect of the direct neighboring particles on the optical responses has been studied for various ensemble configurations, which can be arranged in two-dimensional or three-dimensional arrays.

ACKNOWLEDGMENTS

I would like to express my sincerest gratitude to my supervisor Prof. Truong Vo-Van, whose patience and kindness have been invaluable to me, without whom none of this work would have been accomplished. He has supported me throughout my work with his time, knowledge, expertise and advice.

I would like to gratefully acknowledge Damascus University for its financial support throughout my Master's degree.

I also wish to thank my supervisor Prof. Sushil K. Misra for allowing me the room to work in my own way. I am grateful to him for introducing me to the program with warm greetings.

I want to thank all of my group members especially; Mohammed Alsawafta for his willingness to discuss any topic and his good company, with whom I studied the plasmon resonance of many metallic nanostructures, Alaa Mahmoud for her encouragement and sharing the literature.

I would like to thank Dr. Denise Koch who arranged an effective way to provide me with access to CERMM facilities. I also wish to thank Wentworth Brookes for his technical support and introducing me to the SSH connection.

I thank B. T. Draine and P. J. Flatau for the free DDSCAT 7.1 code.

My special thanks to my wife Nivine for her endless love and priceless support.

Above all, I am more thankful than I can express to my parents for their spiritual care and prayers helping me through all times.

DEDICATION

TO MY PARENTS, TO THE FREE SPIRITS AND THE BRAVE SOULS IN SYRIA.

TABLE OF CONTENTS

TABLE OF FIGURES

TABLE OF SYMBOLS

C_{abs}	**absorption cross-section**
Q_{abs}	absorption efficiency factor
ω_p	bulk plasma frequency
ε	complex dielectric constant of the particle
S	contact area
R_0	critical radius
γ_0	damping constant (relaxation constant)
b	decay constant
T	dephasing time
l	depolarization factor
μ	dipole moment
λ_0	dipole plasmon resonance wavelength in single particles
m_e	effective mass of the electron
L_{eff}	effective mean free path of conduction electrons
a_{eff}	effective radius
λ_{eff}	effective wavelength
C_{ext}	extinction cross-section
Q_{ext}	extinction efficiency factor
v_F	Fermi velocity of conduction electrons
ω	frequency

h	height of the sphere-like particle
ε_∞	high frequency part of metal dielectric function
$\varepsilon_2(\omega)$	imaginary part of the metal dielectric function
φ	incident angle
d	interdipole separation
D	interparticle separation (spacing)
l_∞	mean free path of conduction electrons in the bulk
ε_m	medium dielectric constant
N	number of dipoles
N_{surf}	number of surface dipoles
R_{opt}	optimum radius
ε_0	permittivity of vacuum
ω_{sp}	plasmon resonance frequency
α	polarizability
p	polarization
$\varepsilon_1(\omega)$	real part of the metal dielectric function
λ_{res}	resonance wavelength
C_{sca}	scattering cross-section
Q_{sca}	scattering efficiency factor
R	sphere radius
λ	wavelength
k	wavenumber

CHAPTER 1

Introduction

The surface plasmon resonance, resulting from the interaction between light and metallic nano-sized particles, forms the basis of the unique optical properties of the nanoparticles assemblies whether in one, two or three dimensional arrays [1,2]. These properties have found uses in diverse applications, depending on the plasmon resonance parameters: resonance frequency, plasmon bandwidth, extinction cross-section and plasmon mode. It is now well established that many influential factors on the plasmon resonance phenomenon would include the particle size, the metal type, the particle shape, the host medium and the polarization direction of the incident light. Manipulating these factors is crucial to advancing nanotechnology research. A better understanding of the optical properties of noble-metals aggregates can be used to achieve new material responses, which can be of great interest in different applications.

In this thesis, the discrete dipole approximation (DDA) is used as a powerful and reliable tool to study the optical properties of isolated and coupled targets, which are revealed by the calculated plasmon resonance parameters. The major advantages of the DDSCAT, the implementation of the DDA, in simulating single targets of arbitrary shapes and assemblies of interacting nanoparticles have been exploited to illustrate the substrate effect on optical response of supported particles, and to study the plasmon coupling

arising between interacting metallic nanoparticles, arranged successively in one-dimensional, two-dimensional and three-dimensional arrays.

1.1 Background and objectives of the present study

The substrate effect on the plasmon resonance in isolated silver nanoparticles, placed at different distances from the substrate, was investigated by Noguez and co-workers [3] with the inclusion of multipolar plasmon resonance mode, especially when the substrate is in close contact with the particle. The DDA was used by Malinsky et al. [4] to qualitatively study the dependency of the resonance wavelength on the refractive index of the substrate, which supports a silver truncated tetrahedron. Yang et al. [5] used the DDA to investigate the influence of a MgO substrate on the optical properties of triangular silver nanoprisms.

In this thesis, we propose a more systematic study of the substrate effect on the plasmon resonances in small spherical and sphere-like silver nanoparticles. The optical properties of such nanoparticles are affected by the bonding between the substrate and the particles. The multipolar plasmon modes are studied for different combined substrate and silver-particle targets, characterized by different contact areas. These targets are simulated in different surrounding environments. The sensitivities of the dipole and multipolar plasmon resonance wavelengths to the refractive index of the host medium are investigated, when the refractive index of the host medium, n_{medium}, is either greater or lesser than the refractive index of the of the substrate $n_{substrate}$.

The plasmon parameters of metallic nanoparticle ensembles have been found to strongly depend on the interparticle separation and the polarization direction [6,7,8,9] . The dependency of the plasmon coupling parameters on interparticle spacing was experimentally clarified by the plasmon spectra of nanodisc pairs, fabricated by Huang et al. [10]. In this work, the plasmon resonance wavelength of a linear chain is observed to red-shift near-exponentially with decreasing interparticle separation, for incident polarization parallel to the chain axis. This shift was expressed by the fractional plasmon shift in a system of nanoparticle pairs leading to the **universal scaling behaviour** reported by Jain et al. [10,11]. The universal scaling behaviour supposes that the fractional plasmon shift decays near-exponentially over a spacing between the pair particles, which is roughly 0.2 in units of the particle size. The universality relies on the fact that the decay constant is independent from the nanoparticle size, metal type, shape or the host medium. Consequently, the "plasmon ruler equation", proposed by Jain et al. [10], was used to evaluate the spacing between a pair of interacting particle from their measured plasmon shift, deviated from the resonance wavelength of a single component particle. The universal scaling behaviour has been successfully applied to a trimer of nanospheres by Jain et al. [12]. In this work, we examined the validity of extending this universal scaling law to a linear chain of any size consisting of identical silver nanospheres. While the universal scaling behaviour was found to be independent from the nanoparticle size [10], our calculations reveal that the magnitude of the plasmon shift is found to be dependent on the component sphere diameter and slightly on the refractive index of the host medium. We also present the details of the variation of the dipole plasmon parameters with component particle size and host medium, respectively, as a

function of the interparticle separation in units of sphere diameter, for incident polarization parallel and perpendicular to the chain axis. In order to perform the required calculations, the absorption spectra of linear silver chains consisting of identical spheres at various interparticle separations are simulated i) for component sphere radii extending from 2nm to 15nm, and embedded in a specific host medium, and ii) for a specific component sphere radius immersed in different host media.

Finally to complete our research work, we extend the DDA simulations to two-dimensional as well as three-dimensional arrays of nanoparticles and discuss their optical responses in the light of the numerous factors discussed earlier. We believe that the present work presents a more comprehensive picture of nanoparticle arrays than previous studies, and it will permit a better appreciation of the behaviour of experimental arrangements of these plasmonic nanoparticles.

1.2 Organization of the thesis

The thesis is divided into nine chapters.

Chapter 2: Plasmon resonance in metallic nanoparticles

The origin of the plasmon resonance in the metallic nanostructures exhibiting unique optical properties is explained. Dependency of the plasmon resonance parameters on metal type, size, shape and environment, and plasmon coupling observed in assemblies of nanoparticles are presented.

Chapter 3: The discrete dipole approximation

The discrete dipole approximation method is presented as a methodology to solve the electromagnetic scattering problem of an incident periodic wave, which interacts with an array of point dipoles composing the target. A Fortran implementation of the DDA is presented. The input files required and the output files produced are explained. The memory and CPU requirements are discussed and other computational considerations are also defined.

Chapter 4: The size-corrected dielectric function and the effect of the host medium on the optical properties of isolated spherical silver nanoparticles

The complex dielectric functions, which represent the physical properties of the plasmonic nanoparticles perfectly, are derived from the bulk dielectric functions by exploiting the Drude model. The imaginary and real parts of the size-corrected bulk dielectric function are plotted and their dependency on the host medium is illustrated. The effect of the host medium on isolated silver spheres of various radii is studied. Their resonance wavelengths will be used as a reference to calculate the plasmon shift of coupled particles, studied in next chapters. The sensitivity of the dipole plasmon resonance shift to the particle size as a function of the refractive index of the host medium is extracted.

Chapter 5: Optical properties of supported sphere-like silver nanoparticles in different host media

The substrate effect on plasmon resonances in sphere and sphere-like particles is investigated with changing contact area, substrate material, substrate thickness,

surrounding environment and particle size. The variation of the plasmon resonances, due to the substrate existence, with the contrast between the refractive indices of the host medium and the substrate is studied in a systematic way.

Chapter 6: Host medium effect on the dipole plasmon coupling resonance in silver linear chains

The optical properties, characterized by plasmon resonance parameters, of a linear chain of any size consisting of identical silver nanospheres are estimated. Silver linear chains, composed of spheres of radius $R = 8nm$, arranged at various interparticle separations covering the near-field and far-field regions, are simulated in different host media. The details of the variation of dipole plasmon parameters with the host medium are consequently induced. Plasmon resonance sensitivity and fractional plasmon shift are determined as functions of the interparticle separation in units of component sphere diameter. Under oblique polarization, two distinct plasmon peaks, attributed respectively to the longitudinal and the transverse plasmon bands, are investigated as functions of the interparticle separation in different host media.

Chapter 7: Component particle size effect on the dipole plasmon coupling resonance in silver linear chains

The sensitivity of the plasmon resonance wavelength, observed in a silver linear chain embedded in PDMS of refractive index n=1.46, to the component sphere radius extending from 2nm to 15nm is evaluated under parallel and perpendicular polarizations. It is also plotted as a function of the interparticle separation in units of sphere diameter. The

plasmon resonance bandwidth is plotted as a function of the component sphere radius when the interparticle separation ranges between $D = R/8$ and $D = 2R$.

Chapter 8: Particles configuration effect on the dipole plasmon coupling resonance in interacting silver nanoparticles

The dependency of the dipole plasmon coupling resonances (longitudinal and transverse) on the configuration of particles, arranged in two and three-dimensional arrays, is clarified by the absorption plasmon spectra, when the targets are composed of identical ultrafine silver spheres.

Planar arrays consisting of 36 identical silver nanospheres, uniformly arranged in square areas at various interparticle separations are simulated under parallel polarization: i) in different host media when the component sphere radius is set to $R = 6nm$, ii) in a host medium of refractive index $n = 1.66$ while the component sphere radius increases from 2nm to 14nm. The sensitivity of the longitudinal dipole plasmon resonance wavelength to the refractive index of the host medium and to the component sphere radius are extracted as functions of interparticle separation in units of sphere diameter.

Optical responses of various configurations of nanoparticle ensembles are studied to detect the effect of the direct neighboring particles, which are arranged in two and three-dimensional arrays.

Chapter 9: Conclusions

The main features of the present work are described along with the most interesting conclusions.

CHAPTER 2

Plasmon resonance in metallic nanoparticles

Metal nanostructures exhibit unique aspects of optical properties due to their interaction with light. These optical properties are mainly attributed to the motion of the conduction electrons confined to nanometer length scale. They depend strongly on the metal type, the size and shape of the nanostructure, and the dielectric environment.

2.1 Plasmon resonance

The interaction between the incident electromagnetic waves and nanoparticles can be illustrated by an irradiated sphere that had been studied by G. Mie in 1908 [13]. The exact solution of Maxwell's electrodynamic equations in the presence of a spherical particle was presented. The scattering of electromagnetic waves surrounding the surface of the sphere were also calculated to many orders, ranging from the lower dipolar order to higher multipolar orders, according to the relative size (diameter) of the sphere as compared to the wavelength of light.

If an isolated metallic nanosphere of radius ($2.5 \le R \le 15\,\text{nm}$) is irradiated by a plane electromagnetic wave propagating in the x direction, with wave vector $\vec{k} = \sqrt{\varepsilon_m}\,\frac{2\pi}{\lambda}\hat{x}$ where λ is the wavelength of the incident light, then one can assume that the electric field component of the incident light is constant across the volume of the sphere since $R \ll \lambda$, but with a time dependent phase, according to the quasi-static approximation.

The scattering electric field is radiated in the dipolar mode as the electric field alternatively polarizes the tiny sphere. The polarization of the sphere P is related to the electric field (Eq. 1) by the Clausius-Mossotti relation expressing the static polarizability α (Eq. 2) that can be written as follows [14]

$$P = \varepsilon_m \alpha E_0 \tag{1}$$

$$\alpha = 4\pi R^3 \varepsilon_0 \frac{\varepsilon - \varepsilon_m}{\varepsilon + 2\varepsilon_m} \tag{2}$$

where ε_0 is the permittivity of vacuum , ε_m is the dielectric constant of the host medium and ε is the complex dielectric constant of the metal composing the sphere, which is energy dependent on the incident light and conventionally appended by frequency ω

$$\varepsilon(\omega) = \varepsilon_1(\omega) + i\,\varepsilon_2(\omega) \tag{3}$$

where $\varepsilon_1(\omega)$ is the real part and $\varepsilon_2(\omega)$ is the imaginary part of the dielectric constant.

The maximum polarizability can be deduced from Eq. 2 to be

$$\varepsilon_1(\omega) = -2\varepsilon_m(\omega) \tag{4}$$

A negative value of the real part of dielectric function is required to satisfy this condition, which is the case for the complex dielectric functions of some metals. On the other hand, the real part $\varepsilon_1(\omega)$ is frequency dependent. Consequently, the condition expressed in Eq. 4 is valid at a specific frequency ω_{sp} of the incident light, at which the maximum polarizability is achieved as a response of the applied electric field. The frequency ω_{sp}

reflects an intense interaction between light and the matter forming the nanosphere; such a strong interaction imposes collective coherent oscillations upon the conduction electrons. This oscillating coherent motion is called plasmon resonance or localized surface plasmon resonance, and ω_{sp} is known as a plasmon frequency.

As a result of the plasmon resonance, an enhanced strong electric field is induced, called the local field. It locates on the surface of the sphere and extends to the surrounding region, known as near-field region, defined by a distance comparable to the radius of the metallic nanosphere.

According to the well-known Rayleigh diffraction limit, a particle with a size smaller than the wavelength of the incident light cannot confine the light. However, the volume containing the near-field is much smaller than the value of the diffraction limit as $R \ll \lambda$; plasmon oscillations on the surface of metallic nanoparticles can be thus considered as confined to a nano-sized lens of aperture $2R$. Eventually, the plasmon resonance is a phenomenon that provides the ability of the confinement of light to metallic nanostructures that possess a large enhancement of the light extinction cross-section. The absorption and scattering cross-sections are affected by the plasmon resonance mode ranging from the lower dipolar to higher multipolar modes, giving rise to various optical responses.

2.1.1 Dipole plasmon resonance

The dipolar mode of plasmon resonance is mainly involved in relatively small nanoparticles with size of a few ten nanometres, such as the case with spherical silver and gold particles with a radius less than 15nm.

In a system of such metal nanoparticles, the conduction (free) electrons are governed by the alternating electric field and forced to transiently move away from the metal particle relative to the immobile background of positive ions, creating a dipole that is driven to switch direction with a frequency that follows the change of the incident alternating electric field and by the restoring force, due to the Coulomb attraction between the oscillating electrons and localized positive ions. When both frequencies of the dipole ω_{sp} and the incident light are equal, the resonance condition defined in Eq. 4 is satisfied, the conduction electrons oscillations are constructively interfered with light, and the **dipole plasmon resonance** occurs as it is schematically illustrated in Figure 1.

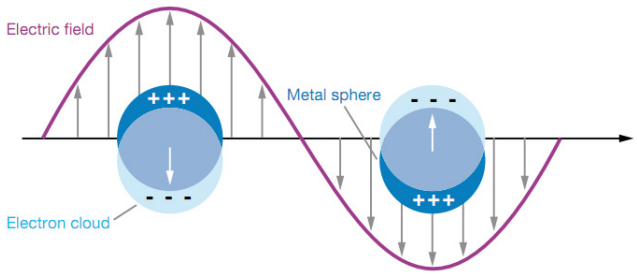

Figure 1| The electric field pushes the free electrons away from a positive metallic nanoparticle composing oscillating electronic cloud due to the Coulombic restoring force at the incident field frequency. When the incident light frequency and ω_{sp} are equal, the resonance condition is satisfied. Reproduced from ref. [15].

The energy of electromagnetic wave is transformed by the plasmon resonance mechanism to the **absorption** process, and then the **scattering** process could be achieved by the accelerated oscillating electrons that radiate the energy in all directions. Both of these processes together are incorporated in the so-called light extinction process. Subsequently, the extinction cross-section refers to the total electromagnetic power penetrating the surface of the nanoparticle, and defined as

$$C_{ext} = C_{abs} + C_{sca} \tag{5}$$

The extinction cross-section is related to the dipolar polarizability as [16]

$$C_{ext} = k\ \mathrm{Im}(\alpha) \tag{6}$$

where $k = \frac{2\pi\sqrt{\varepsilon_m}}{\lambda}$ is the wavenumber.

The scattering cross-section is given as a function of the polarizability α and the incident wavelength in Eq. 7

$$C_{sca} = \frac{k^4}{6\pi}|\alpha|^2 \tag{7}$$

2.1.2 Quadrupole plasmon resonance

The next higher plasmon mode is the quadrupole excitation, which is observed in larger particles than that exhibit the dipole plasmon resonance. It occurs when the electronic cloud motion is equally divided into two directions; parallel and antiparallel to the

external electric field [16], consequently, two negative poles and two positive poles emerge at the surface of a spherical nanoparticle as can be seen in Figure 4.

2.2 Other absorption and scattering mechanisms

Intraband transitions refer to electronic excitation within the conduction band (s-band) of metal nanoparticles, absorbing the light energy by the plasmon resonance. Besides the plasmon resonance, there is also another absorption mechanism, called **interband transitions**, based on the excitation of the electrons, which are energetically in a deeper position (d-band), from occupied to empty bulk bands [17], where each electron is bound by the energy difference between these two bands. However, this absorbing process does not have any contribution in supporting the collective motion of oscillating electrons at plasmon frequency [18].

For particles smaller than ca. 10nm, the interband transitions and the plasmon resonance band are located at the same spectral region for gold and copper nanoparticle, making the analysis more complicated. In these cases, the plasmon resonance bandwidth in absorption spectra may be attributed partially to the effect of interband transitions. However, for metals such as silver and aluminum, the peak position of the interband is well separated from the plasmon band positions [19]. As the absorption of the incident light in the spectral region below 320nm is mainly attributed to the interband transitions, the line profiles of the spectra in this vicinity is quite independent of the shape and size of the silver particles [20].

The plasmon oscillations are exposed to damping processes. In order to shed light on these mechanisms we can consider, from energy perspective, the collective oscillations as

plasmon population, thus damping processes will represent pathways to population decay [21]. The damping processes are characterized according to their nature: **radiative** and **nonradiative** decays. The aforementioned scattering process radiates photons in all directions producing the radiative decay, while nonradiative decay is attributed to the energy dissipated through the collective electronic motion. Dissipating mechanisms involve additional damping processes such as that due to the collisions with phonons of the lattice. The damping constant γ_0 is mainly expressed by the lifetimes of all scattering processes of the conduction electrons in the bulk material, which are electron-electron, electron-phonon and electron-defect collisions. Eventually, the damping constant is given by Mathiessen's rule as a sum of reciprocal relaxation times [22,23]

$$\gamma_0 = \frac{1}{\tau_{e-e}} + \frac{1}{\tau_{e-ph}} + \frac{1}{\tau_d} \tag{8}$$

Let l_∞ designates the mean free path of the conduction electrons in the bulk. l_∞ is related to γ_0 by

$$\gamma_0 = \frac{v_F}{l_\infty} \tag{9}$$

where v_F is the Fermi velocity of conduction electrons.

For small nano-sized particles ($R \leq 10\,\text{nm}$), the finite surface tries to restrict the electrons motion to its boundaries, which gives rise to an additional electron scattering process, known as **electron-surface scattering** or **surface dispersion**, due to the collisions between the particle surface and electrons, when their mean-free-path is greater or comparable to the size of metal nanoparticles. This process is not observed in large

nanoparticles, but it has a significant effect in small nanoparticles. The electron-surface scattering should be added to the damping constant γ_0, and the overall damping constant is then given as

$$\gamma = \gamma_0 + \frac{v_F}{L_{eff}} \tag{10}$$

L_{eff} is the effective distance or effective mean free path of the conduction electrons

$$L_{eff} = \frac{R}{A} \tag{11}$$

where R stands for the particle size (sphere radius), and A is a dimensionless factor that relies on how the electron-surface scattering is modeled and also on the shape of the particle [24]. The dephasing time T could thus be written as [25]

$$T = \frac{2\hbar}{\gamma} \tag{12}$$

Where $h = 2\pi\hbar$ is Planck's constant.

Consequently, electron-surface scattering results in broadening of the plasmon resonance band and decreasing of the absorption cross-section of small nanoparticles [18].

2.3 Plasmon resonance dependency

The plasmon resonance strongly depends on a number of factors, by which the optical response of a metallic nanoparticle is characterized. These factors are:

- Material: a metal from which nanoparticles are composed.

- Geometry: nanoparticles either can be designed in a simple shape or can grow as unspecified aggregates gathered together.
- Size: the plasmon resonance is excited by the lower dipolar or multipolar modes, depending on the particle size.
- Environment: nanoparticles can be distributed in a liquid, injected in a solid embedding material, deposited on a substrate substance, filled by dielectric cores or covered by multi-shells.

Manipulating one or more of those factors, we can tune the plasmon resonance parameters, i.e., resonance wavelength, plasmon bandwidth, intensity of the plasmon band (extinction efficiency) and plasmon mode (dipole or multipolar modes), according to desired patterns that can be utilized in a wide variety of applications. Each factor will be discussed in the following sections.

2.3.1 Material

Copper, silver and gold are all noble metals that belong to the eleventh group of the periodic table. These three elements have filled d-subshells, and a single valence electron in the half -filled s-subshells. The electronic configurations of these elements in order of increasing energy of the subshells are:

Copper (Cu) $1s^2\ 2s^2\ 2p^6\ 3s^2\ 3p^6\ \mathbf{4s^1}\ 3d^{10}$

Silver (Ag) $1s^2\ 2s^2\ 2p^6\ 3s^2\ 3p^6\ 4s^2\ 3d^{10}\ 4p^6\ \mathbf{5s^1}\ 4d^{10}$

Gold (Au) $1s^2\ 2s^2\ 2p^6\ 3s^2\ 3p^6\ 4s^2\ 3d^{10}\ 4p^6\ 5s^2\ 4d^{10}5p^6\ \mathbf{6s^1}\ 4f^{14}\ 5d^{10}$

The electrons in the deeper completely filled levels are called inert gas configuration. The metallic properties of these three elements are thus attributed to the valence electron in the half -filled s-subshells.

The physical and chemical properties of a substance can be characterized by the type of motion that can be performed by its electrons [26]. The plasmon resonance in metallic nanostructures is governed by the density of the oscillating electrons within the conduction band, (Eq. 18). This density varies depending on the metal. Moreover, the electronic motion, from plasmon resonance perspective, can be determined by the dielectric function of the metal, which is defined as a measure of energy storage due to charge accumulations in response to the applied alternating field and, consequently, determines the ability of the metal to get transiently polarized. However, the dielectric function is available as measurable quantity for bulk metals. The wavelength at which the plasmon resonance occurs is determined by the real part of the dielectric function of the metal as demonstrated in Eq. 4.

Alkali metals and noble metals are considered free-electron metals, since their optical properties are principally attributed to the conduction electrons. The Drude-Lorentz-Sommerfeld model provides a simple approach to study plasmon resonance, assuming that the conduction electrons can move freely on the surface of the metal independently from the positive background of immobile ions that only act as scattering centers [27, 28]. While the deeper bands in these metals are totally filled, the conduction band is partially filled and thus their dielectric function is governed by the excited transitions in the conduction band. The dielectric function according to this model is given as [28]

$$\varepsilon_1(\omega) = 1 - \frac{\omega_p^2}{\omega^2 + \gamma_0} \tag{13}$$

where ω is the frequency, ω_p is the plasmon frequency in the bulk metal, and γ_0 is given in Eq. 9. The bulk plasmon frequency depends on the free electron density N in the conduction band, as shown in Eq. 14

$$\omega_p = \sqrt{\frac{Ne^2}{\varepsilon_0 m_e}} \tag{14}$$

where m_e is the effective mass of an electron.

However, the effect of other mechanisms governing the light-metallic nanoparticle interaction (e.g.; interband transitions), excluded in the Drude-Lorentz-Sommerfeld model, must be included for better representation of the electronic behaviour. This can be achieved by inserting ε_∞ (the high frequency-limit dielectric constant) in the dielectric function expression given in Eq. 13 to become

$$\varepsilon_1(\omega) = \varepsilon_\infty - \frac{\omega_p^2}{\omega^2 + \gamma_0} \tag{15}$$

In noble metals $\gamma_0 \ll \omega$, Eq. 15 can hence be simplified as

$$\varepsilon_1(\omega) = \varepsilon_\infty - \frac{\omega_p^2}{\omega^2} \tag{16}$$

This shows that while the frequency ω decreases, the real part of dielectric constant becomes more negative. At the plasmon frequency Eq. 4 is satisfied and Eq. 16 can be cast as follows

$$\frac{\omega_p^2}{\omega_{sp}^{\ 2}} = 2\varepsilon_m + \varepsilon_\infty \tag{17}$$

Eventually, the metal type dependence of the plasmon resonance frequency is expressed in terms of ε_∞ and N as

$$\omega_{sp} = \sqrt{\frac{Ne^2}{m_e}} \sqrt{\frac{1}{\varepsilon_0(\varepsilon_\infty + 2\varepsilon_m)}} \tag{18}$$

2.3.2 Size effect

The extinction process, achieved by the plasmon resonance, is directly affected by the size of metallic nanoparticles. For instance, in case of small nanoparticles (e.g., spheres of radii $R \leq 10nm$) it has been found that the scattering is negligible in favor of the absorption and the extinction cross-section, in quasi-static limit, is given as [29]

$$C_{ext} = C_{abs} = \frac{24\pi^2 R^3 \sqrt{\varepsilon_m^{\ 3}}}{\lambda} \frac{\varepsilon_2}{\varepsilon_2^{\ 2} + (\varepsilon_1 + 2\varepsilon_m)^2} \tag{19}$$

While the density of conduction electrons is kept constant, the total number of the electrons increases with increasing volume of a metallic nanoparticle. Thus, the cross-section increases with R^3.

For larger nanoparticles, the plasmon resonance is excited by different plasmon modes ranging from the lower dipolar order to higher multipolar orders.

2.3.2.1 Size effect on extinction process

In spherical nanoparticles with radii ($R \leq 10nm$), the absorption process is only observed in the extinction spectra through single plasmon bands, centered at the same resonance wavelength as illustrated in Figure 2a. The scattering process dominates the extinction for larger particles ($R \geq 30nm$), while the resonance wavelength red-shifts with increasing size as can be seen in Figure 2b [20].

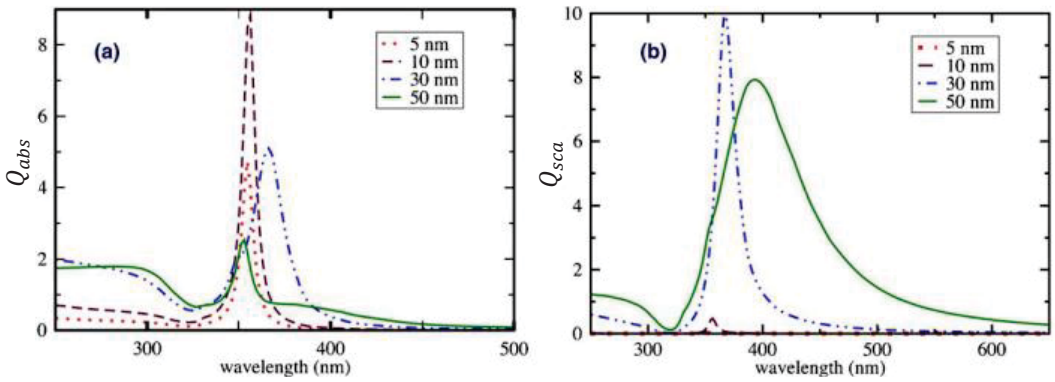

Figure 2| (a) Calculated absorption spectra of different silver spheres with different radii listed in the legend and (b) scattering spectra of the same spheres. Reproduced from ref. [20].

2.3.2.2 The phase retardation effect

While all the conduction electrons in a small metallic nanoparticle experience approximately the same phase of an incident electromagnetic field giving rise to the dipole plasmon resonance mode , the electric field is no longer uniform through a larger metallic nanoparticle and the conduction electrons cannot be therefore displaced simultaneously. The conduction electrons on the facing and opposite sides of

nanoparticles consequently oscillate with different phases, leading to the so-called **phase retardation effect**, and multipolar plasmon resonance modes are eventually excited.

By increasing the particle size, higher plasmon modes are hence excited, the resonance wavelengths of the plasmon modes are red-shifted and the overall line profile of the plasmon resonance gets broadened. These facts have been experimentally observed in the extinction spectra of silver nanostructures by Kumbhar et al. [30].

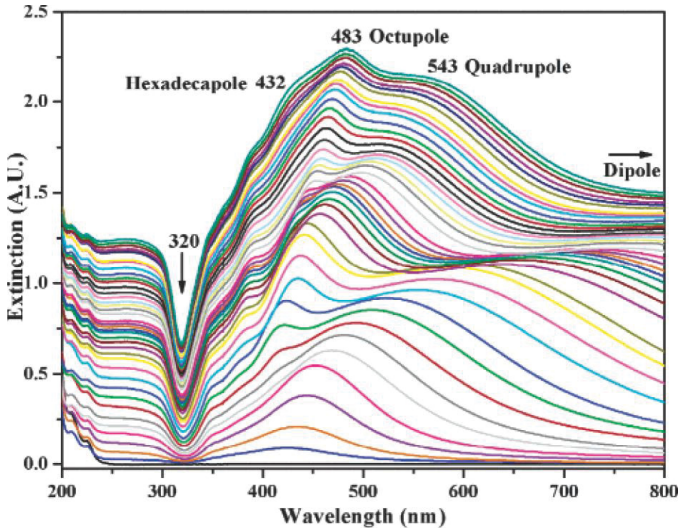

Figure 3| Experimental extinction spectra of nanoparticles consisting of single-crystal silver with different sizes. The particle size ranges from 10nm, represented by the blue spectrum in the bottom, to 215nm illustrated through the green line profile on the top. Reproduced from ref. [30].

Figure 3 shows the extinction spectra of single-crystal silver particles with narrow size and shape distribution. Those particles were synthesized by hydrogen reduction method [30], with a size range of 10nm-215nm. The measured spectra revealed the dipole, quadrupole, octupole and even hexadecapole plasmon resonance modes. In the seeds with size of 10nm, the dipole plasmon resonance was revealed through the spectrum (blue line

in the bottom) with a single peak at 420nm. This peak was observed to be continuously red-shifted as the particle size increased. The dipole resonance wavelength at 490nm of the particle with size ca. 90nm was not the only plasmon band observed in the extinction spectrum; a new peak attributed to the quadrupole mode appeared at 420nm (red eighth line). As the particle size increased the dipole and quadrupole plasmon bands red-shifted to 630nm and 470nm, respectively, and a new band ascribed to the octupole mode arose at 430nm in the particles size of 170nm. By increasing the size, previous peaks kept getting red-shifted until the octupole plasmon band centred at 475nm, and a shoulder attributed to the hexadecapole excitation emerged at 430nm. This shoulder evolved gradually as the particle continued growing. When it reached a maximum size ca. 215nm, the spectrum shows quadrupole, octupole and hexadecapole plasmon modes centered at 543nm, 543nm and 483nm, respectively. The damping of plasmon resonance at around 320nm is attributed to the interband electronic transitions, whereas the shoulder at 350nm is not defined as a plasmon mode and its exact origin is not completely understood [31].

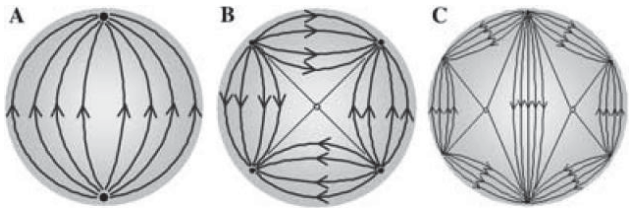

Figure 4| Schematic representations of the electric field lines of the A) dipole, B) quadrupole, and C) octupole plasmon resonance modes. Reproduced from ref. [13].

The electric field lines of the dipole, quadrupole and octupole excitation modes in nanospheres are schematically depicted in Figure 4.

As demonstrated in Figure 5, the absorption is the dominant process and is associated with the dipolar plasmon resonance in smaller nanoparticles, whereas the absorption is roughly associated only with the quadrupole plasmon resonance in the larger particles. The scattering in those latter dominates the extinction process, and is associated with both the dipole and quadrupole modes. The scattering process represents the radiative emission at wavelengths longer than 450nm [32]. At a dimension of 52nm for silver nanoparticles, both the absorption and scattering efficiencies become equal but their resonance wavelengths are shifted relative to each other [33].

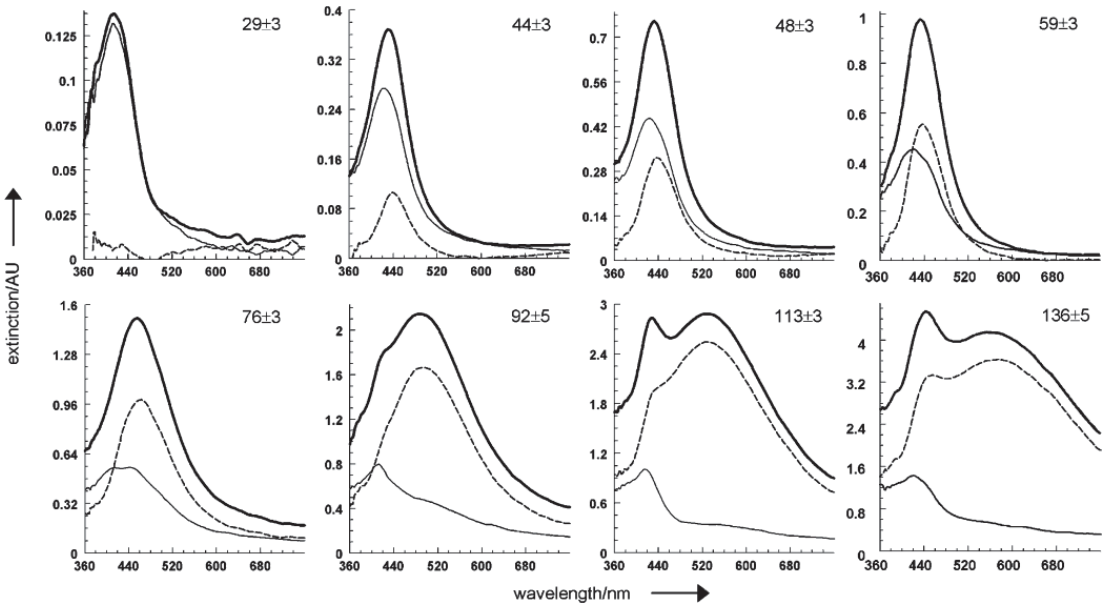

Figure 5| Extinction spectra (thick solid line), absorption spectra (thin solid line) and scattering spectra (dashed line) of silver particle suspensions with various sizes mentioned in each panel. Those spectra are normalized per single particle. Reproduced from ref. [32].

2.3.3 Shape effect

The surface plasmon resonance excites collective electron motion on the surface of metallic nanoparticles. Consequently, the geometry of a nanoparticle restricts the collective motion of the conduction electrons to the surface features, which leads to a direct effect on the plasmon resonance. For instance, the sharper curvature of a nano-spheroid surface weakens the restoring force, due to the Coulomb attraction force between the oscillating electrons and localized positive ions, which is expressed by depolarization factor l .

Involving l in the polarizability relation (Eq. 2) to get the general form that is written as [34]

$$\alpha = \varepsilon_0 V \left(\frac{\varepsilon - \varepsilon_m}{l(\varepsilon - \varepsilon_m) + \varepsilon_m} \right) \tag{20}$$

Obviously, the depolarization factor l depends on the shape, e.g., for a sphere $l = 1/3$ leading to the Clausius-Mossotti relation.

The real part of dielectric constant that satisfies the plasmon resonance condition according to this consideration, expressed in Eq. 4, becomes [34]

$$\varepsilon_1 = -\left(\frac{\varepsilon_m}{l} - \varepsilon_m \right) \tag{21}$$

The depolarization factor introduces the effect of the particle geometry on the plasmon resonance wavelength.

Relative dimensions of a specific shape (e.g., the aspect ratio or major to minor axis ratio of an oblate spheroid) strongly affect the plasmon resonance as illustrated in Figure 6. Although each spheroid is designed to have the same volume, which is equal to that of a sphere of radius 80nm, the extinction spectra of oblate spheroids exhibit various features of the plasmon bands. The dipole plasmon band, centered at a lower energy, progressively red-shifts with increasing aspect ratio, while the quadrupole plasmon band is quenched and the shape becomes more oblate. For the larger aspect ratios, the quadrupole plasmon band is attenuated to a very small peak, located at the high-energy tail of the dominant dipole plasmon band [16].

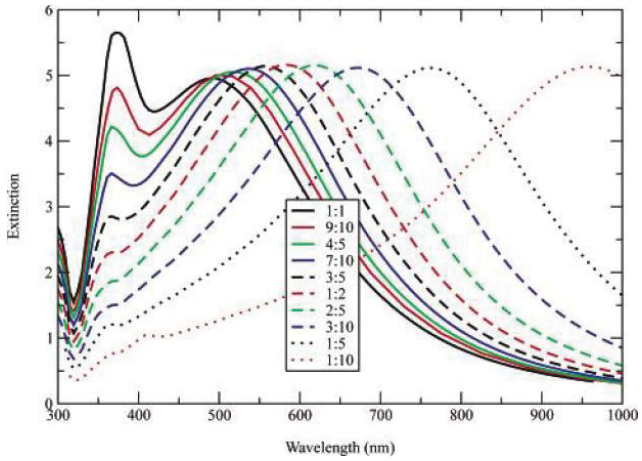

Figure 6| Exact electrodynamic calculation of the extinction spectra of various oblate spheroids having the same volume equals to that of a sphere with radius of 80nm, illuminated by polarized light where the electric field is oriented to be parallel to the major axis, and each spheroid is characterized by the aspect ratio ($AR = major / \min or$) listed in the legend. Reproduced from ref. [16].

The plasmon resonance bands, revealed by the various spectra shown in (Figure 6), declare the importance of particle shape in controlling the plasmon resonance frequency,

while the size, represented by the volume, of those spheroids is kept constant. This actually involves the effect of the volume to surface area ratio on the dielectric function, which describes to the ability of the conduction electrons to oscillate collectively leading to the surface plasmon resonance in metallic nanoparticles [24].

2.3.4 Environment effect

The plasmon resonance frequency of either single or coupled nanoparticles is strongly sensitive to the dielectric function of the surrounding medium. The polarizability of an individual metallic nanoparticle increases in response to an increment in the dielectric constant of the host medium, see Eq. 2 and Eq. 20. The plasmon resonance frequency red-shifts as the negative value of the real part of dielectric function, required to satisfy the condition in Eq. 4 and Eq. 21, increases [35, 36]. The resonance wavelength red-shift can be also derived from Eq. 18 by substituting $\omega_{sp} = kc = \frac{2\pi c}{\lambda_{res}}$ to get

$$\lambda_{res} = 2\pi c \sqrt{\frac{m_e \varepsilon_0 (\varepsilon_\infty + 2\varepsilon_m)}{Ne^2}} \tag{22}$$

An isolated nanoparticle acquires the electric dipole moment μ, when it is placed in electric field E which is related to μ as:

$$\mu = \alpha \varepsilon_m E \tag{23}$$

The charge accumulation, produced in the polarizable host medium and located at the close proximity to the particle, reduces the Coulombic restoring force acting on the polarized electronic cloud. Thus, the larger refractive index ($n_m = \sqrt{\varepsilon_m}$) of the

surrounding medium, the stronger medium polarizability and the weaker restoring force reducing the plasmon frequency.

The wavelength of light penetrating the surrounding medium is reduced when the refractive index of the host medium (n_m) increases, while the embedded nanoparticle receives the so-called effective wavelength $\lambda_{eff} = \lambda / n_m$. Consequently, the particle size with respect to the effective wavelength increases. This is leads to the phase retardation, which excites multipolar plasmon modes, and results also in a significant broadening of the dipole plasmon band in nanoparticles.

In response to an increase in n_m , the plasmon resonance of a system, composed of interacting nanoparticles, exhibits a larger magnitude of plasmon resonance red-shift in relative to that of the isolated component particle, and reflects more sensitivity due to the coupling energy that is originated from near-field interactions between nanoparticles.

In two-dimensional arrays consisting of silver self-assembled spheres of 100nm in diameter, a quadrupole plasmon band, characterized by a sharp peak, is excited due to the phase retardation (Figure 7a) [37]. The resonance wavelength, in this case, is highly sensitive to the refractive index of the environment. This sensitivity has been found to be linearly dependent on the refractive index of the host medium within around 35nm-spectral range [37] as illustrated in Figure 7b. These host media are solvents, composed of various mixtures of polymer solutions allowing gradual increments in the refractive index.

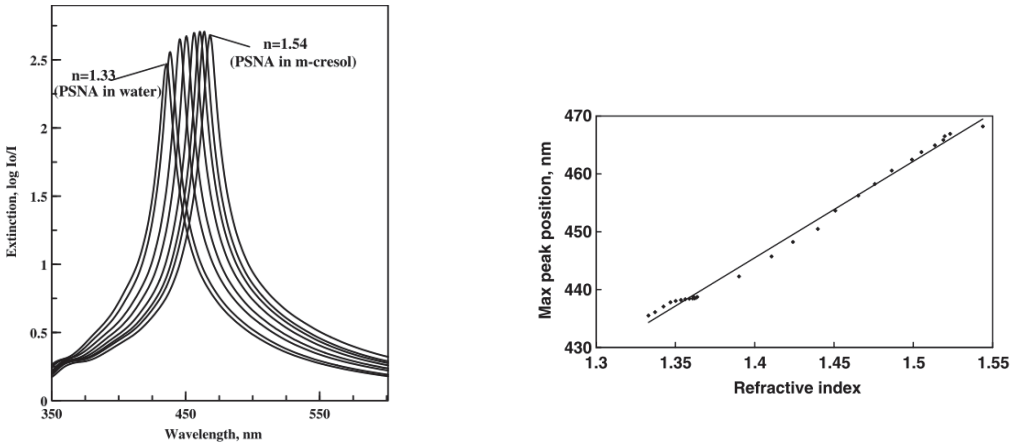

(a) (b)

Figure 7| (a) Extinction spectra of planar silver nanoparticle arrays (PSNA), surrounded by various host media water/ethanol and ethanol/m-cresol mixtures. The resonance wavelength red-shifts with gradual increments in the refractive index of the host medium, (b) successive plasmon wavelength red-shifts as a function of the refractive index of the surrounding medium. Reproduced from ref. [37].

This system of self-assembled silver nanospheres planar array relying on quadrupole excitation could be used in measurement applications, since it provides highly sensitive measurements of the refractive index of the surrounding environment. Each 0.006 RIU (unit change of the refractive index) corresponds to nm wavelength shift, and the sharpness of the plasmon peak provides an accurate measurement of 0.1nm of the spectral shift [37]. Thus, 0.0006 RIU is possible to be detected by a bench-type spectrophotometer.

2.4 Plasmon coupling

Assemblies of nanoparticles constitute coupled systems, the plasmon resonance frequency of the assembly is highly affected by the interactions between nano-sized particles, and governed by plasmon coupling energy, which depends, besides the

aforementioned factors, on i) the polarization direction of the incident light relative to the surface of a two-dimensional assembly or the interparticle axis of a linear chain of nanoparticles, ii) nanoparticle arrangement determines the number of the closest neighbouring particle and iii) the interparticle separation. The plasmon resonance of a system consisting of interacting particles is hence called plasmon coupling resonance.

It has been found by numerous theoretical calculations and experimental measurements that the plasmon resonance wavelength, observed in the spectrum of interacting nanoparticles, is either red-shifted or blue-shifted as the inter-particle separation decreases depending on the direction of the incident electric field (incident polarization). For instance, the plasmon coupling of a dimer exhibits a large red-shift as the nanoparticles approach each other for incident polarization parallel to the dimer axis, due to the applied and induced electric fields that are constructively added to each other as illustrated in Figure 8a. For incident polarization perpendicular to the axis, a destructive interaction between the applied and induced electric fields is predicted as shown in Figure 8b, leading to a small blue spectral shift [6], where the plasmon coupling resonance is excited by the dipole mode. This fact is also applied to one-dimensional linear chain [3].

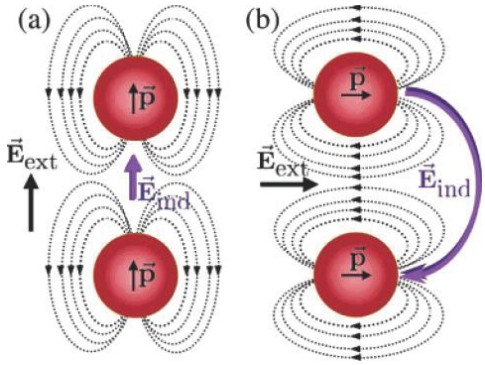

Figure 8| Diagrams represent electromagnetic interaction between two nanoparticles for an applied electric field (a) parallel and (b) perpendicular to the axis of the two particles or a linear chain. Reproduced from ref. [3].

In a two dimensional array of small silver nanoparticles, the applied electric field induces highly enhanced local electric field. The local field extends from the particle surface to a distance comparable to the diameter of the nano-sized particle. When small nanoparticles are placed in close proximity to each other, the local fields of individual particles overlap, producing the plasmon coupling resonance. Depending on the incident polarization direction, two dipole plasmon resonance distinct bands are observed. Figure 9 shows the absorption spectra of 91 silver nanospheres of radii R=2.5nm hexagonally close-packed in a planar array, the longitudinal and transverse plasmon bands are excited for incident polarization parallel and perpendicular to the array surface, respectively. By decreasing the interparticle separation, resonance wavelengths of the longitudinal plasmon band is red-shifted while the transverse band is blue-shifted [38].

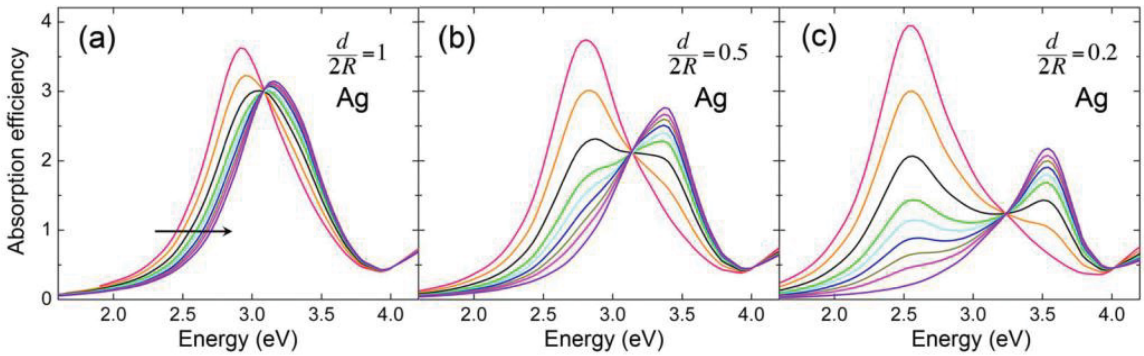

Figure 9| plasmon coupling bands of 91 silver nanospheres of radii R=2.5nm hexagonally close-packed in a planar array, red line represents longitudinal plasmon spectrum (under parallel polarization), and violet line indicates the transverse plasmon spectrum (under perpendicular polarization), the other lines in between occurs under oblique polarizations. The interparticle separation: (a) d=5nm, (b) d=2.5nm, and (c) d=1nm. Reproduced from ref. [38].

CHAPTER 3

The discrete dipole approximation

Introduction

The basic concept of the DDA was originally presented by DeVoe [39] in 1964. This approximation, as a discretization method to solve Maxwell's equations in the case of matter-light interaction, is assumed to replace the continuum particle by a finite array of points N (polarizable entities). Each point possesses an oscillating dipole moment in response to the incident electric fields and to the contribution of the other polarizable points composing all together the entire array. The problem is then reduced to a system of linear equations. In 1973 Purcell and Pennypacker [40] developed the DDA to calculate the scattering and absorption cross-sections of the interstellar dust grains. The self-consistent solutions of the linear equations were restricted to a small number of the dipoles $N \leq 256$, and difficulties with convergence of the iterative algorithm were reported. In 1978, Yung [41] exploited another iterative algorithm to solve these linear equations with large N up to 15600, but it failed to converge when large dielectric functions were considered. Then by successive improvements, particularly the ones which have been achieved by B. T. Draine, P. J. Flatau and J. Goodman [42], this approximation has been refined to solve the scattering problems by either individual or multiple particles of any geometry and size with high accuracy, Moreover, they allow to model systems composed of various materials.

3.1 DDSCAT

DDSCAT is a FORTRAN implementation of the DDA, developed by B. T. Draine, P. J. Flatau, and the software package of the DDSCAT is freely available [43], and it requires that the polarizable points be located on a cubic lattice. The most recent version DDSCAT7.1 released in 2010 has been used.

3.2 DDSCAT input files:

3.2.1 Target geometry

The executable file "**ddscat.exe**" must be provided with the spatial Cartesian coordinates of the N dipoles. These coordinates can be either set by the user in a separate file "**shape.dat**", or it can be automatically generated by the executable file according to some parameters that must be defined by the user. In both cases, the dipoles must be located in a cubic lattice, and the number of dipoles is optionally controlled to produce a desired interdipole separation (or lattice spacing constant) d .

3.2.2 Target size

The target size is represented by N the number of the dipoles composing the discretized continuum particle, where each dipole occupies a volume d^3. The simulation target size is only limited by the supporting hardware. The ideal environment for simulation is a multi-core system with a compliant OpenMP compiler that supports parallel programming in a multi-platform infrastructure with shared-memory, where the computational processing is highly accelerated.

For instance, a single particle of 46nm in diameter, represented by 1,697,504 dipoles, has been simulated using a machine of 8 CPUs and 16 GB of RAM running Intel® ifort compiler.

3.2.3 Target material

The target can be composed of different materials. The material data is inputted to the ddscat.exe by either the refractive index or the dielectric function. In order to avoid the lack of numerical resolution, the dielectric constant at the incident wavelength considered should be provided for each component material. Those constants are tabled in external files for each material, which are referred to during the execution at each wavelength.

3.2.4 Wavelength of incident light

The target is simulated and the linear equations are iteratively solved for every wavelength of the given spectral region.

3.2.5 Target orientation

The target orientation is defined with respect to i) the wave vector defining the propagating direction of the incident light and ii) the electric field direction.

The incident angle can be changed indirectly through a set of three elective angles, which determine the rotation of the target frame in three orthogonal planes with reference to the lab frame, where the lab frame axes are defined by the wave vector and the electric field direction.

3.3 DDSCAT outputs:

3.3.1 Absorption efficiency factor

$$Q_{abs} = \frac{C_{abs}}{\pi a_{eff}^2}$$

where C_{abs} is the absorption cross-section, and πa_{eff}^2 represents the cross-section of a sphere of equal volume, where a_{eff} is the "effective radius".

3.3.2 Extinction efficiency factor

$$Q_{ext} = \frac{C_{ext}}{\pi a_{eff}^2}$$

where C_{ext} is the extinction cross-section.

3.3.3 Scattering efficiency factor

$$Q_{sca} = \frac{C_{sca}}{\pi a_{eff}^2} = Q_{ext} - Q_{abs}$$

where C_{sca} is the scattering cross-section.

3.4 Target geometry

The interdipole separation d is required to be small enough to achieve a good shape definition of the target, by satisfactorily approximating the exact particle shape via the boundaries of the periodic cubic lattice, as shown in Figure 10.

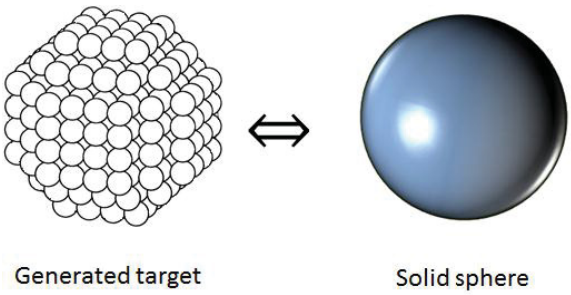

Figure 10| Schematic representation of a solid nanosphere in terms of the dipole sites that are located in a cubic lattice.

3.5 Target size

The DDSCAT characterizes the volume by the effective radius a_{eff} . The equivalent sphere contains the same number of the dipoles composing the target regardless of its shape. Each dipole is represented by an occupied site in the cubic lattice, with a cubic subvolume d^3 of material centered on that site.

The solid sphere (Eq. 24) is equivalent to that generated in term of dipoles sites (Eq. 25) shown in Figure 11.

$$V = \frac{4}{3}\pi R^3 \tag{24}$$

$$V = Nd^3 \tag{25}$$

Thus, the effective radius can be written in terms of N and d as

$$a_{eff} \equiv R = \sqrt[3]{\frac{3N}{4\pi}}\, d \tag{26}$$

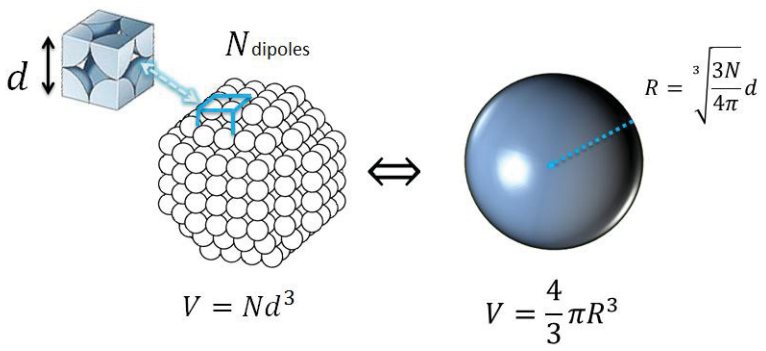

Figure 11| Diagram depicting the DDSCAT target of a single sphere of radius R (to the right). The target consists of N dipoles located in a cubic lattice whose lattice spacing is d .

In the case of a system involving interacting particles, the equivalent sphere contains the actual mass of all the particles. For instance, a schematic representation of a target consisting of two different spherical nanoparticles is depicted in Figure 12,

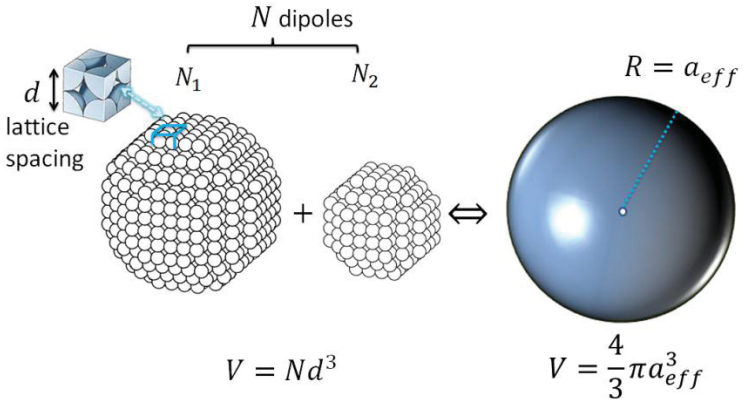

Figure 12| Schematic representation of the DDSCAT target replicating two different spheres by means of periodic dipoles located in a cubic lattice, the equivalent sphere target is the sum of their volumes and contains the total number of dipoles $N = N_1 + N_2$.

The volume of the target is given as $V = (N_1 + N_2)\, d^3$. The volume of the equivalent sphere containing the actual mass is $V = \frac{4}{3}\pi a_{eff}{}^3$ or equivalently $V = \frac{4}{3}\pi(R_1^3 + R_2^3)$. Thus, the effective radius can be written as

$$a_{eff} = \sqrt[3]{R_1^3 + R_2^3} \tag{27}$$

and the interdipole separation (the lattice spacing) is given as

$$d = \sqrt[3]{\frac{4\pi}{3(N_1 + N_2)}}\; a_{eff} \tag{28}$$

3.6 Spurious surface effect

Each dipole occupies a site in the periodic cubic lattice, possesses a cubic subvolume d^3 and represents the polarizability of such a subvolume of the particle [44]. As a matter of fact, the dipoles locating near the particle boundaries "the surface dipoles" should be weaker than the inner dipoles, or equivalently occupy a smaller subvolume for more precise calculation. However, DDSCAT7.1 does not take this perspective into consideration to avoid the substantial cost of computational resources, which leads to an overestimation in the extinction cross-section calculated; this effect is known as the **spurious surface effect**. Thus the ratio of surface-to-inner dipoles represents a crucial parameter. In order to prevent the spurious surface effect, it is preferable to minimize this ratio by decreasing the interdipole separation d, which concurrently reduces the granularity of the surface. This is usually achieved by increasing N to a reasonable value that is computationally convenient for a proper convergence.

The number of the surface dipoles varies depending on the geometrical shape of the target, e.g., the number of the surface dipoles N_{surf} in a sphere, composed of N dipoles, was calculated by Sosa and coworkers [45] as $N_{surf} = N - (\sqrt[3]{N} - 1)^3$. The number of surface dipoles and the surface-to-total dipoles ratio are calculated in the table below for various N

Total dipoles N	Surface dipoles N_{surf}	(N_{surf} / N) (%)
10^2	51.7	51.7
10^3	271.0	27.1
10^4	1328.8	13.2
10^5	6325.0	6.32
10^6	29701.0	2.97

Table 1| Dependency of the surface dipole portion relative to the entire dipoles that are used to represent a spherical particle. Reproduced from ref. [45].

Taking a large number of dipoles N to represent a target, the computational time in turns increases proportionally to $0.003N^3$ CPU s, which imposes an upper limit to N. However, the number of dipoles representing a target is subject to optimization.

3.7 Computational considerations

3.7.1 Iterative method

The target is discretized to N dipoles by the DDA, and the scattering problem is therefore reduced to a system of complex linear equations which can be given as [46]:

$$\vec{E} = \mathbf{A}\vec{P} \tag{29}$$

$\vec{E}$: $3N$-dimensional complex vector of the incident electric field.

$\vec{P}$: $3N$-dimensional complex vector of the unknown dipole polarizations.

$\mathbf{A}$: $3N \times 3$N complex matrix.

The iterative methods are more efficient for solving this system of equations than the direct methods for as $3N$ is usually a large number. By initiating an initial guess $\vec{p}$, and afterwards the estimation of $\vec{P}$ is iteratively improved until the previous equation is solved to a desired error criterion.

In the present work, the BiConjugate Gradient with Stabilization algorithm (PBCGS2) [46,47] was used for iterative solution.

3.7.2 Dipole polarizability and scattering problem

The polarizable points (dipoles), located in a periodic cubic lattice at the positions $i = 1,2,3,...,N$, are irradiated by an incident plane wave; ddscat.exe assigns a polarizability α_i to each point, and eventually a dipole moment "polarization" $\vec{P}_i$

$$\vec{P}_i = \alpha_i \cdot \vec{E}_{i\,loc} \tag{30}$$

where α_i is polarizability of the point at $\vec{r_i}$, and $\vec{E}_{i\,loc}$ is the local electric field acting on the dipole located at *i-th* point. The polarizability prescription used in Eq. 30 is given by the Lattice Dispersion Relation (LDR) [48]:

$$\alpha_i \equiv \alpha_{LDR} \approx \frac{\alpha^{CM}}{1+\alpha^{CM}\left[\left(b_1+\varepsilon b_2+\varepsilon S b_3\right)\left(\frac{k^2}{d}\right)-\frac{2}{3}ik^3\right]} \tag{31}$$

where d is the lattice spacing, ε is the dielectric function of the subvolume centered at location $\vec{r}_i$ and α^{CM} is the polarizability given by a Clausius-Mossotti relation [49]:

$$\varepsilon = \frac{4\pi n\alpha^{CM}}{1-\left(\frac{4\pi}{3}\right)n\alpha^{CM}}+1 \tag{32}$$

where n is the number of the polarizable points in unit volume, b_1, b_2, b_3 are constants and $S \equiv \sum_{j=1}^{3}\left(a_j \hat{e}_j\right)^2$ where $a_j, \hat{e}_j$ are unit vectors providing the incident direction and the polarization state.

On the other hand, the local electric field representing the total electric field at location $\vec{r}_i$ is given as

$$\vec{E}_{i\,loc} = \vec{E}_{i\,inc} + \vec{E}_{i\,ind} \tag{33}$$

where $\vec{E}_{i\,inc}$ is the incident electric field, and $\vec{E}_{i\,ind}$ is the induced electric field acting on the *i-th* dipole due to the contribution of all other $N-1$ dipoles composing the target with the *i-th* dipole , including retardation effect.

Considering an incident monochromatic plane wave

$$\vec{E}_{i\,inc} = \vec{E}_0\, e^{(i\vec{k}\cdot\vec{r}-\omega t)} \tag{34}$$

and the induced electric field is given by

$$\vec{E}_{i\,ind} = -\sum_{j\neq i}^{N} \mathbf{A}_{ij} \cdot \vec{P}_j \tag{35}$$

where $-\mathbf{A}_{ij} \cdot \vec{P}_j$ is the electric field at the dipole $\vec{P}_j$ located at $\vec{r}_j$, the element $\mathbf{A}_{ij}$ is a 3x3 matrix representing the electromagnetic interaction among the dipoles. This matrix is formed as [44]

$$\mathbf{A}_{ij} = \frac{\mathrm{e}^{ikr_{ij}}}{r_{ij}} \left[k^2 (\hat{r}_{ij}\hat{r}_{ij} - \mathbf{1}_3) + \frac{ikr_{ij} - 1}{r_{ij}^2} (3\hat{r}_{ij}\hat{r}_{ij} - \mathbf{1}_3) \right] \tag{36}$$

where $i \neq j$, $\mathbf{1}_3$ is the 3×3 identity matrix, $r_{ij} = \left|\vec{r}_i - \vec{r}_j\right|$, $\hat{r}_{ij} = \dfrac{(\vec{r}_i - \vec{r}_j)}{r_{ij}}$ and k is the wavenumber.

Substituting the induced electric field from Eq. 35 into Eq. 33, then by substituting the local field outcome into the Eq. 30, we get the dipole moment of the point at the position i, represented by a system of $3N$ linear equations

$$\vec{P}i = \alpha_i \cdot \left(\vec{E}_{i\,inc} - \sum_{1=j\neq i}^{N} \mathbf{A}_{ij} \cdot \vec{P}_j \right) \tag{37}$$

or it can be cast as

$$\vec{E}i_{\,inc} = \sum_{j=1}^{N} \mathbf{A}_{ij} \cdot \vec{P}_j \tag{38}$$

But when $i = j$ the element $\mathbf{A}_{ii} \equiv a_i^{-1} = a_{LDR}^{-1}$ (see Eq. 31)

Solving the latter equation (Eq. 38), which represents Eq. 29, for the all the dipoles constituting the target, once the unknown polarizations are $\vec{P}_i$ found the extinction and scattering cross-sections are calculated by the following equations [44]:

$$C_{ext} = \frac{4\pi k}{|\mathbf{E}_0|^2} \sum_{i=1}^{N} \mathrm{Im}\left(\mathbf{E}^*_{i_{inc}} \cdot \mathbf{p}_i\right) \tag{39}$$

$$C_{abs} = \frac{4\pi k}{|\mathbf{E}_0|^2} \sum_{i=1}^{N} \left[\mathrm{Im}\left(\mathbf{p}_i \cdot (\alpha_i^{-1})^* \mathbf{p}_i^*\right) - \frac{2}{3} k^3 |\mathbf{p}_i|^2 \right] \tag{40}$$

where $\mathbf{E}_{i_{inc}} \equiv \vec{E}\, i_{inc}$ and $\mathbf{p}_i \equiv \vec{P}_i$

The scattering cross-section could also be evaluated once $\mathbf{p}_i$ are known as

$$C_{sca} = C_{ext} - C_{abs} \tag{41}$$

3.7.3 FFT method

In order to exploit the Fast Fourier Transform (FFT) method, the N point dipoles are required to be located in a periodic lattice, and each dipole site is assigned to occupy the same polarizable subvolume d^3, regardless of its location whether is on the surface or in the core of the target. FFT methods can greatly accelerate the computational processing, which is reduced to $O(N \ln N)$ operations instead of $O(N^2)$ operations that are required for solving the scattering problem formed in Eq. 29 [50].

3.7.4 Compiler

The FFTMKL Algorithm, obtained from Intel®MKL library, was used. This enabled us to use a machine of 8 CPUs running Intel® ifort compiler, provided in Intel® composer 2011 package.

In addition, gfortran compiler was used to simulate small targets by using a single CPU, as the DDSCAT7.1 package seems not to support the OpenMP option with this compiler.

3.7.5 Memory & CPU requirements

The total memory required by the DDSCAT for simulating a target consisting of N dipoles is approximately $0.58N_V/1000$ Mbytes [44], where $N_V = N_x N_y N_z$ is the volume of the rectangular "or cubic" containing all of the target's dipoles. The total CPU requirement for a single iteration is about $3N_V/1000$ CPU s [44].

This means that the memory and CPU requirements are linearly proportional to the rectangular volume, containing the overall dipoles. It is directly deduced that those requirements strongly depend on the number of dipoles representing that particle, which is well-understood for a system of a single particle. But for a target consisting of assembly of separate particles, these requirements depend on the interparticle separation D in addition to particles size, which heavily increases the computational cost.

CHAPTER 4

The size-corrected dielectric function and the effect of the host medium on the optical properties of isolated spherical silver nanoparticles

Introduction

The selection of the appropriate dielectric function along with a sufficient number of dipoles has a key effect in determining the level of accuracy that can be reached, in order to precisely predict the optical response of nanoparticles.

4.1 Size-corrected dielectric function

The dielectric functions ε_{Bulk} of bulk metals of interest have been experimentally measured. The dielectric function ε_{Bulk} can be expressed as

$$\varepsilon_{Bulk} = \varepsilon_{Inter} + \varepsilon_{Intra} \tag{42}$$

where ε_{Inter} describes the interband electronic transitions, and ε_{Intra} stands for the intraband transitions (see 2.2).

4.1.1 Drude free electron model

The electronic motion, described by ε_{Intra}, represents the electronic transitions at Fermi level in metals, where the free electron are excited by the localized surface plasmon resonance, and can be modeled by the Drude model as (see 2.2)

$$\varepsilon_{Intra} = \varepsilon_{Drude}^{Free}(\omega) = 1 - \frac{{\omega_p}^2}{\omega^2 + i\,\omega\gamma_0} \tag{43}$$

4.1.2 Electron-surface scattering

The energy absorbed by the free electrons "plasmon resonance", then it is fractionally dissipated by electron-surface scattering (see 2.2). Thus, it is necessary to impose an additional damping term to ε_{Bulk}, which can be done by inserting an extra damping term $A\frac{v_F}{R}$ to the Drude model as

$$\varepsilon_{Drude}^{Free+Surface}(\omega, R) = 1 - \frac{{\omega_p}^2}{\omega^2 + i\,\omega\gamma} \tag{44}$$

where γ is the damping constant:

$$\gamma = \gamma_0 + A\frac{v_F}{R} \tag{45}$$

The second term, Av_F / R, is responsible for additional dephasing of electrons. For spherical particles $A = 3/4$. The total damping constant γ participates in determining the

width of the plasmon resonance band [51]. For other geometries, other than spheres, the term $A\nu_F / R$ can be written in terms of L_{eff} , given in Eq. 10, as [52]

$$L_{eff} = \frac{4V}{S}$$

where S and V are the surface area and volume of the particle, respectively.

4.1.3 Corrected dielectric function

The final dielectric function, includes the contributions of transitions of bound electrons and free electrons, besides electron-surface scattering is given by $\varepsilon = \varepsilon_{\text{inter}} + \varepsilon_{Drude}^{Free+Surface}$

Substituting $\varepsilon_{\text{inter}}$ from Eq. 42

$$\varepsilon = \varepsilon_{bulk} - \varepsilon_{Intra} + \varepsilon_{Drude}^{Free+Surface} = \varepsilon_{bulk} - \varepsilon_{Drude}^{Free} + \varepsilon_{Drude}^{Free+Surface} \tag{46}$$

Using Eq. 43, Eq. 44 and Eq. 45

$$\varepsilon(R,\omega) = \varepsilon_{bulk}(\omega) + \frac{{\omega_p}^2}{\omega^2 + i\,\omega\gamma_0} - \frac{{\omega_p}^2}{\omega^2 + i\,\omega\left(\gamma_0 + A\,\frac{\upsilon_F}{R}\right)} \tag{47}$$

It is worth mentioning that the interband and intraband transitions exhibit two absorption bands in the spectral region at the UV region and from IR to visible light region, respectively [53].

4.2 Corrected dielectric function of small spherical silver particles

The dielectric function dependency on the size has been calculated by Eq. 47 for all spherical particles, simulated in this work, while the dielectric functions measured experimentally for bulk metals were taken from Johnson and Christy [54].

4.2.1 Imaginary part ε_2

As the radius of a spherical silver nanoparticle decreases, the imaginary part increases with wavelength in the spectral range extending from 330nm to 945nm illustrated in Figure 13. The increment rate with the wavelength is higher for the smaller particles. The difference in the imaginary part at 330nm between particles with radii $R = 2.5nm, 40nm$ is trivial (around 0.5) relative to a significant difference (9.5) observed at the longer wavelengths in the spectral range considered.

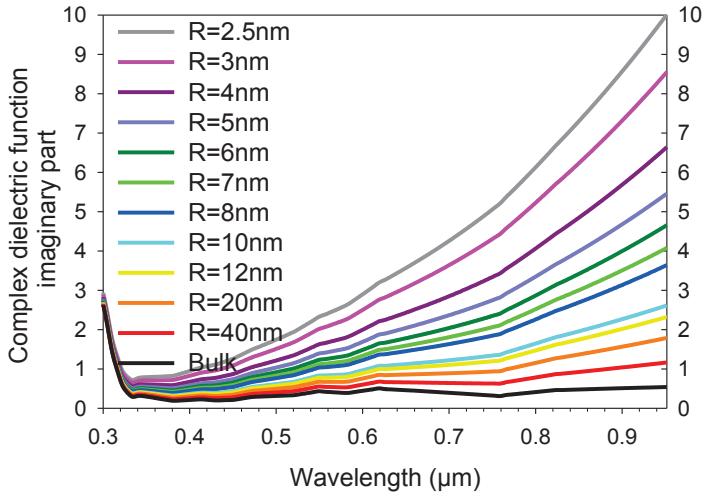

Figure 13| Imaginary part ε_2 of the corrected dielectric constant ε of silver nanospheres of various radii (listed in the legend) as a function of the wavelength.

Thus, the increment in the imaginary part is more pronounced for smaller spheres $R \leq 10nm$ at longer wavelengths. This behaviour results in broadening of the dipole absorption plasmon resonance band observed in small (ultrafine) nanoparticles.

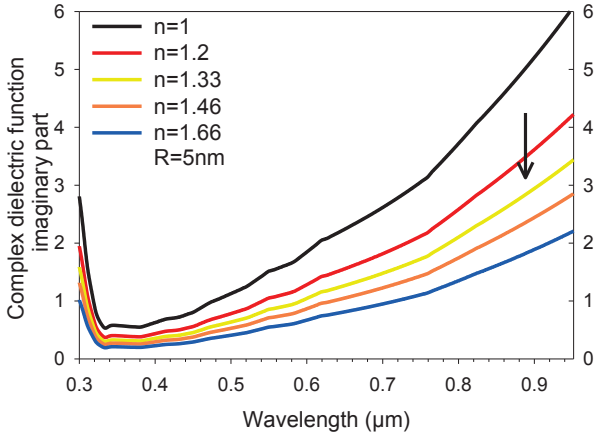

Figure 14| Imaginary part ε_2 of the corrected dielectric function of silver nanosphere of radius 5nm, immersed in various host media (refractive indices n_m listed in the legend), as a function of the wavelength.

When the refractive index of the surrounding medium increases, the imaginary part of the dielectric function decreases as illustrated in Figure 14. The decrements were more pronounced at longer wavelengths, where a silver sphere of radius 5nm has been considered.

4.2.2 Real part ε_1

In decreasing the sphere diameter, the real part of the complex dielectric function barely changes at longer wavelengths, as illustrated in Figure 15a, while it is not affected by the particle size in the spectral region of smaller wavelengths. Thus, the effect of the

correction on the real part ε_1 is almost null, especially at shorter wavelengths, contrary to the case of ε_2.

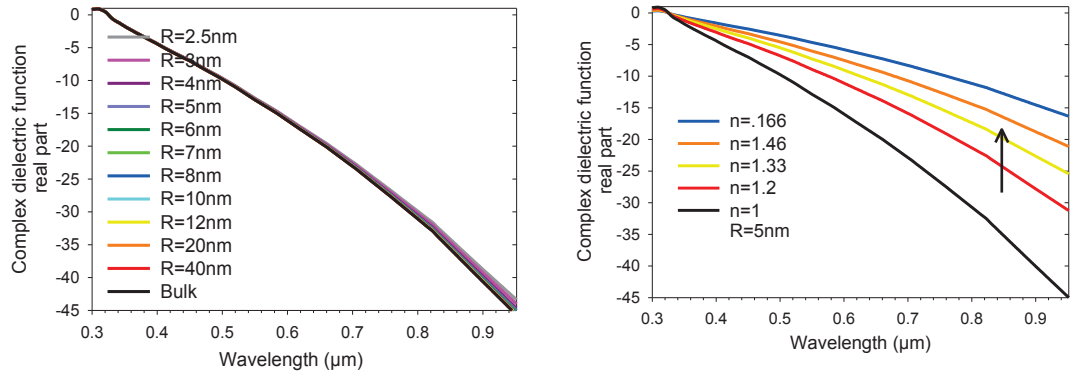

(a) (b)

Figure 15| Real part ε_1 of the size-corrected dielectric function of (a) silver nanospheres of various radii (listed in the legend) as a function of the wavelength. The corrected real part exhibits very slight deviations from the bulk (b) a silver nanosphere of radius 5nm, immersed in various host media (n_m listed in the legend) as a function of the wavelength.

When the refractive index of the surrounding medium increases, the real part of the dielectric function of silver sphere 5nm decreases to a smaller negative value, as illustrated in Figure 15b. While this decrement is more pronounced at longer wavelengths, it is not observed at shorter wavelengths in the considered spectral region. This leads to a red-shift in the dipole plasmon band and. The magnitude of this red-shift is expected to be more pronounced in the case of larger particles that have longer dipole resonance wavelengths (see Figure 15b).

Conclusion

In the spherical silver nanoparticle, the imaginary part ε_2 is a strong wavelength-dependent with smaller sizes $R < 8nm$ (Figure 13), where the dissipating energy is more pronounced (see 2.2). The energy losses can be hence described by the imaginary part ε_2, while the real part ε_1 determines the plasmon resonance wavelength (Eq. 4).

As can be seen in Figure 16, over the entire considered spectral region the imaginary part increases from 0.5 to 3.5, which seems to be a wavelength-independent relative to a rapid increase in the absolute value of the real part with the wavelength.

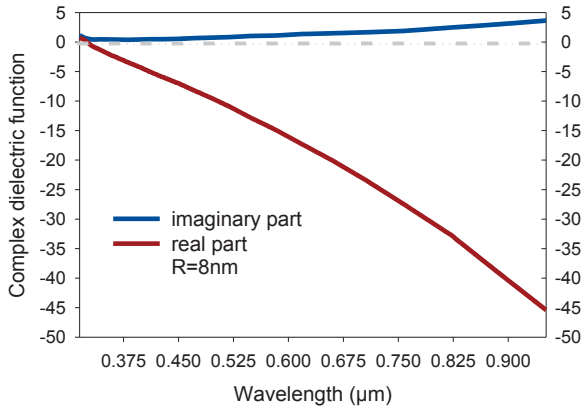

Figure 16| The corrected complex dielectric function of a silver sphere of 8nm, embedded in a host medium of refractive index $n_m = 1$, as a function of wavelength.

An increase in the refractive index of the dielectric host medium, for a given particle $R < 8nm$, reduces ε_1 and ε_2, which consequently red-shifts the plasmon resonance wavelength and decreases the energy dissipation in the nanoparticle.

4.3 The environment effect on the dipole plasmon resonance in single spherical silver nanoparticles

Silver nanoparticles exhibit a very strong interaction with light due to the localized surface plasmon resonance. Small silver nanoparticles are therefore highly efficient in absorbing the light energy in the visible region, as the absorption cross-section C_{abs} of a silver nanoparticle collecting the light energy is larger than the geometric cross-section C_{geo}. Several numerical methods have been developed to investigate the optical response of metal nanoparticles. The absorption and scattering efficiencies for a homogeneous silver sphere have already been calculated by using MiePlot v4.2 [55], the implementation of the Mie theory, and based on the BHMI code.

As an appropriate entrance to the following topics, single silver nanospheres are simulated, the optical response is revealed by means of the absorption efficiency spectra ($Q_{abs} = C_{abs} / C_{geo}$). The resonance wavelengths of the single silver nanosphere will be needed as a reference to calculate the plasmon shift of coupled particles, studied in next chapters. The variations of absorption spectra with the sphere size of radius R are investigated in various surrounding media of refractive indices $n = 1,\ 1.33,\ 1.46,\ 1.66$.

The absorption spectra of isolated silver spheres of various sizes, surrounded by the medium of $n = 1$, are plotted in Figure 17a showing the dependency of the dipole wavelength resonance on the particle size. The maximum absorption efficiency occurs for the optimum radius (optimum size) $R_{opt} = 20nm$ (Figure 17a).

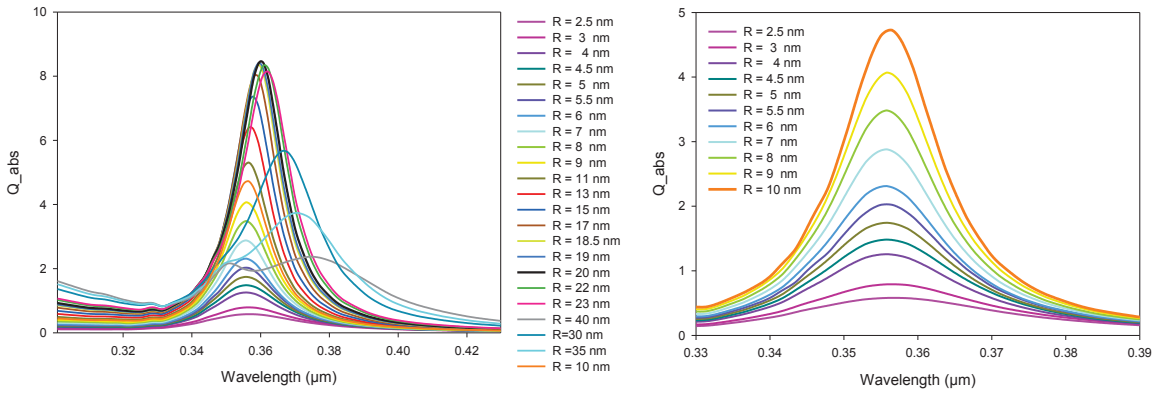

(a) (b)

Figure 17| Absorption spectra of individual silver spheres of different radii in air $n=1$ illustrating (a) the dependency of the spectral peak position on the size(b) the dipole resonance wavelength λ_0 for various spheres radii $R<R_0$ (listed in the legend).

For small particles when $R \leq 10nm$, the dipole resonance wavelength $\lambda_0 = 355.8nm$ is independent from the particle size as illustrated in Figure 17b, the critical radius is therefore defined as $R_0 = 10nm$. Exceeding the critical radius the resonance wavelength, designated by λ_{res} when $R > R_0$, red-shifts with a magnitude $\Delta\lambda = \lambda_{res} - \lambda_0$ as can be seen in Figure 18a.

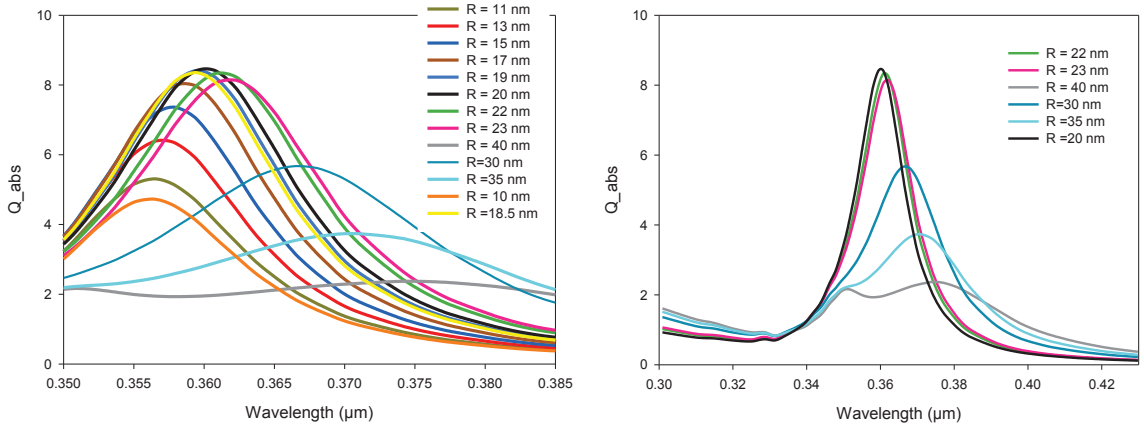

(a) (b)

Figure 18| Absorption spectra illustrate that the resonance wavelength red-shifts with increasing radius (listed in the legend) while the plasmon bandwidth is broadened.

As shown in Figure 18a the dipole plasmon resonance is the only plasmon mode that can be found when $R \leq 25nm$ as the conduction electrons oscillate in the same phase. For particles larger than the optimum size, the absorption efficiency decreases and the absorption band gets broadened with the size.

Changing the surrounding medium to poly (dimethylsiloxane) (PDMS) of $n = 1.46$, the dipole plasmon band red-shifts to $\lambda_0 = 399nm$ as expected. It is found that the optimum and critical sizes get smaller $R_{opt} = 13nm$ and $R_0 = 8nm$, respectively as can be induced from Figure 19a, b. The quadrupole mode is pronounced with a distinguished shape at a smaller size $R = 17.5nm$.

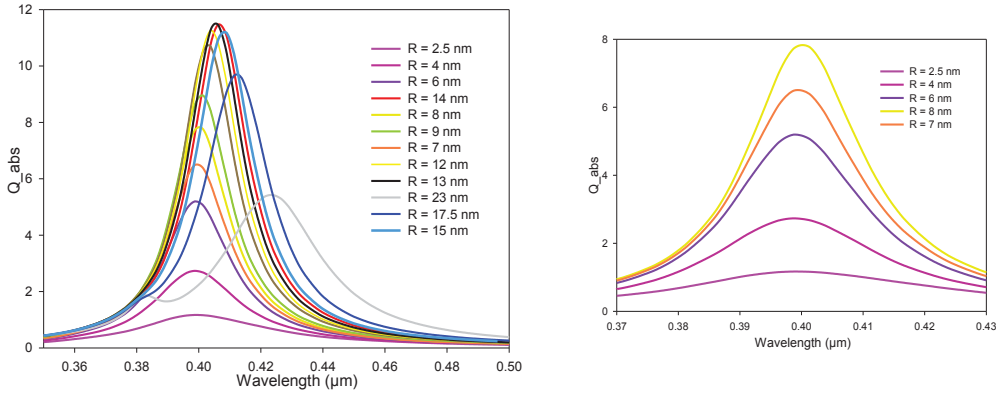

(a) (b)

Figure 19| Absorption spectra of individual silver spheres of different radii in air $n=1.46$ illustrating (a) the dependency of the spectral peak position on the size(b) the dipole resonance wavelength λ_0 for various spheres radii $R<R_0$ (listed in the legend).

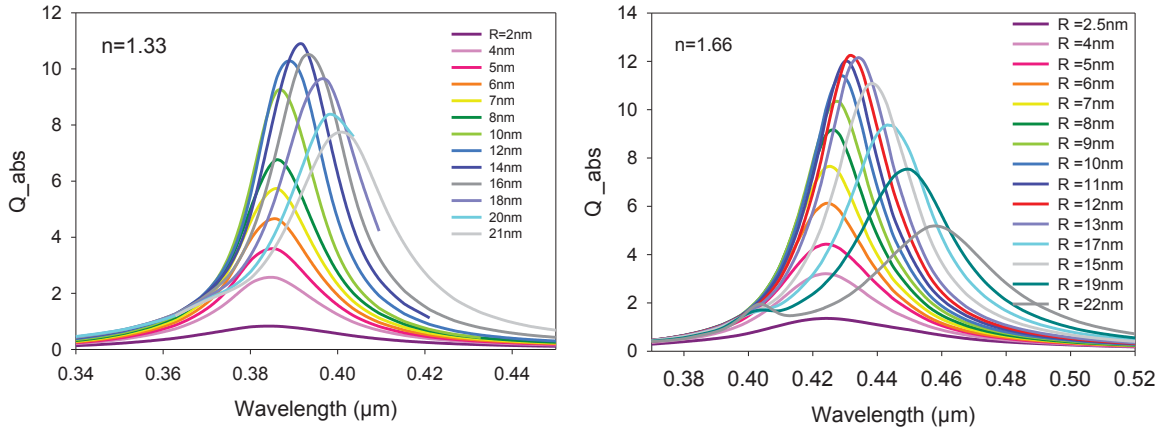

(a) (b)

Figure 20| Absorption spectra of individual silver spheres of different radii embedded in a host medium of refractive index (a) $n=1.33$ and (b) $n=1.66$, illustrating the dependency of the spectral peak position on the sphere radius (listed in the legend).

Simulating single silver particles in two other host media, a similar tendency is observed as illustrated in Figure 20. A maximum efficiency is reached at $R_{opt}=14nm, 12nm$ and

the critical radii are $R_0 = 9nm, 6nm$ corresponding to the resonance wavelengths $\lambda_0 = 386.1nm, 424nm$ in media of $n = 1.33, 1.66$, respectively.

4.3.1 Absorption cross-section

When the refractive index of the surrounding medium is fixed at $n = 1$, The linear proportion between the absorption efficiency and the particle size is restricted to small radii less than $18nm$, and the scattering process is negligible as demonstrated in Figure 21, The absorption efficiency reaches a maximum when $R = 20nm$. Exceeding this size, the absorption efficiency then decreases in favour of the scattering efficiency until they coincide at the same value when $R = 29nm$. As the size increases, the scattering is going to be the dominant process and reaches a maximum at R=40nm, while the absorption quickly decreases. The silver sphere of radii less than 20nm are hence highly efficient for absorbing light, while larger silver spheres scatter light much more efficiently.

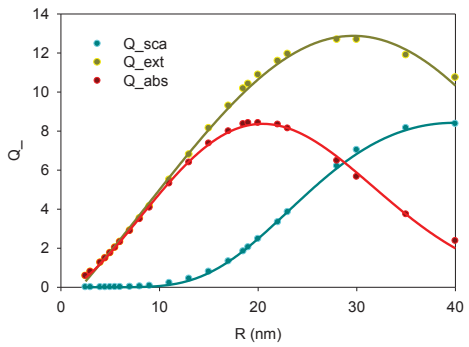

Figure 21| Absorption Q_{abs} , scattering Q_{sca} and extinction Q_{ext} efficiencies of silver nanospheres as a function of the sphere radius.

By setting the refractive index of the host medium to a higher value n=1.46 (PDMS), the absorption is to a greater maximum efficiency value occurring at a smaller size

$R_{opt} = 13nm$. The linear proportion range of the absorption efficiency is thus reduced to a smaller particle size $R < 11nm$, and the enhancement rate of the absorption, represented by the slopes of the linear proportions in Figure 22a, is also increased.

The absorption cross-section resulted in $n = 1.46$ (PDMS) in units of "normalized to" the one calculated in $n = 1$ is plotted in Figure 22 b as a function of the sphere radius. It has been found that PDMS enhances the absorption efficiency of particles with radii less than 18nm, especially for smaller particles to reach a maximum amplification at R~7nm. Thereafter the enhancement in C_{abs} decreases quickly as the particle size increases until it fades when $R = 19nm$, and the surrounding medium PDMS no longer affects the absorption cross-section. On the contrary, when the particle radius is larger than 19nm, PDMS shields the local field and reduces the absorption cross-section.

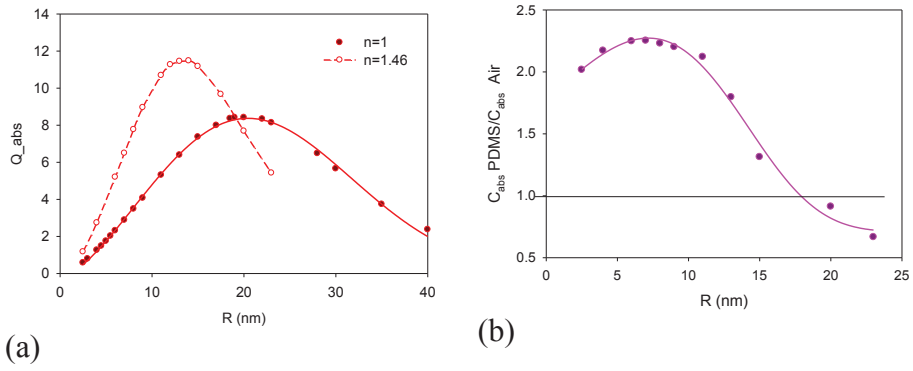

Figure 22| Absorption efficiency as a function of the radius of individual silver nanospheres embedded in medium of n=1 (solid line) and n=1.46 (dashed line). (b) The change of the absorption cross-section of the silver sphere embedded in the PDMS (n=1.46) relative to that of the same sphere surrounded by air (n=1) when the radius changes.

On the other hand, the normalized scattering cross-section is illustrated in Figure 23, the scattering cross-section is enhanced over the whole size range, especially for smaller particles. This enhancement reaches a maximum value up to nine times when $R = 8nm$. It has been also noticed that the maximum scattering efficiency that can be reached in PDMS occurs at smaller size with a greater value compared to the one found in air.

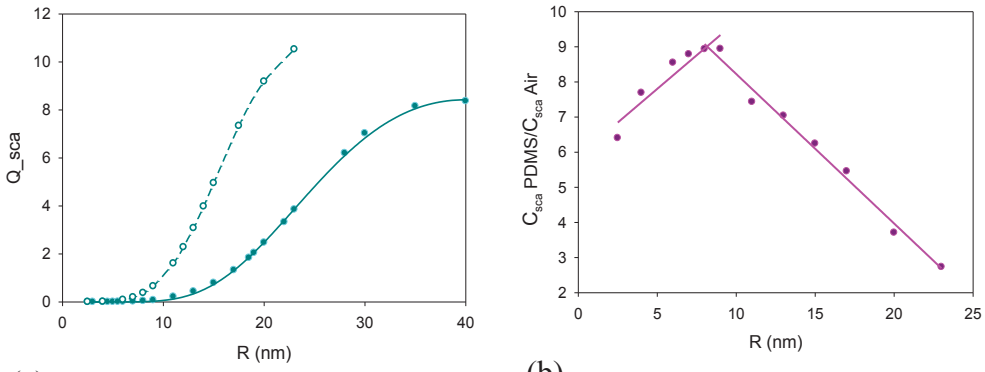

(a) (b)

Figure 23| Scattering efficiency Q_{sca} as a function of individual silver nanospheres embedded in medium of n=1 (solid line) and n=1.46 (dashed line). (b) The change of the scattering cross-section of the silver sphere embedded in the PDMS (n=1.46) relative to that of the same sphere surrounded by air (n=1) when the radius changes.

The sum of both absorption and scattering efficiencies are represented in Figure 24 illustrating the extinction efficiency as a function of particle size. The absorption dominates the extinction, excited by the dipole plasmon resonance, when $R \le 20nm$ in $n = 1$ or $R \le 13nm$ in PDMS, whereas the scattering is the dominant process for larger radii, $R \ge 30nm$ and $R \ge 20nm$ in air and PDMS, respectively.

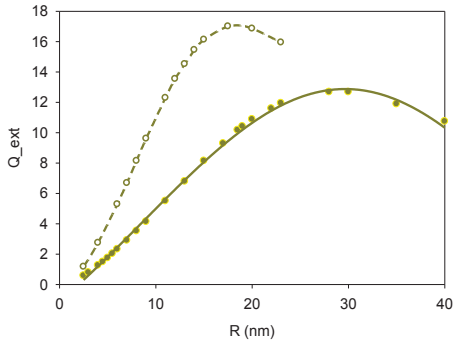

Figure 24| Extinction Q_{ext} efficiency as a function of the radius of individual silver nanospheres embedded in medium of n=1 (solid line) and n=1.46 (dashed line).

4.3.2 Resonance wavelength

The resonance wavelength is found to be insensitive to the particle size for smaller particles. The radii of these small particles are defined, in the present work, to be equal or less than the critical radius. Exceeding the critical radius, the resonance wavelength red-shifts with increasing sphere size. As the resonance wavelength depends on the size, a linear proportion between the resonance wavelength and the sphere radius is illustrated in Figure 25. Experimental measurements, revealed a similar linear proportion for single silver nanoparticles, have been presented by McFarland et al. [56].

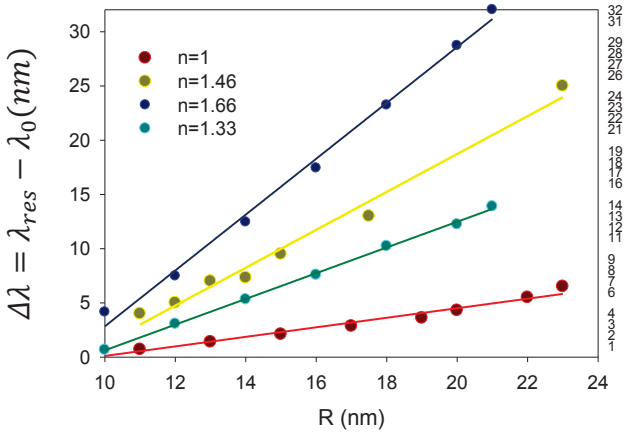

Figure 25| Resonance wavelength red-shift as a function of the silver sphere radius in various surrounding media of refractive indices $n = 1, 1.33, 1.46, 1.66$ (color online).

The magnitude of the resonance wavelength red-shift, observed when the particle size increases, is found to be strongly affected by the host medium and linearly increased with the refractive index of that medium as can be seen in Figure 26.

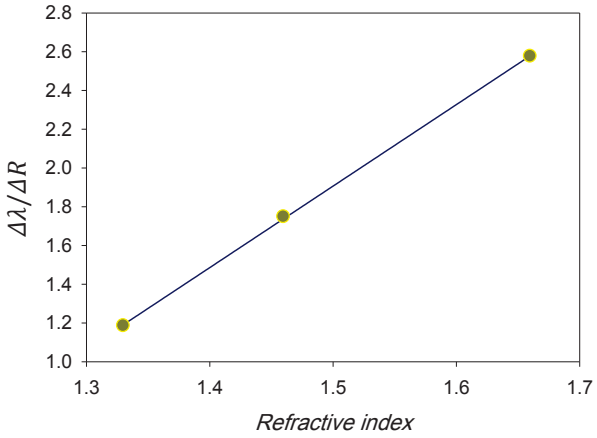

Figure 26| Sensitivity of the plasmon shift to the particle size as a function of the refractive index of the host medium.

CHAPTER 5

Optical properties of supported sphere-like silver nanoparticles in different host media

Introduction

If we place a nanoparticle on a substrate, the displacement of the electronic cloud, driven by the applied electric field of the incident light, induces a charge distribution on the substrate, which acts on the collective motion of the oscillating electrons and affects the plasmon resonance parameters [3]. For a small spherical silver nanoparticle ($\leq 50nm$), the phase retardation effect is roughly null, and the dipole plasmon resonance mode is only excited. However, when that particle is placed on a substrate, the dipole approximation is not sufficient while the metallic particle experiences different phases, attributed to the local electric field and substrate induced-field: the total field penetrating the particle may no longer be homogenous. This gives rise to multipolar excitations.

It has been found that when a spherical silver nanoparticle is deposited on a substrate, the dipole resonance wavelength red-shifts and the multipolar plasmon modes can be excited, either in a broadened spectral plasmon band or through several plasmon peaks, which are usually observed in larger particles [3]. It has been reported by Zhang et al. [18] that when the sphere touches the substrate, smooth spectra are expected. Whereas, when the sphere is separated by a distance above the substrate, well-defined features of the resonance spectrum are found. For incident polarization perpendicular to the substrate

surface, the plasmon resonance bands cover a longer region of wavelengths compared to that resulting under parallel polarization [3].

5.1 Sphere-like particles

Metallic nanoparticles, deposited on a substrate, have been used in plasmonic bio-sensing, which is based on the sensitivity of the plasmon resonance wavelength to the ambient. The plasmon resonance dependency on the refractive index of the surrounding medium is limited by the bonding between the deposited particles and the substrate, a weak bonding usually leads to unstable detection. Among the key factors affecting the plasmon resonance of a metallic nanoparticle, the contact area between the particle and the substrate is studied in this chapter for single sphere-like particles. A coupled system consisting of such particles, arranged in a one-dimensional or two-dimensional array, could offer a high enhancement of the sensitivity due to the plasmon coupling resonance.

5.2 The DDA target geometry and orientation

Optical properties of isolated sphere-like particles are simulated for different sizes, polarization directions and cut-facet areas.

The polarization direction is defined by the angle θ as schematically illustrated in Figure 27. The incident light propagates parallelly to the x axis, the incident electric field is parallel to the y axis and the rotation axis is the z axis.

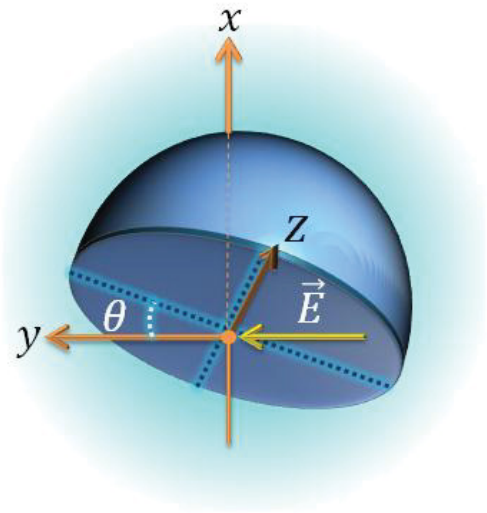

Figure 27| Schematic representation of the isolated silver sphere-like particle illustrates the particle orientation relative to the incident electric field.

A spherical silver particle merely touches the surface with a minimum contact area. By cutting the sphere, the sphere-like particle is formed, and the contact area is thus increased as depicted in Figure 28. The cut-facet (the contact area) and the height of the sphere-like nanoparticles (h) are determined by the contact angle (α) between the contact facet and the tangential of the sphere body at any contact edge.

The contact area (S) is related to the contact angle and the sphere radius by

$$S = \pi R^2 \sin^2 \alpha \tag{48}$$

where $90^o \le \alpha \le 180^o$.

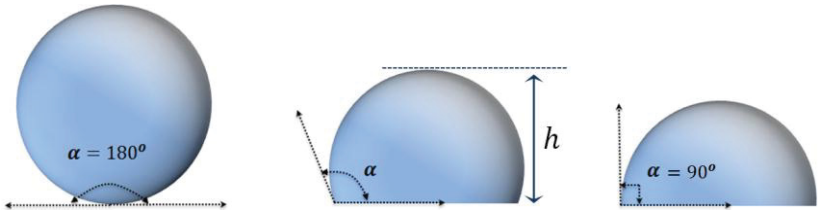

Figure 28| Schematic diagrams illustrating the contact area between the silver particle and the substrate, defined by the contact angle $90^o \le \alpha \le 180^o$.

At larger contact angles, contact areas are smaller and at the maximum angle $\alpha = 180^o$ the particle has a perfect spherical shape and merely touches the substrate. At minimum angle $\alpha = 90^o$, a hemisphere is represented and characterized by a maximum contact area equals to the sphere cross-section as can be seen in Figure 28. The height of the sphere-like particle can be calculated in terms of the contact angle and the sphere radius as

$$h = R(1-\cos(\alpha)) \tag{49}$$

5.3 Optical response of isolated sphere-like particles

For incident polarization parallel to the cut-facet of an isolated hemispherical nanoparticle ($\theta = 0^o$), the dipole plasmon resonance wavelength, characteristic of the plasmon resonance in a silver sphere of radius 20nm, red-shifts as the symmetry of the sphere is broken giving rise to a shoulder. This latter becomes better defined by increasing the cut-facet area occurring at smaller contact angles. When $\alpha = 90^o$ a hemispherical nanoparticle is yielded, and the absorption spectrum ends up with a small quadrupole plasmon band, represented by a distinct shoulder and centered at 357.5nm on

the tail of the dominant dipole plasmon band in the low wavelength side as can be seen in Figure 29.

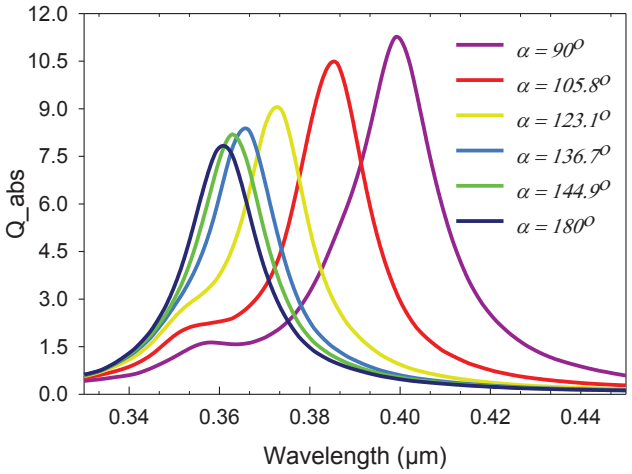

Figure 29| Absorption efficiencies of isolated particles that are defined by various contact angles (listed in the legend). The dipole plasmon band, observed in the sphere (at $\alpha = 180^{o}$), is red shifted as the contact area increases and an evolving shoulder, attributed to the quadrupole plasmon band, emerges on the tail of the dominant dipole plasmon band in the low wavelength side.

The two plasmon bands, observed in the absorption spectra of a 40 nm silver hemispherical particle under parallel polarization ($\theta = 0^{o}$), are investigated for smaller sizes as illustrated in Figure 30.

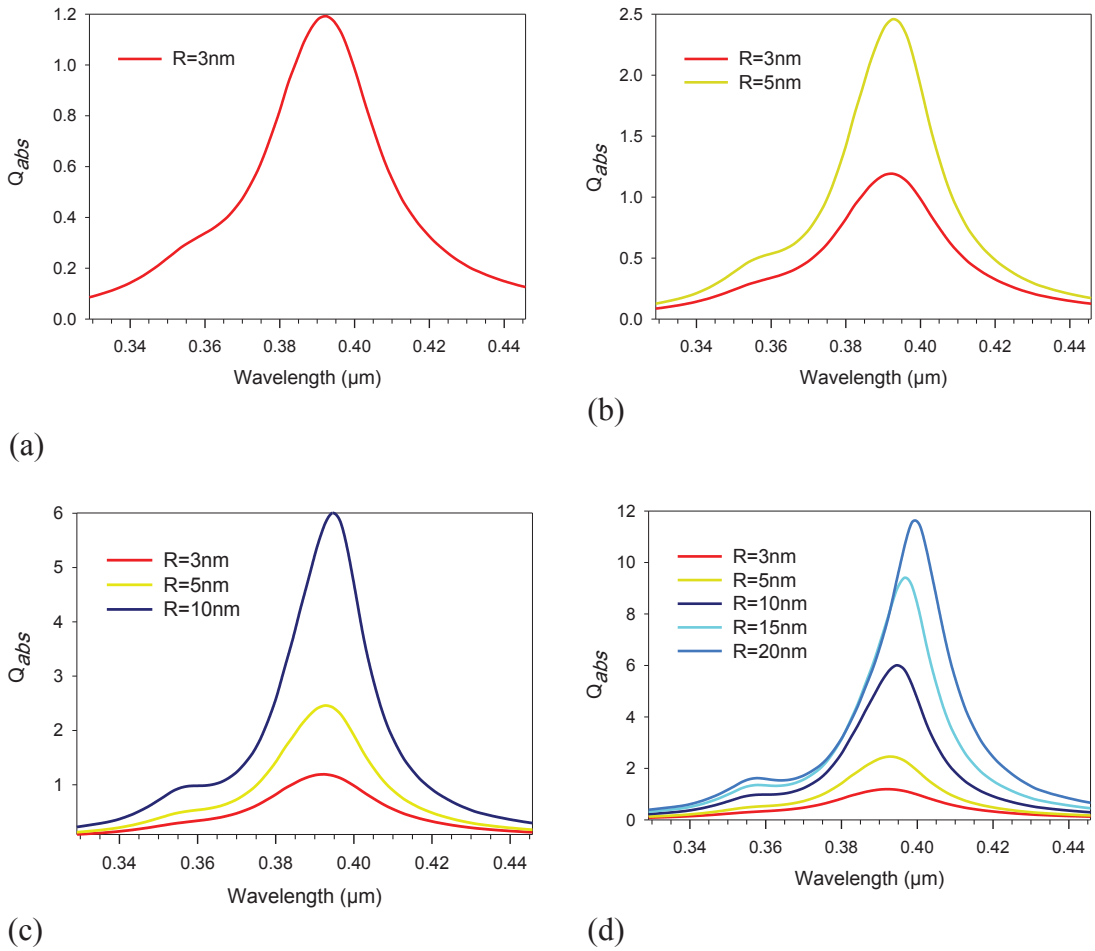

Figure 30| Absorption efficiencies of isolated hemispherical particles of various radii (listed in the legend).

The quadrupole plasmon structure is barely noticed in the spectrum of a very small hemisphere of radius 3nm (Figure 30a). This structure, centered at 358nm, is gradually evolved with increasing particle size as the phase retardation effect grows and strengthens the quadrupolar charge distribution, while the dipole plasmon resonance wavelength red-shifts as $R > 10nm$ (see 4.3) and the band gets sharper as shown in Figure 30b, c, d.

The aforementioned two plasmon bands are studied under various incident polarizations. A strong dependency of the dipole plasmon band on the polarization is revealed in Figure 31. Increasing θ, the intensity of the dipole band gradually decreases while a second band

grows up at a lower wavelength (332.5nm) with small amplitude relative to that of the dipole band. These bands evolve in the opposite way when varying the angle θ, due to the opposite responses, resulted from the electric field projections on both the parallel and perpendicular directions to the contact facet. When $\theta = 90^o$, a well-defined band is observed at the lower wavelength and the dipole plasmon peak disappears.

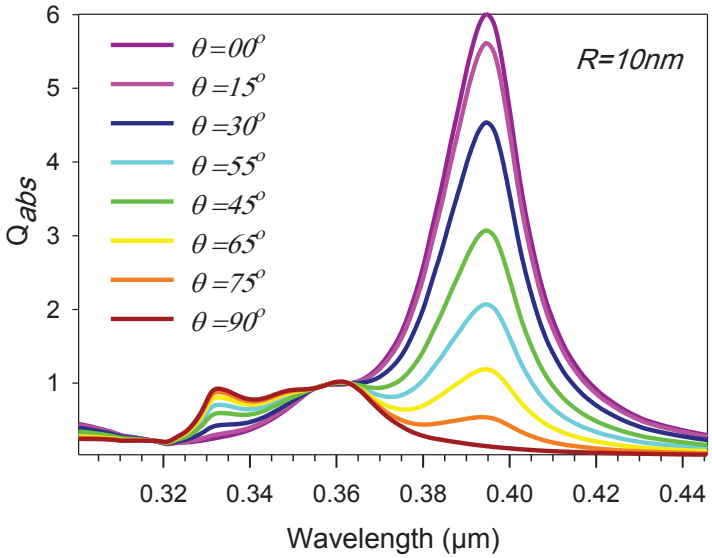

Figure 31| Absorption efficiencies of isolated hemispherical particles of radius $R = 10nm$, under various polarizations determined by θ (listed in the legend).

The resonance wavelength of the quadrupole plasmon band is barely affected by increasing θ and red-shifted from 357.7nm to 361nm. When $\theta = 55^o$, another peaks at 349.5nm emerges and gradually evolves as θ increases to 90^o, as can be seen in Figure 32a, b.

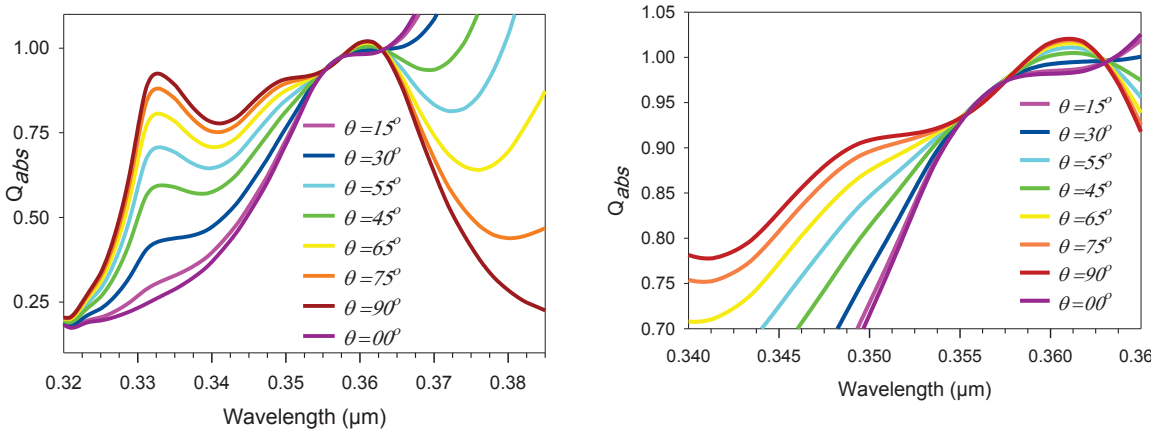

(a) (b)

Figure 32| Absorption efficiencies of isolated hemispherical particles of radii $R=10nm$, under various polarizations (listed in the legend).

Eventually, the quadrupole plasmon band, observed under parallel polarization ($\theta=0^o$), roughly maintains the same resonance wavelength and amplitude under any polarization characterizing any isolated silver sphere-like particle. It also gets more pronounced as the sphere-like geometry is more deviated from the perfect spherical symmetry. Thus, from now on we will refer to this band as the **shape band**.

5.4 Substrate effect

An indium tin oxide (ITO) substrate is firstly used to study the effect of the substrate on the plasmon resonances of the silver nanoparticles, for incident polarization parallel to the contact facet. The ITO substrate was chosen because it is one of the most widely used transparent conducting oxides, with a relatively high refractive index (varies around $2.15+i\,0.0044$ in the visible region) ensuring a good contrast between the substrate and the surrounding medium (air or vacuum). Its optical constants were taken from ref. [57].

The substrate thickness $l = \frac{h}{2}$ equals to half of the sphere-like particle height, as drawn in Figure 33.

Figure 33| Schematic diagram showing the substrate thickness l relative to the particle height h , which is defined as $h = 2l$.

The absorption spectra of isolated sphere-like particles, plotted in Figure 29 and revealed the shape band (shoulder) on the tail of the dominant dipole band, are split into two well-defined plasmon resonance bands due to the substrate effect as can be seen in Figure 34.

The shape band is still observed at a slightly shorter wavelength than that of the perfect sphere. By increasing the contact area (decreasing the contact angle), the shape band is blue-shifted whereas the dipole plasmon band is red-shifted with a higher amplitude. Thus, the energy difference between the two bands increases with the contact area. At the contact angle $\alpha \leq 123.1^o$, a small shoulder between the shape and dipole bands begins emerging and evolves with increasing contact area to form a distinct band when $\alpha = 90^o$ as illustrated in Figure 35. From now on we will refer to this band as the **substrate band**, which is ascribed to the substrate effect

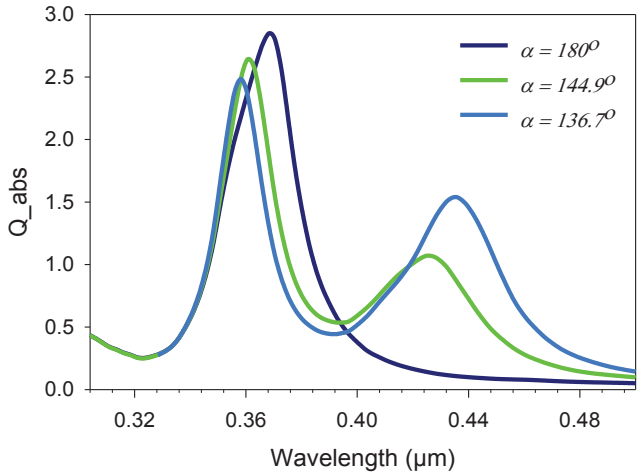

Figure 34| Dependency of the absorption efficiency of supported particles on the contact angle (contact angle listed in the legend). The band at longer wavelengths is attributed to the dipole plasmon excitation, while the shape bands are observed at shorter wavelengths.

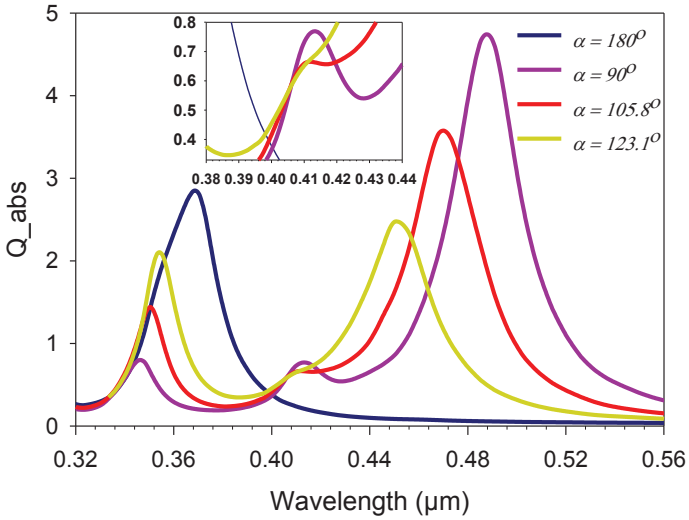

Figure 35| Dependency of the absorption efficiency of the supported particles on the contact angle (contact angle listed in the legend). The plasmon absorption bands, observed in isolated sphere-like particles, are split into two well-defined plasmon resonance bands due to the substrate effect. The shoulder between the two aforementioned bands is attributed to the substrate effect and is observed when $\alpha \leq 123.1^{o}$.

5.4.1 Resonance wavelength of the dipole band

By increasing the contact area, the sphere-like geometry is more deviated from the perfect spherical symmetry, which decouples the sphere-like particle from the substrate and red-shifts the plasmon resonance wavelengths. Consequently, the dominant plasmon band of sphere-like particles, observed in Figure 29, is red-shifted giving rise to the dipole plasmon band [3]. The dipole plasmon mode is therefore more pronounced at the minimum contact angle $\alpha = 90^{o}$ (hemisphere) as revealed in the absorption spectra in Figure 34.

Plasmon shifts of the dipole band are illustrated in Figure 36 as a function of the particle height h. We found that the resonance wavelength linearly decreases with the particle height in both cases of isolated and supported nanoparticles. Note that a larger contact facet corresponds to a smaller particle height h.

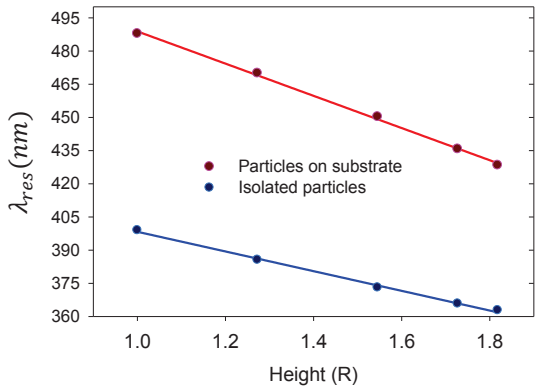

Figure 36| Dependency of the dipole resonance wavelength on the height of ; the sphere-likes particle that are placed on a substrate of thickness equals to half of the sphere-like particle height(red straight line), the isolated sphere-like particles(blue straight line).

The substrate effect on the plasmon shift magnitude is determined by the difference of the straight lines' slopes; these slopes represent the rate of the red-shift with increasing contact area (decreasing particle height). This rate is 44.5 for isolated sphere-like particles against 72.8 when those particles are located on a substrate (such as the ITO substrate). Thus, the plasmon peak shifts cover a more extended wavelength region when the particle is on a substrate as compared to the situation when the sphere-like particle is isolated.

5.4.2 Resonance wavelength of the substrate band

In the hemispherical nanoparticle ($R = 20nm$) deposited on the ITO substrate, the multipolar plasmon resonance gives rise to the substrate band. As the contact angle increases, the dipole plasmon band blue-shifts until it incorporates the substrate band into a smooth and broadened band at contact angle $\alpha = 136^o$ or larger angles (see Figure 34 and Figure 35). When a perfect sphere touches the substrate, at $\alpha = 180^o$, the plasmon band curve is smoothed and broadened with a width of 30nm against 20nm for the same isolated sphere while the peak position is red-shifted from 360nm to 369nm (see Figure 29 and Figure 34).

5.4.3 Resonance wavelength of the shape band

The shape band is evident in a well-defined structure only in the presence of the substrate effect (Figure 34), its resonance peak linearly blue-shifts as the particle height decreases

(the contact area increases). The rate of the change is 22.2 (line slope), as illustrated in Figure 37, and it covers a narrow spectral region around 25nm between the two marginal cases (the perfect spherical particle at $\alpha = 180^o$, the hemispherical particle at $\alpha = 90^o$).

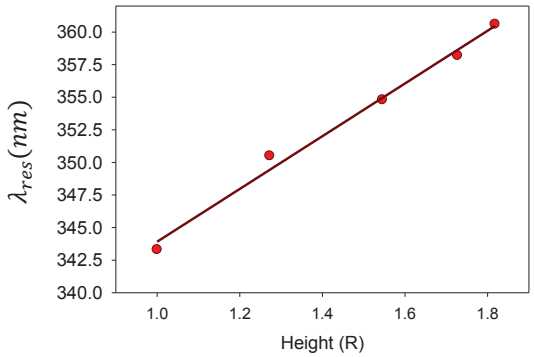

Figure 37| Dependency of the resonance wavelength of the shape band on the height of sphere-like particles, which are placed on a substrate of thickness equals to half of the sphere-like particle height.

5.5 Substrate effect and particle size

In order to figure out the dependency of the substrate effect on the size of a sphere, sphere-like and hemisphere silver particles defined by the contact angles $\alpha = 180^o, 123.06^o, 90^o$, respectively, are examined.

We simulated those particles on a magnesium oxide (MgO) substrate with different radii $R = 5nm, 10nm, 20nm$. The MgO substrate is a dielectric crystal commonly utilized for optical measurements with a refractive index varies around $1.76 + i\,0$ in the visible region, its optical constants were taken from ref. [58]. The absorption spectra of these three particles were calculated and plotted in Figure 38.

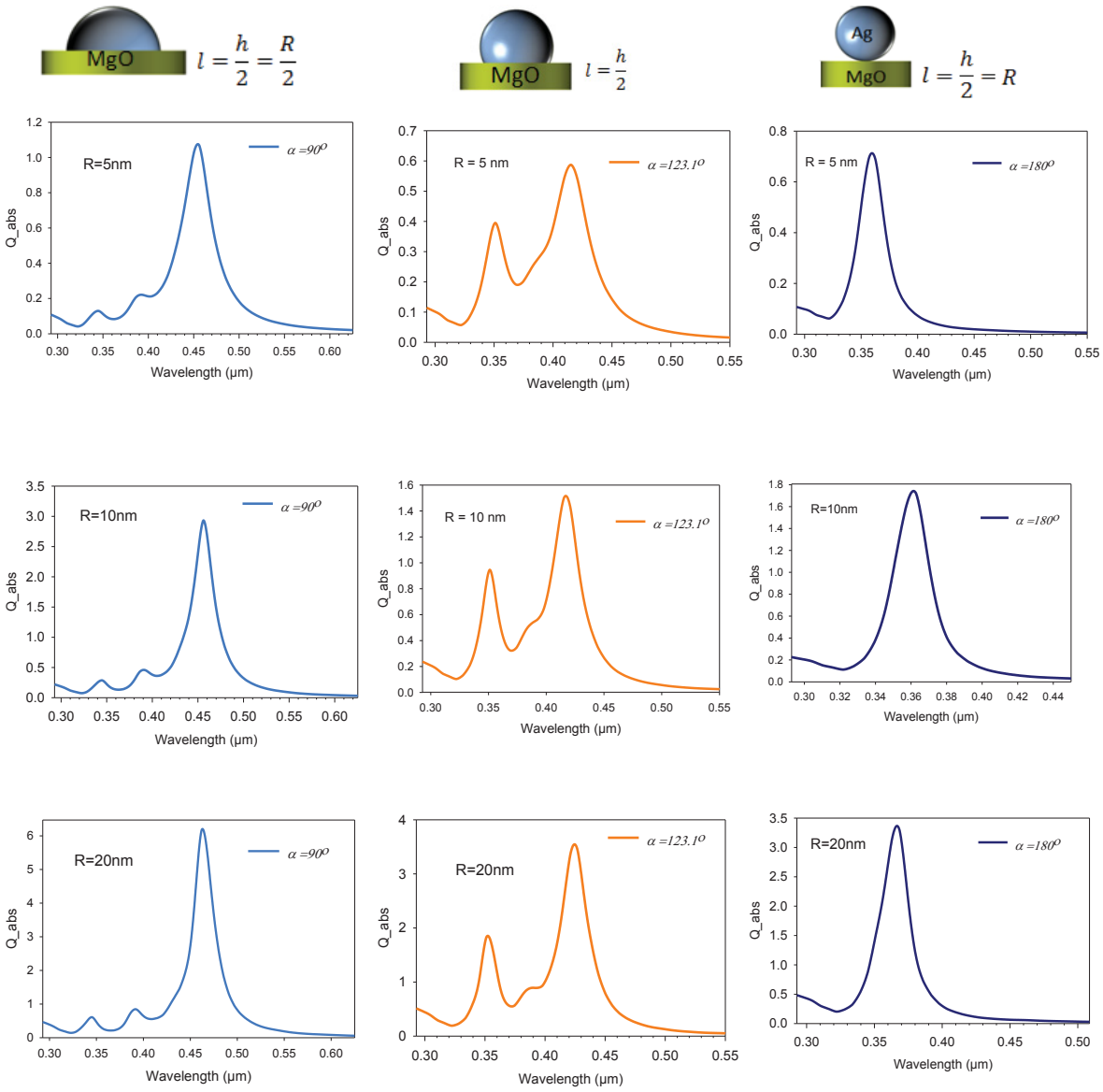

Figure 38| Absorption spectra of spherical, sphere-like and hemispherical particles as defined by the contact angles $\alpha = 180^o, 123.06^o, 90^o$, respectively, located on a magnesium oxide (MgO) substrate, and with different radii $R = 5nm, 10nm, 20nm$.

The particles originated from spheres of radii $R = 5nm, 10nm, 20nm$,depicted in Figure 38, reveal the similar structures of the absorption spectra that have been already observed

(see Figure 34 and Figure 35). By decreasing the particle radius, the plasmon bands attributed to all particles are broadened. This also smooths out the spectrum and diminishes the details of the plasmon bands structures, which is evident in spectrum of the sphere-like particle of radius $R = 5nm$. On the other hand, the substrate band, observed in the sphere-like particle of radius $R = 20nm$, is washed out with decreasing radius and transformed to a small shoulder incorporated into the tail of the dominant dipole band when $R = 5nm$, the dipole band is broadened as the imaginary part of the silver dielectric function increases (see 4.2.1).

The shape and substrate multipolar plasmon bands in all sphere-like particles remain at the same peak positions independently from the size changes as shown in Figure 39 a. This result is supported by the hemispheres spectra as illustrated in the inset in Figure 39 b.

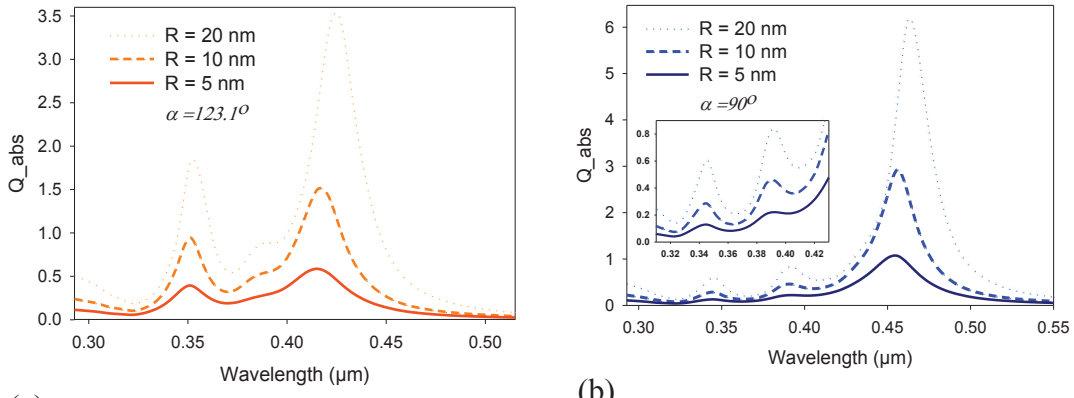

(a) (b)

Figure 39| Diagrams illustrating plasmon bands of supported (a) sphere-like particles defined by $\alpha = 123.06^{o}$ of various radii (listed in the legend) and (b) hemispherical particles, which are placed on a MgO substrate of thickness $l = h/2$

However, the resonance wavelength of the dipole band slightly red-shifts with increasing radius of the sphere-like particle. In the case of a perfect sphere the plasmon resonance wavelength is slightly red-shifted with the sphere size by 7nm when R increases from 5nm to 20nm.

5.6 The effect of the substrate thickness

Sphere-like particles, that are derived from a sphere of radius $R = 20nm$ and defined by the contact angle $\alpha = 123.06^o$, are placed on a MgO substrates of various thicknesses $l = h/2,\ h,\ 2h,\ 4h$.

The wavelength of the dipole plasmon resonance in the sphere-like particles red-shifts with increasing thickness of the substrate, while the absorption efficiency is intensely attenuated, as can be seen in Figure 40a.

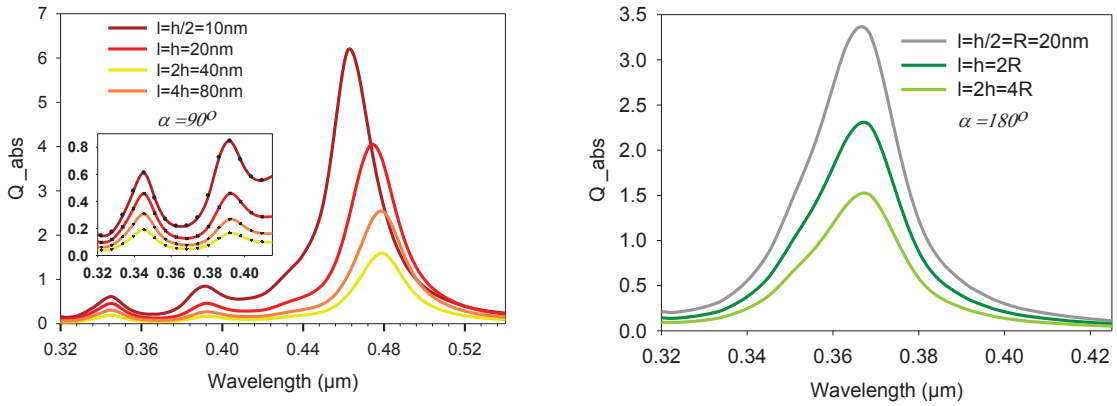

(a) (b)

Figure 40| Absorption spectra illustrating the plasmon resonance wavelength of the various plasmon bands in (a) a sphere-like particle defined by $\alpha = 123.06^o$, and (b) spherical particles of radius $R = 20nm$, which are placed on a MgO substrate of various thicknesses $l = h/2,\ h,\ 2h,\ 4h$ (listed in the legend).

The plasmon resonance wavelength in a perfect sphere as well as the shape and substrate bands pertaining to sphere-like particles remain, however, at the their spectral positions independently from the substrate thickness. On the other hand, the absorption efficiencies are quickly reduced with increasing thickness of the substrates as can be seen in the inset in Figure 40a and in Figure 40b.

5.7 The effect of the substrate material

A silver sphere-like particle, derived from sphere of $R = 20nm$ and generated at the contact angle $\alpha = 123.06^o$ with height $h = 37.2nm$, is placed on a substrate of thickness $l = \frac{h}{2}$ and depicted in Figure 41, and the refractive index of the medium surrounding the particle-substrate system is set to unity.

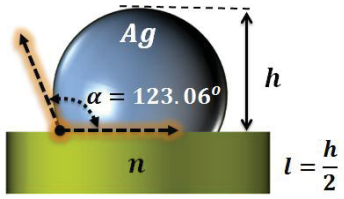

Figure 41| Schematic representation of the silver sphere -like particle, defined by the contact angle $\alpha = 123.06^o$, is placed on various substrates of different n and of the same thickness fixed at $l = \frac{h}{2}$.

This system is simulated for different dielectric substrate materials of refractive indices range between $n = 1.23$ and $n = 2.57$, and the calculated absorption spectra are plotted in Figure 42. As the dielectric constant of the substrate increases, the dipole plasmon band is reduced to lower efficiencies, gets broadened and is quickly red-shifted.

It is worth mentioning that the substrate plasmon band was not observed for smaller refractive indices of the substrate $n \leq 1.46$.

When $n = 1.69$, the substrate band emerges as a small shoulder between the shape and dipole bands. Then, this shoulder is rapidly red-shifted with increasing substrate refractive index and gradually evolves into a most defined structure when $n = 1.92$ before it begins to incorporate into the tail of the dominant dipole plasmon band, which ends up with a smooth broadened for larger n of the substrate.

The shape band is shown in the inset in Figure 42. It evolves rapidly with increasing refractive index of the substrate, the bandwidth increases and its resonance wavelength is slightly red-shifted by around 5nm.

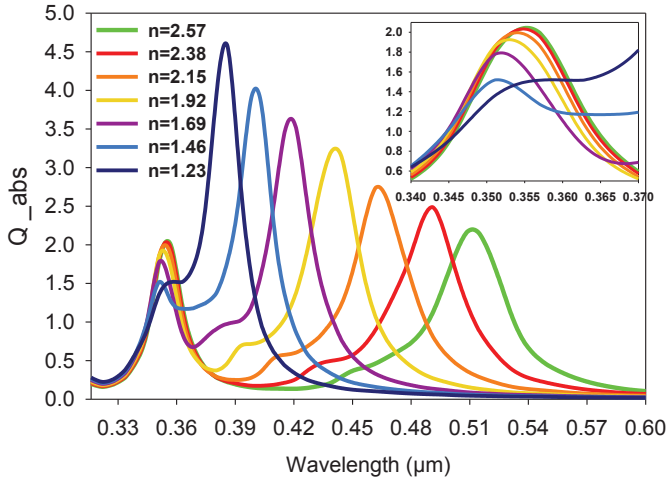

Figure 42| Absorption spectra illustrating the dependence of the plasmon resonance wavelength of the various plasmon bands in a sphere-like particle on the dielectric constant of a substrate. The sphere-like particle is defined by $\alpha = 123.06^{o}$, derived from a sphere of radius $R = 20nm$ and placed on substrates of various materials (n listed in the legend), the refractive index of the medium surrounding the particle-substrate system is set to unity.

The sensitivity of the dipole resonance wavelength to the substrate material is demonstrated by successive red-shifts of resonance wavelength in linear proportion with increasing dielectric constant of the substrate, as shown in Figure 43a, whereas the absorption efficiency is linearly decreased with refractive index of the substrate, as illustrated in Figure 43 b.

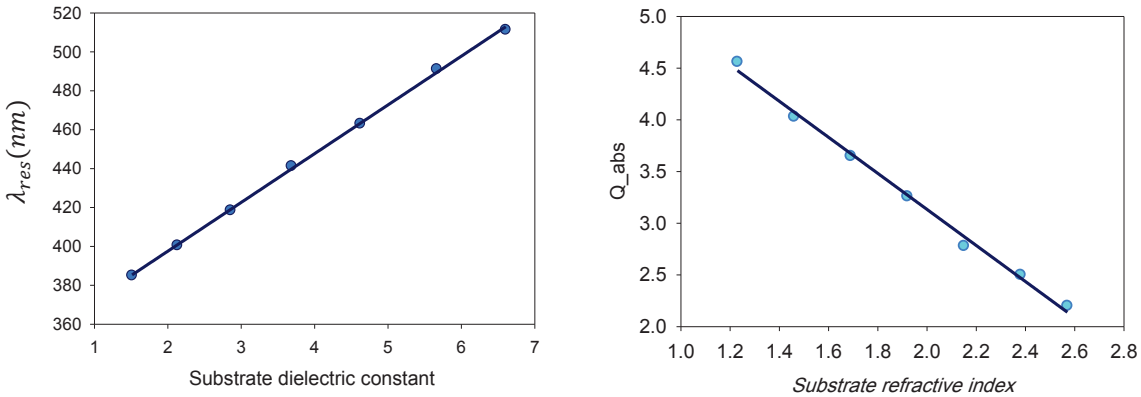

(a) (b)

Figure 43| (a) dipole resonance wavelength, observed in a sphere-like particle defined by $\alpha = 123.06^{o}$, as a function of the dielectric constant of the substrate, (b) Absorption efficiency of dipole plasmon resonance band as a function of the refractive index of the substrate.

5.8 The contrast in refractive indices of the substrate and the host medium

A silver sphere-like particle, derived from sphere of $R = 20nm$ and generated at the contact angle $\alpha = 123.06^{o}$ with height $h = 37.2nm$, is placed on a substrate of thickness $l = \frac{h}{2}$ and refractive index $n = 1.92$ and is schematically depicted in Figure 41.

i) **When the refractive index of the surrounding medium** $n = 1, 1.23, 1.46, 1.69$ **is less than that of the substrate** $n = 1.92$, the absorption spectra of the sphere-like particle on a substrate are shown in Figure 44a. The resonance wavelengths of both dipole and shape plasmon bands, excited by dipole and multipolar modes respectively, are red-shifted with increasing refractive index of the host medium. The spectral range separating their peak positions decreases linearly with the refractive index of the host medium as illustrated in Figure 44b. This relationship is attributed to the red-shift of the shape plasmon band that moves faster than the dipole plasmon band which is broadened with increasing n_{medium}.

The substrate plasmon excitation is revealed in a single plasmon band when $n_{medium} = 1, 1.23$, where the contrast in the refractive indices of the substrate and medium increases as illustrated in Figure 44a.

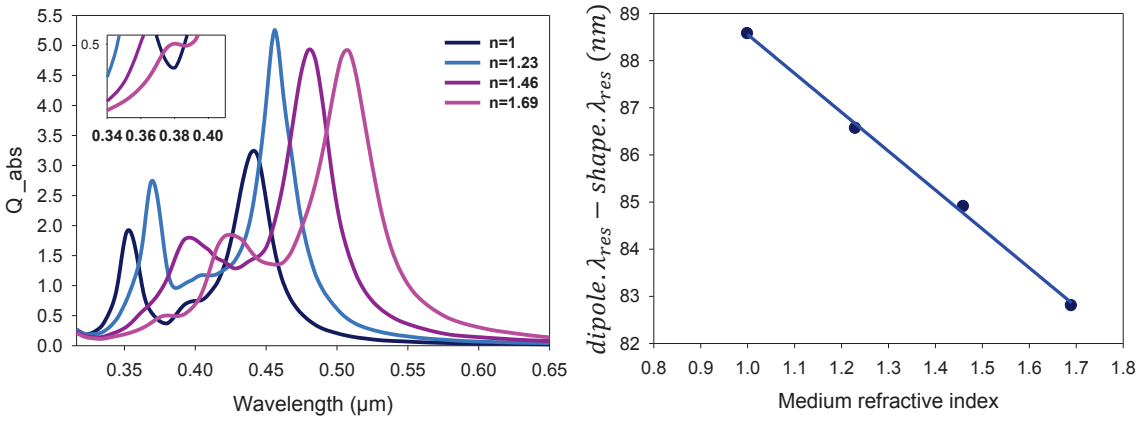

(a) (b)

Figure 44| (a)Absorption spectra illustrating the dependency of the plasmon resonance bands in a sphere-like particle, placed on a substrate of $n = 1.92$, on the refractive index of the host medium (n listed in the legend $< n = 1.92$). (b) Spectral range between the dipole and shape resonance wavelengths as a function of the refractive index of the host medium.

When the refractive index of the host medium $n_{medium} = 1.46, 1.69$, the shape plasmon band and the shoulder representing the substrate plasmon band overlap. Consequently, the shape band gets broadened, as shown in Figure 44a. It is noticed that a higher-polar substrate band emerged at 380nm when the refractive index of medium $n = 1.69$ as shown in the inset in Figure 44a.

ii) When the refractive index of the surrounding medium $n = 2.15, 2.38, 2.57, 2.86$ **is larger than that of the substrate** $n = 1.92$, the inset in Figure 45a shows the higher-polar excitation due to the substrate effect emerging in two well-separated plasmon structures, the small band at a higher energy being centered at resonance wavelength 380nm, which is independent of the refractive index of the host medium.

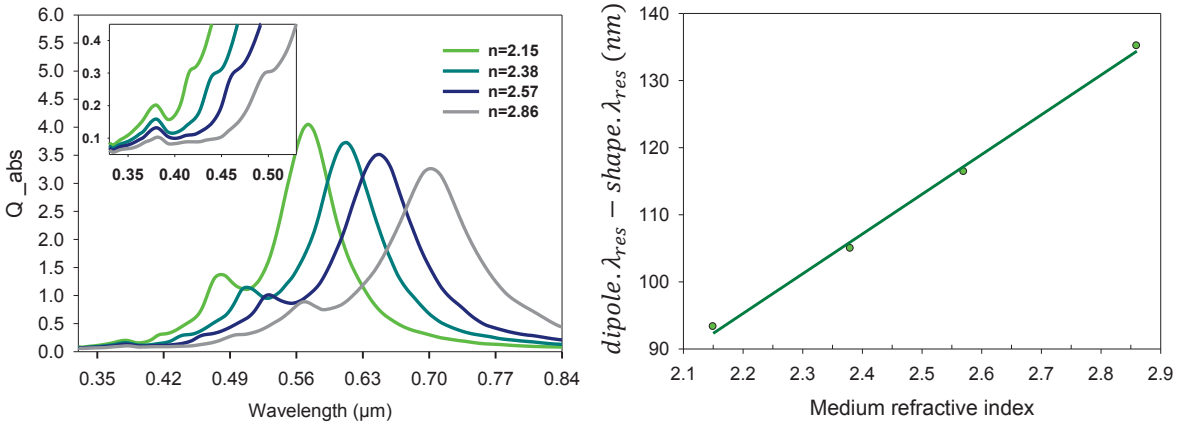

(a) (b)

Figure 45| (a) Absorption spectra illustrating the dependency of the various plasmon bands in a sphere-like particle, placed on a substrate of $n = 1.92$, on the refractive index of the host medium (n listed in the legend $> n = 1.92$). (b) Spectral range between the dipole and shape resonance wavelengths as a function of the refractive index of the host medium.

The other quadrupole plasmon shoulder is located at the lower energy and red-shifted with refractive index of the surrounding medium.

The resonance wavelengths of both dipole and shape plasmon bands red-shift with increasing refractive index of the host medium. In contrast with the first case when $n_{substrate} > n_{medium}$, the spectral range separating peak positions of the dipole and shape bands increases linearly with increasing refractive index of the host medium as illustrated in Figure 45b. This proportion is attributed to a resonance wavelength of the dipole plasmon band that red-shifts much faster than the shape resonance wavelength. The dipole plasmon band width gets broadened with the refractive index of the host medium, while the absorption efficiencies of both the dipole and shape plasmon bands decrease.

CHAPTER 6

Host medium effect on the dipole plasmon coupling resonance in silver linear chains

In order to study the effect of the dielectric environment on the plasmon resonance parameters of coupled silver nanoparticles, a study of the optical response of the individual silver nanospheres immersed in various host media has been done in chapter 4. This will be an appropriate introduction for the investigation of the relationship between the host medium and the dipole plasmon coupling mechanism occurring among interacting small silver nanoparticles arranged in one-dimensional, two-dimensional and three-dimensional arrays.

Introduction

The dipole plasmon resonance wavelength of a silver nanosphere can be red-shifted by increasing the refractive index of the host medium. The tunability of the resonance wavelength with the sphere size is however too limited for diverse applications. The range of the tunability is furthermore found to be restricted by the dielectric constant of the host medium (see 4.3.2).

By exploiting the plasmon coupling between interacting nanoparticles, the tunability of the plasmon parameters can be highly enhanced, as the plasmon coupling are strongly dependent on the interparticle separation.

The plasmon parameters determining the optical properties of a coupled system consisting of nanospheres, aligned in a linear chain, are studied in this chapter. The interparticle separation, the host medium and the particle size are treated as variables for different incident polarizations to figure out their effects on the plasmon coupling parameters. The results can be generalized to any (large) number of component particles composing the linear chain.

6.1 Target geometry and orientation

The calculations are done for one-dimensional linear chains consisting of equal-sized and equally separated silver nanospheres embedded in various host media.

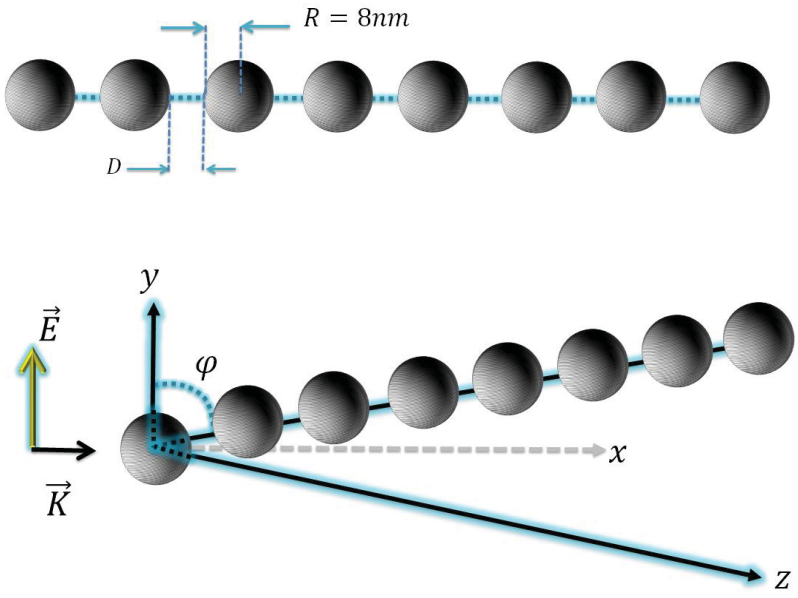

Figure 46| Schematic representation of a linear chain composed of 8 silver spheres (diameter $2R$) with interparticle separation D, the x-y plane is the plane of incidence, the incident electric field is parallel to the y axis, φ is the polarization angle between the electric field and the chain axis in the y-z plane.

The particles system is irradiated with an electromagnetic plane wave. The structure and the orientation of the chains are depicted in Figure 46, the plane of incidence is set to be the x-y plane and the incident electric field is parallel to the plane of incidence (the y axis). The light is thus p-polarized; φ determines the polarization angle between the electric field and the axis of the linear array "chain axis", and the interparticle separation "spacing" D is the border-to-border distance between nearest-neighbor particles. D is usually defined in terms of the sphere radius.

6.2 Chain size

As found in (4.3.1), the extinction process produced by a single 8nm silver sphere is dominated by the absorption and the scattering is negligible as illustrated in Figure 22 and Figure 23. Therefore the absorption spectra are assigned to the spectral representation of the dipole plasmon resonance.

The technical capability of the DDA method for simulating any target is restricted by computational resources (memory and processor requirements), and eventually by the size of the target. At the same time, it is necessary to represent the chain with a sufficient number of spheres so that the plasmon parameters, especially resonance wavelength and plasmon bandwidth, become insensitive or independent of the chain size. With the aim to better find the convenient number that satisfies the two requirements, several chains consisting of different number of identical spheres of 8nm in radius separated by the interparticle separation $D = R/2$ were simulated in PDMS ($n = 1.46$) as embedding material, under parallel and perpendicular polarizations. The absorption spectra are shown in Figure 47.

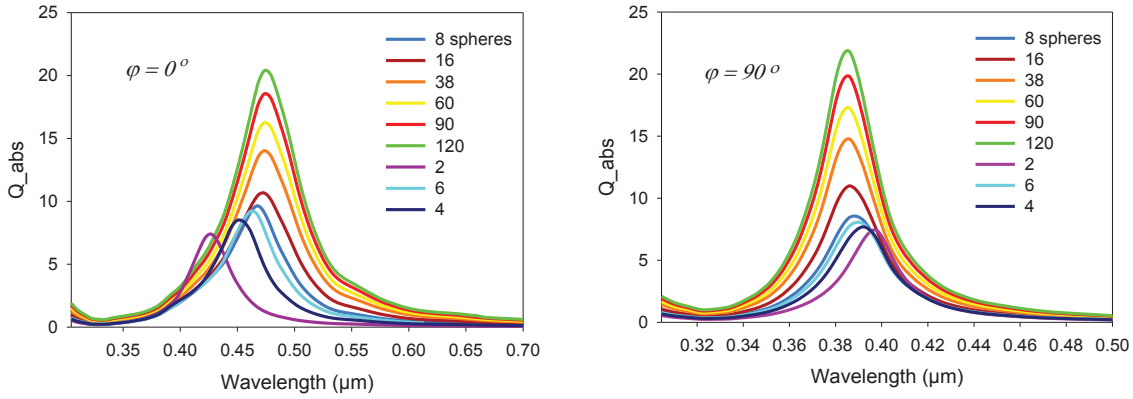

(a) (b)

Figure 47| Absorption spectra of linear chains composed of various number of silver spheres (listed in the legends) , (a) under parallel polarization ($\varphi = 0^o$), the resonance wavelength of the chain red-shifts with increasing number of component spheres, (b) under perpendicular polarization ($\varphi = 90^o$), the resonance wavelength of the chain blue-shifts with increasing number of component spheres. It has been found that the resonance wavelength becomes practically independent of the spheres number when the chain consists of 8 spheres or more.

The resonance wavelengths of chains consisting of 2, 4 and 6 spheres suffer appreciable shifts towards the resonance wavelength that is attributed to the longer chains, which share the same resonance wavelength that becomes independent of the chain size. Under perpendicular polarization, the resonance wavelength (386nm) and bandwidth (30nm) are both independent of the chain size when we have 8 or more spheres. Under parallel polarization, the plasmon resonance of 8 spheres occurs at 467.8nm, which is slightly deviated from the resonance wavelength 473.6nm found for the longer chain consisting of 120 spheres and extending over $2\mu m$. The band width of 8 spheres, 60.5nm, is also very close to that calculated for the longer chains consisting of 16 spheres or more (65.5nm).

Due to these satisfactory convergences and the reasonable computational costs, the chain consisting of 8 spheres is chosen to be a representative of what is studied in this chapter.

Each sphere of radius 8nm is represented by 14,328 dipoles yielding a fine interdipole separation $d = 0.53nm$ for the DDA target. This large number is also considered to avoid the spurious surface effect (see 3.6).

6.3 The effect of the dielectric environment on near-field interactions and plasmon coupling

The dependency of the plasmon coupling on interparticle distance in the near-field range is studied at various polarization angles (parallel, oblique and perpendicular). The calculations are repeated in four different host media of refractive indices; $n = 1$ (air), $n = 1.33$ (water), $n = 1.46$ (PDMS) and $n = 1.66$. The effect of the interparticle spacing will be concurrently investigated with the host medium effect on the plasmon coupling.

It was found that the plasmon resonance energy shifted to either shorter or longer wavelengths as the interparticle spacing decreases depending on the electric field direction, i.e., whether it is perpendicular or parallel to the chain axis, respectively [59].

6.4 Under parallel polarization

The longitudinal plasmon resonance wavelength is red-shifted as the interparticle spacing decreases, as shown in Figure 48.

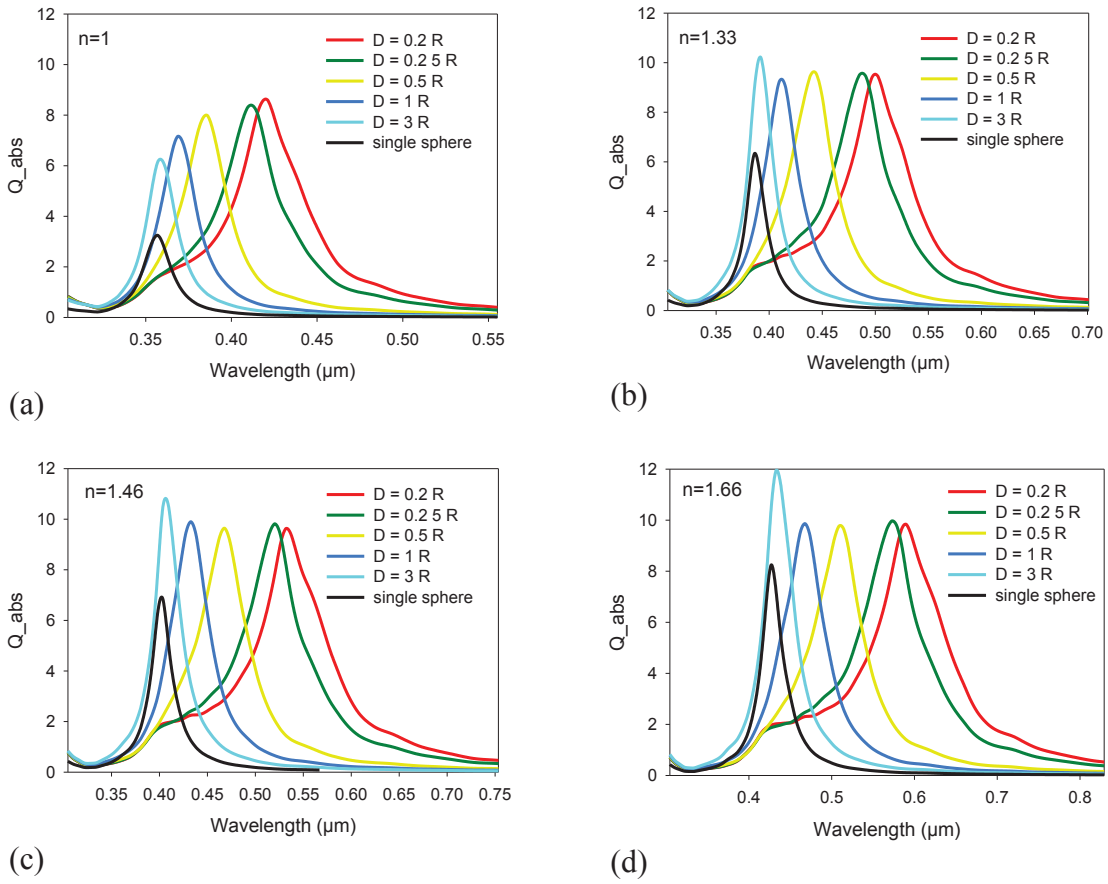

Figure 48| Absorption spectra of silver linear chains under parallel polarization, at different interparticle separations D (listed in the legends) and immersed in various embedding materials of refractive indices (a) $n=1$ (b) $n=1.33$ (c) $n=1.46$ (d) $n=1.66$. These diagrams show that the resonance wavelength is red-shifted as the interparticle spacing decreases.

As the interparticle spacing decreases, the absorption plasmon bandwidth gets broadened in all media, due to the overlap of the local electric fields between neighbouring particles contributing to the coupling [60].

6.4.1 Absorption cross-section

The absorption efficiency of the chain in host medium of $n=1$, reaches a maximum around 8.6 at the smallest interparticle separation $D=R/5=1.6nm$, and then gradually decreases when the separation increases . On the contrary, in the other media of refractive indices larger than unity, the absorption efficiency tends to have the same value of 9.6 ± 0.28 for the smaller interparticle distances $D\le R$, before getting greater values once the interparticle distance is increased to $D=3R$ .Those results are illustrated in Figure 49 showing that the absorption is getting stronger in the media with higher refractive indices at larger interparticle spacing $D=3R$.

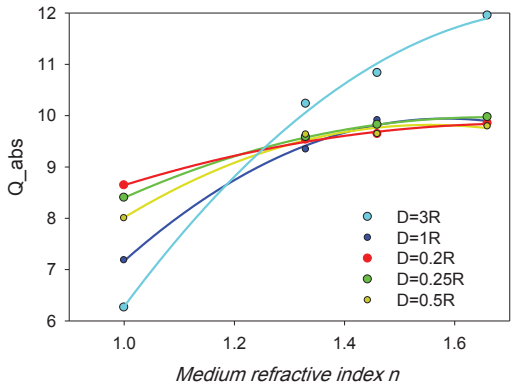

Figure 49| Absorption efficiencies of various chains at different interparticle separations D (listed in the legends) as a function of the refractive index of the host medium. Absorption efficiencies at all interparticle separations are proportional to the refractive index of the medium.

It is noticed that the coupling enhances the absorption efficiency with respect to that of the single sphere in all host media (Figure 48).

6.4.2 Plasmon resonance wavelength

Introduction

Jain et al. have derived a universal plasmon scaling behaviour [10], according to the so-called plasmon ruler equation (Eq. 50). This equation can be exploited to estimate the interparticle separation in a metallic dimer, based on the plasmon shift that is provided by experimental measurements, under parallel polarization when the longitudinal dipole plasmon mode is excited.

$$\frac{\Delta\lambda}{\lambda_0} \approx 0.18 \exp\left(\frac{-\frac{D}{2R}}{b}\right) \tag{50}$$

where $\frac{\Delta\lambda}{\lambda_0}$ is the fractional plasmon shift, and $\Delta\lambda = \lambda_{res} - \lambda_0$ where λ_{res} is the resonance wavelength of longitudinal plasmon coupling and λ_0 is the resonance wavelength for the single sphere. The decay constant $b = 0.23$. According to the authors the universality of the exponential behaviour relies on the fact that the decay constant is independent from the nanoparticle size, metal type, shape or the host medium.

Plasmon resonance wavelength red-shift

The fractional plasmon shift in silver chains embedded in a host medium of n=1.66, plotted in Figure 50 (see Figure 48d) exhibits the same universal decay trend. The decay constant that is found, to be $b = 0.235$, is similar in value to that of the universal scaling trend of the distance decay of plasmon coupling in the gold dimer (about 42nm in diameter) embedded in a host medium of 1.6, which is experimentally found by Reinhard

et al. [61] and theoretically calculated by Jain et al. The magnitude of the plasmon shift observed in the silver chain is found to be larger ($a = 0.5521$).

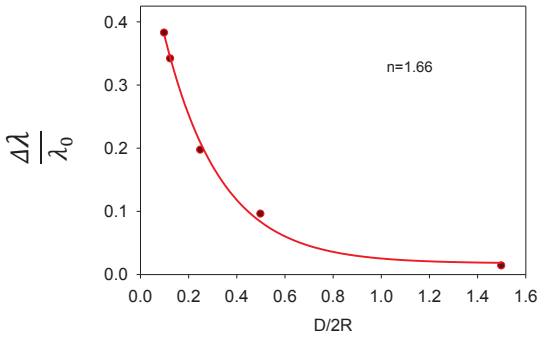

Figure 50| Fractional plasmon shift as a function of the interparticle separation in a linear chain in units of component sphere diameter, when the chain is immersed in a host medium of refractive index $n = 1.66$. The solid curve is fitted to the single-exponential decay $y = y_0 + a\exp(-x/b)$ where $b = 0.235 \pm 0.026$ and $a = 0.5521$.

The universality of the exponential behaviour supposes that the decay constant $b \simeq 0.23$ is independent from the host medium [10]. However, the decay constant of the silver chain slightly varies depending on the host media as can be seen in Figure 51, where the constant decays $b = 0.185,\ 0.206,\ 0.221$ are calculated in the host media $n = 1,\ 1.33,\ 1.46$, respectively. It is worth mentioning that the constant decay of the fractional plasmon shift of a trimer of gold nanospheres of 5nm radius, embedded in host medium of $n = 1.33$, is found to be $b = 0.21$ by Jain et al. [12].

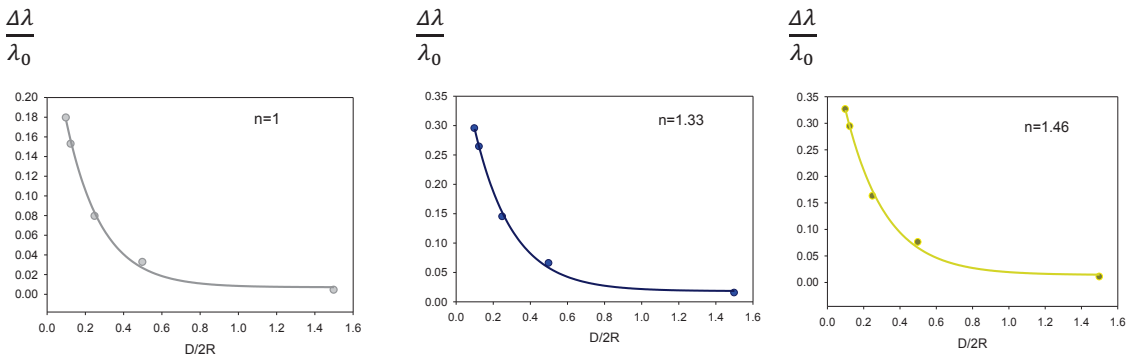

Figure 51| Fractional plasmon shift as a function of the interparticle separation in a linear chain in units of component sphere diameter. The chains are immersed in various host media of refractive indices as mentioned in the legends. The fit (solid line) to the single-exponential decay $y = y_0 + a\exp(-x/b)$ where $b = 0.185 \pm 0.021,\ 0.206 \pm 0.019,\ 0.221 \pm 0.024$ in the media of refractive indices $n = 1,\ 1.33,\ 1.46$, respectively.

Figure 52a illustrates that the plasmon resonance wavelength red-shifts in a linear proportion with increasing refractive index of the ambient at any interparticle separation.

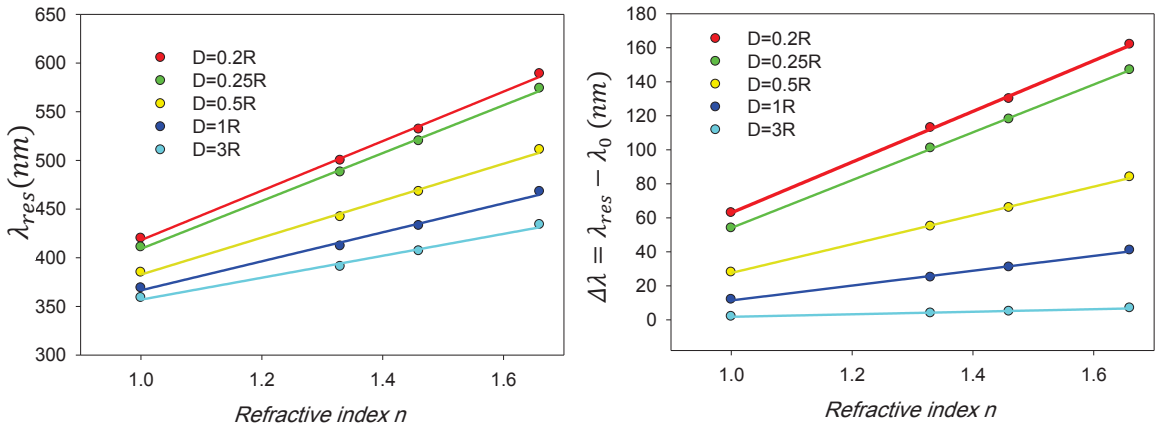

(a) (b)

Figure 52| (a) Resonance wavelengths of linear chains at different linear interparticle separations (listed in the legends) and (b) difference between the resonance wavelength of the chain and the resonance wavelength of the single component sphere as a function of the refractive index of the host medium.

The slopes of these linear proportions, plotted in Figure 52 b, increase inversely with interparticle separation. Therefore, the system exhibits larger magnitudes of plasmon red-shift at smaller interparticle distances in response to an increment in the medium refractive index. In other words, the sensitivity of the chain to the surrounding medium can thus be highly enhanced by decreasing interparticle separation as can be deduced from Figure 53. We found that the plasmon resonance red-shift decays exponentially with increasing D in units of component sphere diameter, with a decay length $b = 0.268 \pm 0.030$ calculated from the fit.

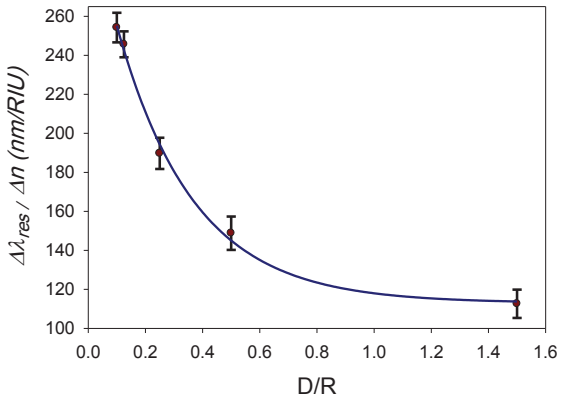

Figure 53| Plasmon resonance sensitivity of a linear chain to the surrounding medium as a function of the interparticle separation in units of component sphere diameter. The sensitivity decays near exponentially with $D/2R$ according to the solid line, fitted to the single-exponential decay $y = y_0 + a\exp(-x/b)$ where $b = 0.268 \pm 0.030$ and $a = 206.4$. The error bars represent the error in the straight line fits in Figure 52a.

P. K. Jain and M. A. El-Sayed [11] found theoretically that the sensitivity of 40nm diameter gold nanosphere pair decays near exponentially with increasing $D/2R$, with

decay constant $b = 0.18$. At $D/2R = 0.1$, this sensitivity is lesser by around 1.5 times than sensitivity of the silver chain, found in this work.

6.5 Under perpendicular polarization

The applied electric field is transversal to the chain axis, polarizes the particles in such a way that the induced local field is against the applied field but in the same direction of the Coulombic restoring force, which is hence enhanced. The plasmon frequency is shifted to a higher energy in this case.

The transverse plasmon resonance wavelength is blue-shifted as the interparticle spacing decreases. The effect of different host media on the plasmon absorption band is investigated at various interparticle distances and plotted in Figure 54. When the refractive index of the host medium is set to $n = 1$, the absorption efficiencies increase with interparticle separation in contrast with the case illuminated by a parallel polarization (see Figure 49a).

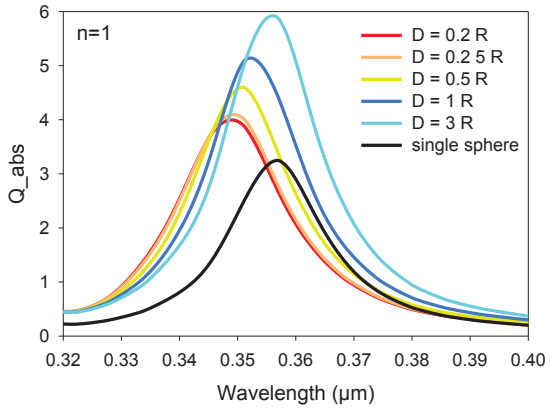

(a)

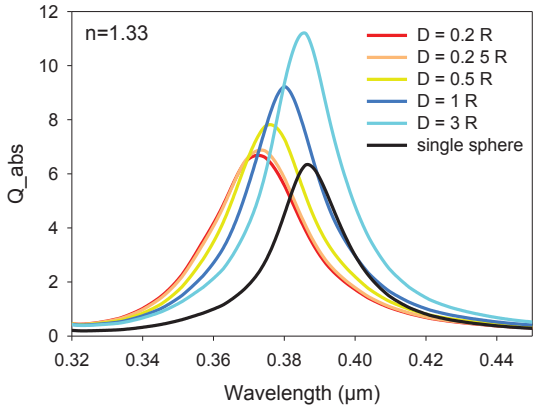

(b)

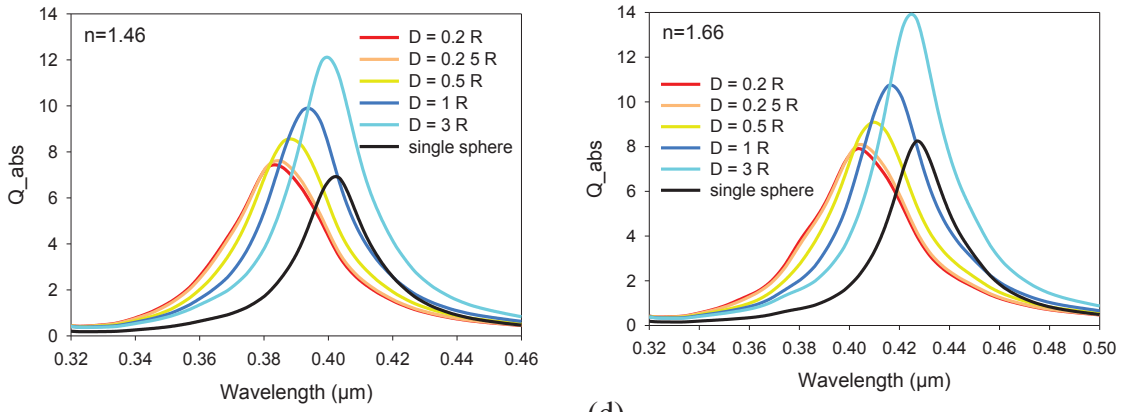

Figure 54| Absorption spectra of silver linear chains under perpendicular polarization, at different interparticle separations D (listed in the legends) and immersed in various embedding materials of refractive indices (a) $n=1$ (b) $n=1.33$ (c) $n=1.46$ (d) $n=1.66$. These diagrams show that the resonance wavelength is blue-shifted as the interparticle separation decreases.

6.5.1 Absorption cross-section

The absorption efficiencies are plotted in Figure 55 as a function of the refractive index of the host medium at various interparticle separations.

The absorption efficiency increases with interparticle separation in all host media, while it increases with refractive index of the host medium at a specific interparticle separation. The absorption coupling efficiencies are greater than those of the single spheres in all media, except hat in a medium of refractive index $n=1.66$ the coupling reduces the absorption efficiency when the interparticle spacing $D \le R/2$.

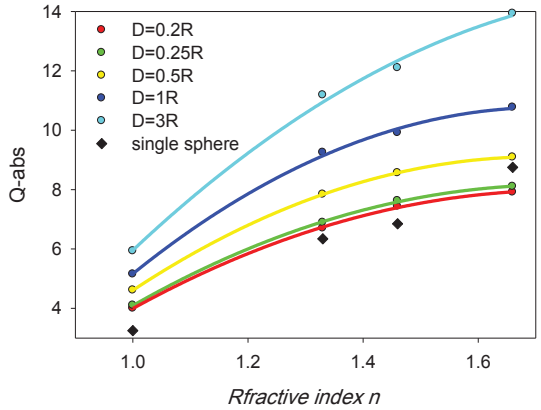

Figure 55| Absorption efficiencies of various chains at different interparticle separations D (listed in the legends) as a function of the refractive index of the host medium. Absorption efficiencies at all interparticle separations are proportional to the refractive index of the medium as seen from the fit (solid lines) to a polynomial-quadratic regression.

For smaller interparticle separations $D \leq R$, the absorption efficiency is plotted as a function of the interparticle separation in units of component sphere radius, as illustrated in Figure 56.

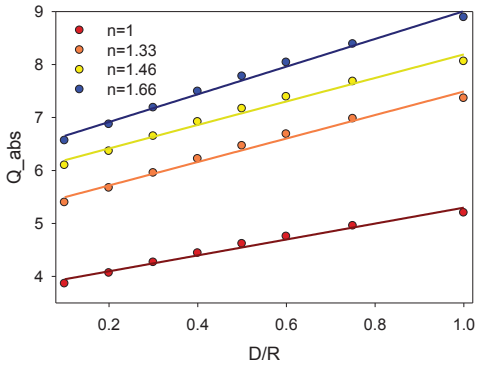

Figure 56| Absorption efficiencies of various chains embedded in different host media (refractive indices are listed in the legends) as a function of interparticle separations D in units of the component sphere radius. Absorption efficiencies in all host media are linearly proportional to the interparticle separation.

The absorption efficiencies increase slowly with D in linear proportions in all host media, the slopes of theses straight lines are being almost equal, especially when $n>1$. Consequently, the consecutive increments in the absorption with increasing interparticle separation can be roughly considered conserved in host media of $n>1$.

6.5.2 Plasmon resonance wavelength

At any interparticle separation, the plasmon coupling resonance wavelength of a chain red-shifts with increasing refractive index of the host medium according to a linear proportion as illustrated in Figure 57.

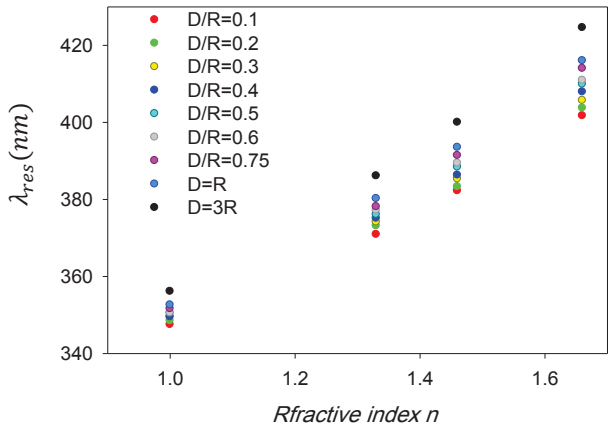

Figure 57| Transverse resonance wavelengths of a linear chain at different interparticle separations (listed in the legends) as a function of the refractive index of the host medium.

The slopes of these linear proportions, plotted in Figure 58 b, increase with interparticle separation in contrast with what we found for incident polarization parallel to the chain axis (see Figure 52 b).Consequently, a silver chin exhibits larger magnitudes of plasmon red-shift at the larger interparticle separation, considered in this case, in response to an increment in the refractive index of the host medium.

The advantage of such a configuration is the narrow bandwidth of dipole plasmon resonance, relatively to the parallel polarization case, at smaller interparticle distances as can be seen from Figure 48 and Figure 54.

In order to extract the sensitivity of a silver chain ($\Delta\lambda_{res}/\Delta n$) as a function of the interparticle separation, the magnitudes of plasmon red-shifts were plotted in Figure 58a, according to $\Delta\lambda = \lambda_{res} - \lambda_0$ where λ_0 defines the resonance wavelength of the chain when each sphere is touched by its two neighbouring particles. This definition of λ_0 is more convenient since the near-field plasmon coupling resonance, under perpendicular polarization, occurs at wavelengths shorter than those of single particles as shown in Figure 54.

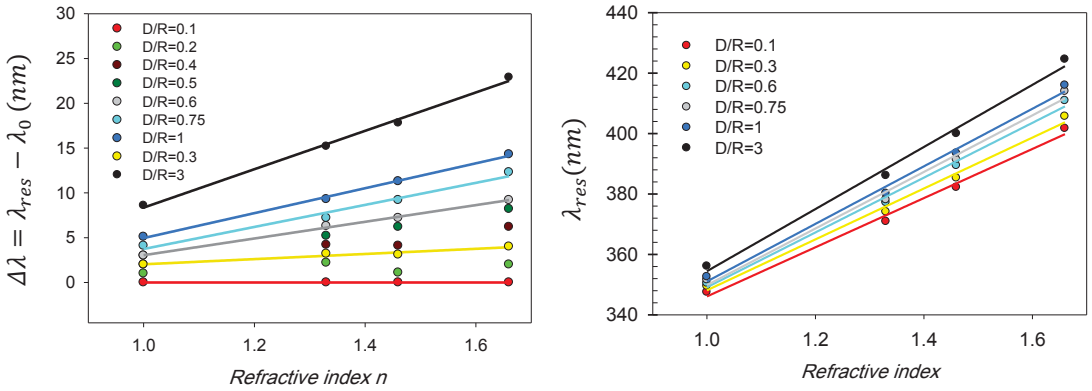

Figure 58| (a) Difference between the resonance wavelength of chains of various interparticle separations (listed in the legends) and λ_0 (the resonance wavelength of the chain when each sphere is touched by its two neighbouring spheres) and (b) resonance wavelengths of linear chains as functions of the refractive index of the host medium.

In Figure 58b we consider chains of interparticle separations showing the most linear proportion of plasmon red-shifts as functions of the environment refractive index that can be easily detected in Figure 58a.

On contrary to the chain plasmon sensitivity under parallel polarization, we found that the sensitivity decay with decreasing interparticle separation, the solid line in Figure 59 is the fit to the single-exponential decay with three parameters given as $y = y_0 + ae^{-\frac{x}{b}}$ where $b = 0.438 \pm 0.058$ is the decay length and $a = -25.73 \pm 1.14$.

The plasmon resonance sensitivity is enhanced up to 20.4nm at the interparticle separation $D = 2R$.

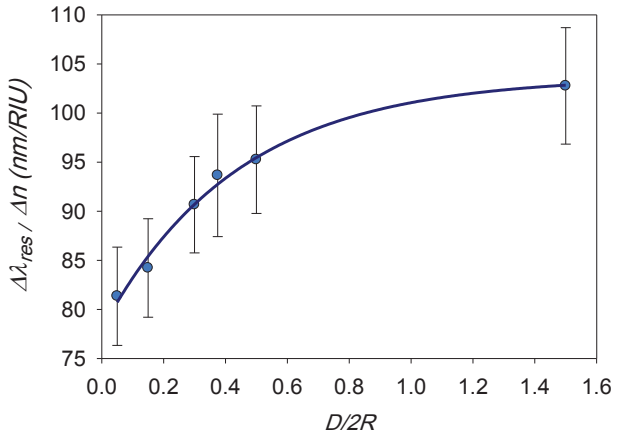

Figure 59| Plasmon resonance sensitivity of a linear chain to the surrounding medium as a function of the interparticle separation in units of component sphere diameter. The sensitivity decays exponentially with decreasing $D/2R$ as seen from the fit (solid line) to the single-exponential decay $y = y_0 + a\exp(-x/b)$ where $b = 0.438 \pm 0.058$ and $a = -25.73 \pm 1.14$.The error bars represent the error in the straight line fits in Figure 58b.

It has also been found that the fractional plasmon shift ($\frac{\Delta\lambda}{\lambda_0}$) of a silver chain, embedded in a medium of refractive index n=1.66, decays exponentially with increasing $D/2R$.

Note that the negative sign of the ordinate indicates the plasmon coupling blue-shift relatively to λ_0 (the resonance wavelength of a single component sphere)

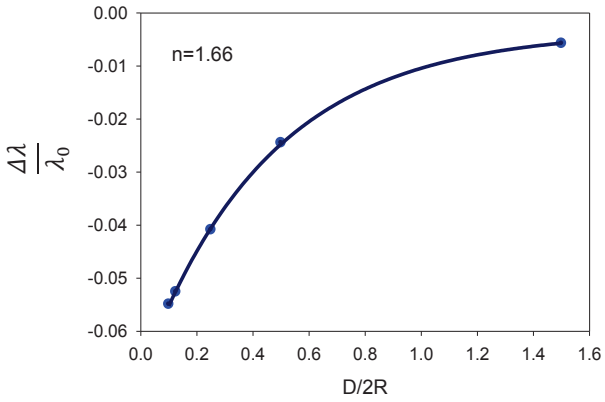

Figure 60| Fractional plasmon shift as a function of the interparticle separation in a linear chain in units of component sphere diameter, when the chain is immersed in the host medium of refractive index $n = 1.66$. The solid curve is a regression of single-exponential decay function $y = y_0 + a\exp(-x/b)$ where $b = 0.451 \pm 0.013$ and $a = -0.065$.

The different behaviours, observed in Figure 59 and Figure 60, reflect an evident dependency of the plasmon resonance shift on the host medium for incident polarization perpendicular to the chain axis. The sensitivity of the longitudinal plasmon coupling is stronger than that of the transverse. The sensitivity of the longitudinal/transverse resonance wavelength exponentially decays with increasing/decreasing interparticle separation.

6.6 Under oblique polarization

Both the longitudinal and transverse plasmon coupling bands can be recognized under oblique polarization. The absorption spectra of silver chains in 4 different host media at various interparticle separations under oblique polarization $\varphi = 45^o$ are plotted in Figure 61.

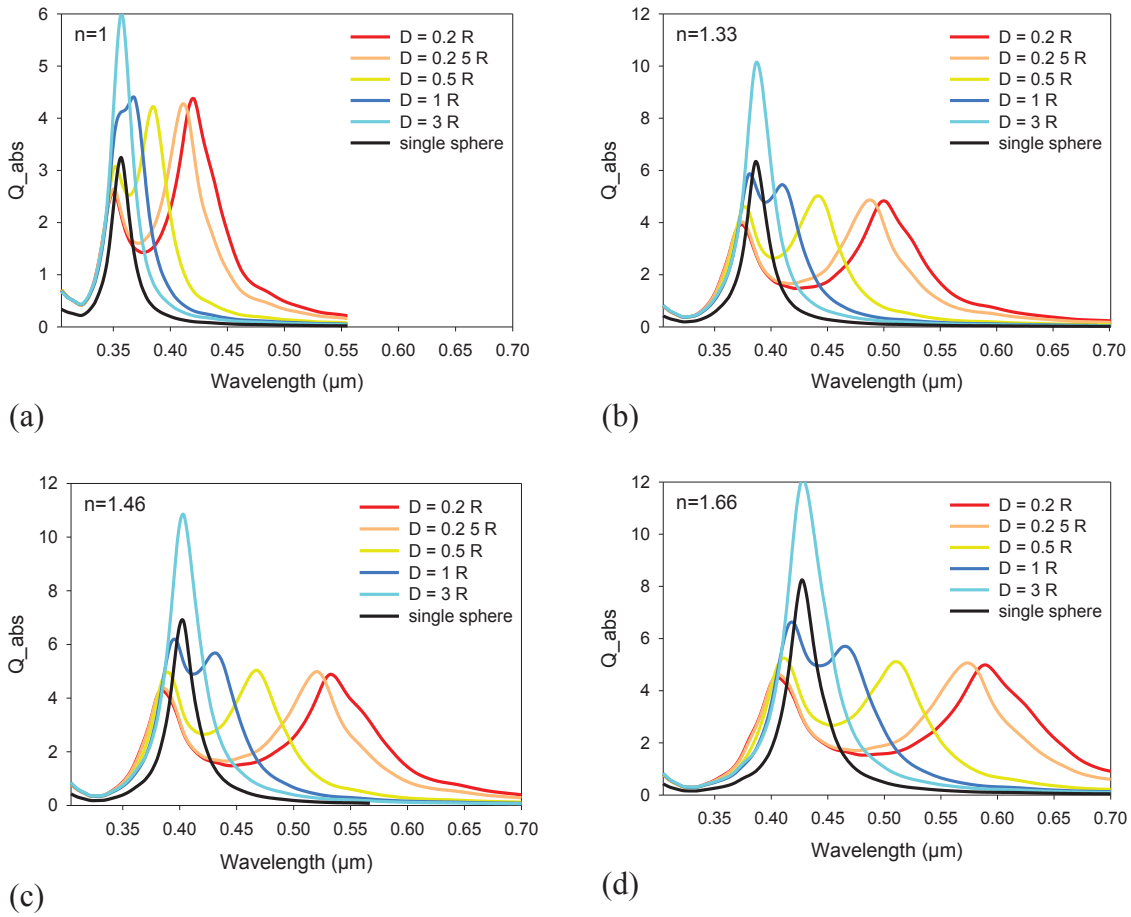

Figure 61| Absorption spectra of linear chains under oblique polarization $\varphi = 45^o$ at different interparticle separations D (listed in the legends) and immersed in various embedding materials of refractive indices (a) $n = 1$ (b) $n = 1.33$ (c) $n = 1.46$ and (d) $n = 1.66$.

It has been found that at the interparticle separation $D = 3R$, only one strong plasmon coupling absorption band can be observed. Decreasing the interparticle distance, the single plasmon resonance band is split into two plasmon bands forming two different peaks. They evolve with decreasing interparticle separation into two well-defined and well-separated plasmon bands. The longitudinal and transverse plasmon bands locate at the lower and the higher energies, respectively. The separation between the peak positions of those bands is strongly affected by the dielectric host medium, and essentially attributed to the longitudinal plasmon shift (compare the plasmon sensitivities plotted in Figure 53 and Figure 59) which is much larger at smaller interparticle separations, in contrast with the case of perpendicular polarization.

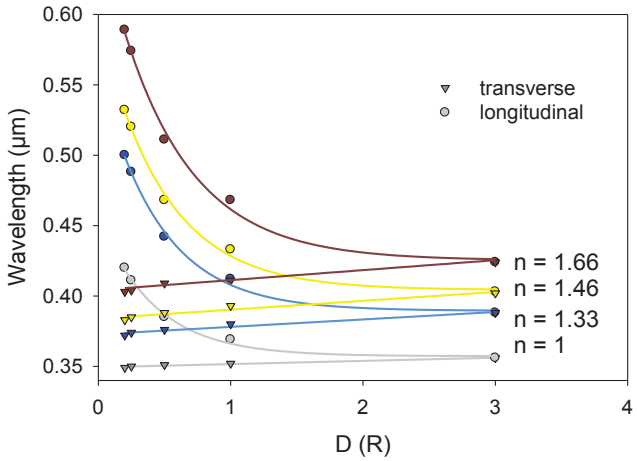

Figure 62| Longitudinal and transverse plasmon resonance wavelengths of linear chains in various surrounding media as a function of the interparticle separation in units of component sphere radius, under oblique polarization $\varphi = 45^o$. Increasing interparticle separation, both longitudinal and transverse peaks move towards each other to overlap when D approaches $3R$.

As the refractive index of the host medium increases and the interparticle separation decreases, the longitudinal plasmon band is broadened and red-shifted to a lower energy, while the transverse plasmon band is blue-shifted (Figure 62). Consequently, they get more separated and better defined.

At $D \approx 3R$, a single well-defined dipole plasmon resonance band was observed under parallel, perpendicular or oblique polarization in all media. The absorption efficiency is being slightly larger in the case of the perpendicular polarization. The plasmon bandwidths in case of the oblique and parallel polarizations were found to be equal $FWHM = 42, 29, 22nm$ in $n = 1.66, 1.33, 1$, respectively, while under perpendicular polarization $FWHM = 33, 24, 20nm$ in $n = 1.66, 1.33, 1$. These variations in the bandwidth values vanish in the far-field plasmon region under any orientation of the linear polarization of the incident light (see 6.7.3).

6.7 The effect of the dielectric environment on far-field interactions and plasmon coupling

6.7.1 Under parallel polarization

Increasing the interparticle separation in the chain, the plasmon resonance wavelength is progressively shifted toward the resonance wavelength of a single component particle, at which the far-field plasmon resonance coupling takes place. A comparison between the absorption efficiencies of a silver chain in different host media has been done. We found that the absorption efficiency decreases with separation in the near-field region see Figure 48a. Once the interparticle separation in the chain exceeds $D = 6R$, the absorption

efficiency increases slightly with separation until it reaches a maximum around 6.5 (less than that resulted from the near-field coupling) when $D = 44R$ where the refractive index of the surrounding medium is set to unity. Afterwards the inverse proportion with interparticle separation returns as D increases up to $66R$ as illustrated in Figure 63b.

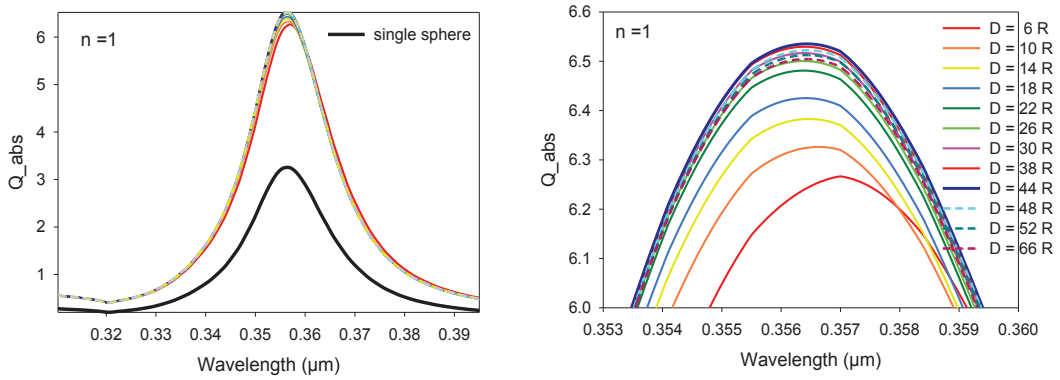

Figure 63| Absorption spectra of a silver linear chain under parallel polarization, at different interparticle separation D extending to far-field region (listed in the legends). The refractive index of the surrounding medium is set to unity.

Increasing refractive index of the host medium to $n = 1.66$, the absorption efficiency increases with interparticle separation in near-field region, as shown in Figure 48d. The main different aspect in behavior of the far-field absorption efficiency, with respect to that observed when $n = 1$, is the enhancement of the absorption efficiency up to 1.68 larger than that attributed to the near-field coupling, and also greater than that observed in $n = 1$ at far-field range by 2.6 times. Besides, the maximum efficiency is reached at a smaller particle separation $D = 30R$, as it can be seen in Figure 64.

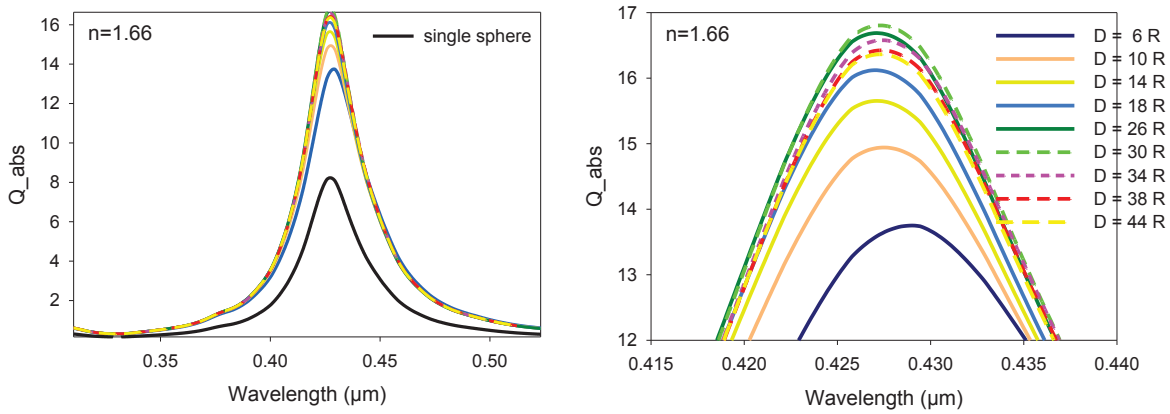

Figure 64| Absorption spectra of a silver linear chain under parallel polarization at different interparticle separation D extending to far-field region (listed in the legends). The refractive index of the surrounding medium is set to $n = 1.66$.

An increase in the medium refractive index magnifies the scattering process in each component particle, which contributes effectively in the far-field coupling. Eventually, the absorption efficiency is enhanced in the far-field region.

6.7.2 Under perpendicular polarization

Increasing interparticle separation, the plasmon resonance red-shifts with interparticle separation in near-field region. Once $D > 3R$ the plasmon resonance reaches the resonance wavelength of a single component particle, and slightly fluctuates afterwards around a few nanometers with non-monotonic shift [62,63].

When the refractive index of the host medium $n = 1$, the absorption efficiency increases with the separation in the near-field region (Figure 54). Once the interparticle separation is greater than $D = 10R$, the absorption efficiency increases slightly until it reaches a maximum around 6.6 when the interparticle separation is roughly $D = 38R$ (a lesser

distance D than that required in the case of parallel polarization). This separation represents the optimum interparticle spacing for far-field coupling, which is mainly supported by the radiative scattering of the nearest particle composing the system. Any increase in the interparticle separation afterwards drifts the absorption slightly to a lower efficiency, as illustrated in Figure 65, as D increases up to $48R$.

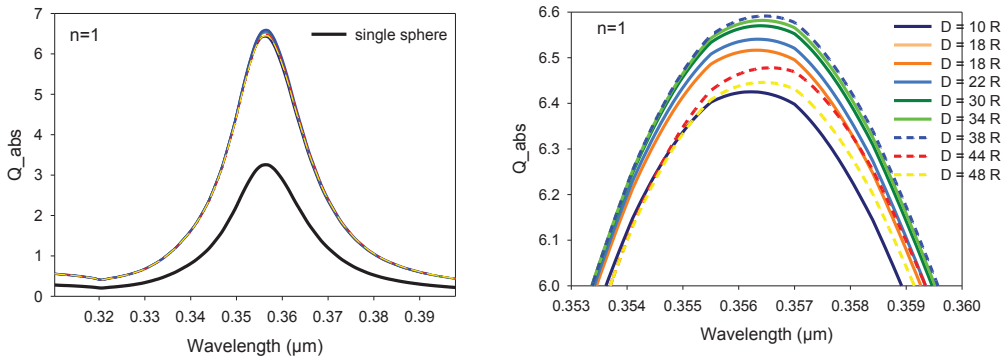

Figure 65| Absorption spectra of linear chains under parallel polarization, at different interparticle separation D extending to far-field region (listed in the legends), the refractive index of the surrounding medium is set to unity.

Increasing refractive index of the medium to $n=1.66$, the absorption efficiency is enhanced up to 17.4, as shown in Figure 66, which is greater than that observed in $n=1$ at far-field region by 2.6 times. Figure 66 shows that a maximum efficiency is reached at a smaller particle separation $D=26R$ in comparison to $D=38R$ that is required in $n=1$ (see Figure 65), and also with respect to that found under the parallel polarization case $D=30R$ in the same medium (see Figure 64).

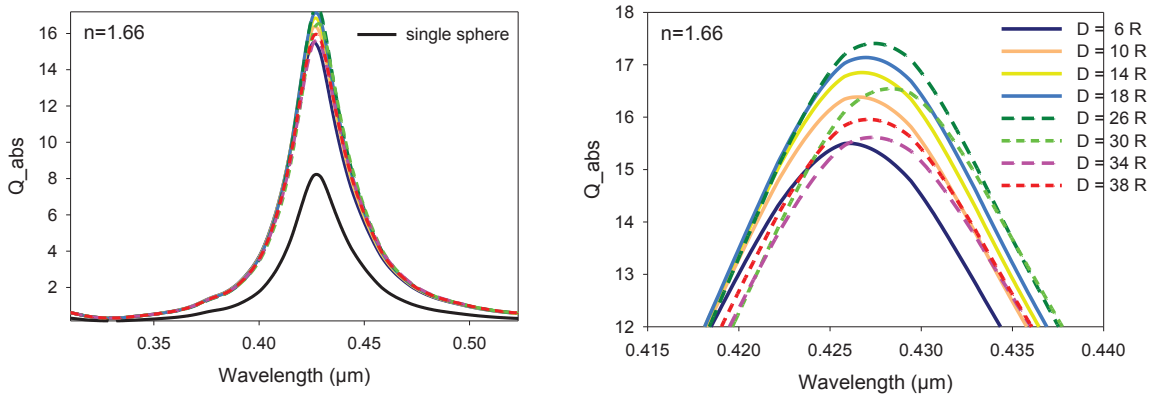

Figure 66| Absorption spectra of linear chains under perpendicular polarization at different interparticle separation D extending to far-field region (listed in the legends). The refractive index of the surrounding medium is set to $n = 1.66$. After reaching the plasmon resonance wavelength of a single component particle, it slightly fluctuates with non-monotonic shift.

6.7.3 Dipole plasmon coupling bandwidth

For any incident polarization, the plasmon absorption band with a maximum efficiency retains the similar bandwidth to that of a single component sphere in the same medium, which is 20nm or 30nm in the host media $n = 1, 1.66$, respectively.

In summary, the far-field plasmon absorption efficiency is highly enhanced with a narrow band in contrast with the broadened plasmon bands that are produced in the near-field coupling region.

CHAPTER 7

Component particle size effect on the dipole plasmon coupling resonance in silver linear chains

Introduction

We now would like to know whether the plasmon shift $\Delta\lambda$ at any given interparticle separation is independent of the component spheres diameter. If not, how does it change with the sphere diameter? Does it have a similar response in the longitudinal and the transverse dipole plasmon resonances?

7.1 The DDA target

A linear chain composed of equally spaced eight identical spherical silver particles is simulated and schematically depicted in Figure 46. The radius R of the component spheres ranges between 2nm and 15nm, at various interparticle separations ranging between $D = R/8$ and $D = 2R$, under the two kinds of polarization; parallel and perpendicular to the chain axis as defined by the polarization angles $\varphi = 0^o$ and $\varphi = 90^o$, respectively. The refractive index of the embedding environment is set to that of PDMS $n = 1.46$.

The optical properties of silver chains are investigated via the absorption spectra that were calculated and plotted in Figure 67 and Figure 73.

7.2 Under parallel polarization

The absorption spectra calculated for different component particle radii are plotted in Figure 67.

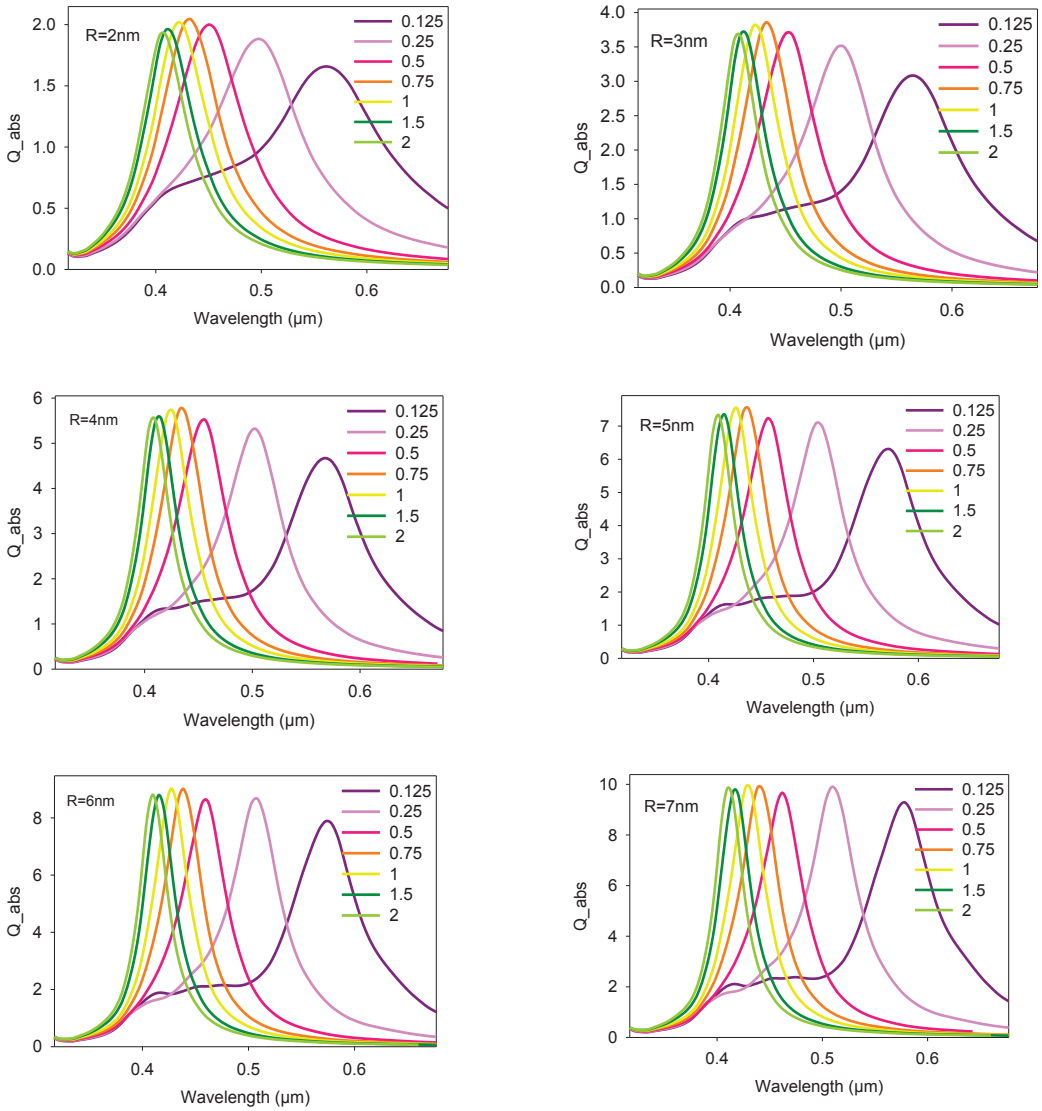

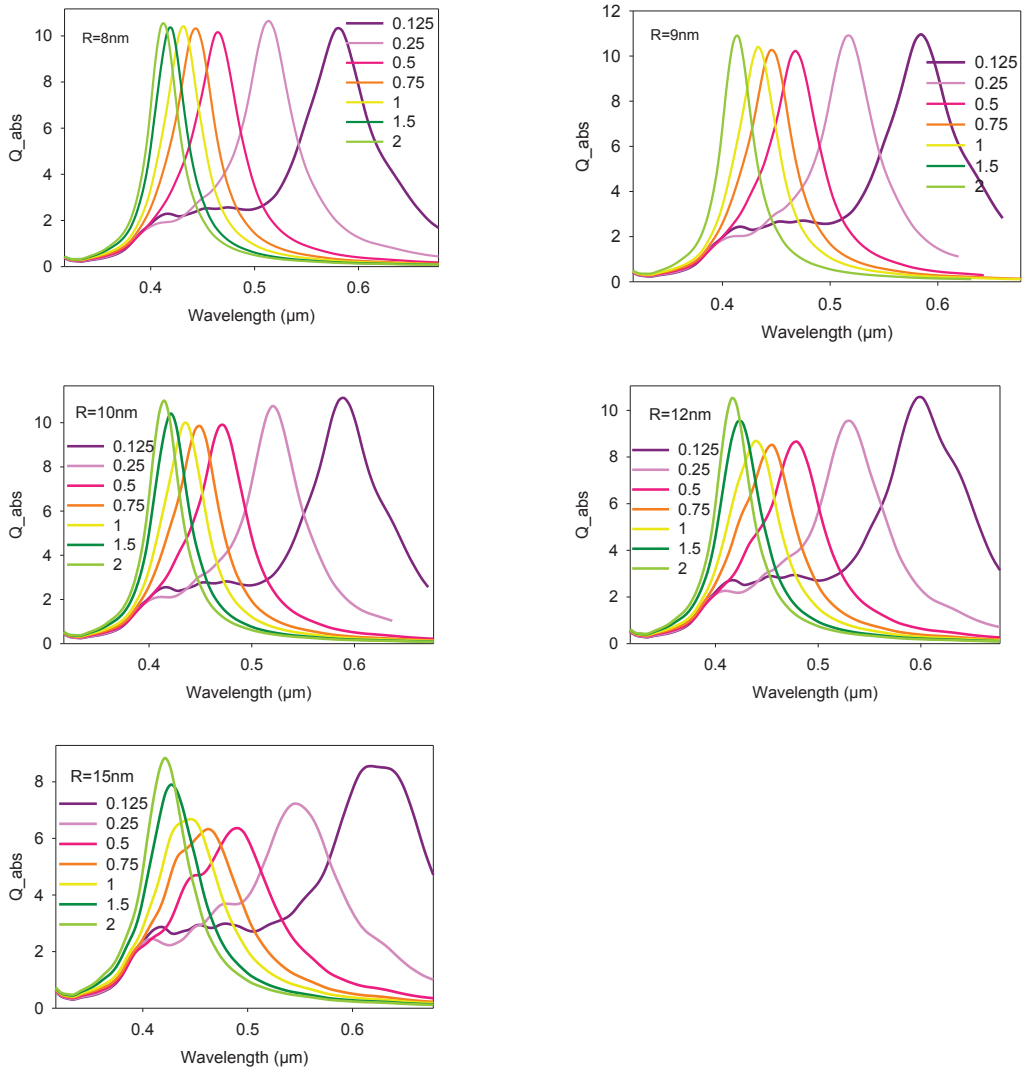

Figure 67| Absorption spectra linear chain under parallel polarization as a function of the wavelength at different interparticle separations D (listed in the legends) and immersed in embedding material of refractive index $n = 1.46$. The component sphere radius is mentioned in each diagram.

The profile lines of the absorption spectra are smooth and streamlined as long as the electric field is uniform across the small silver particles. By increasing the particle size and decreasing the interparticle separation, the phase retardation, usually experienced by large particles, can be stimulated yielding the quadrupole plasmon shoulders, observed in

the spectra of chains composed of 12nm and 15nm spheres at smaller separations $D = 3R/4$ or less. Eventually, increasing component particles size, the plasmon coupling absorption bands get deformed and deviated from the Gaussian bell shape. Those spectra were thus not used in studying the dipole plasmon resonance bandwidth.

7.2.1 Plasmon resonance wavelength

The resonance wavelengths of the plasmon coupling in chains red-shift according to a linear proportion with the component particle size, at any interparticle separation D. The rate of resonance wavelength red-shift is represented by the slopes of these straight lines, illustrated in Figure 68. This rate decreases with interparticle spacing D.

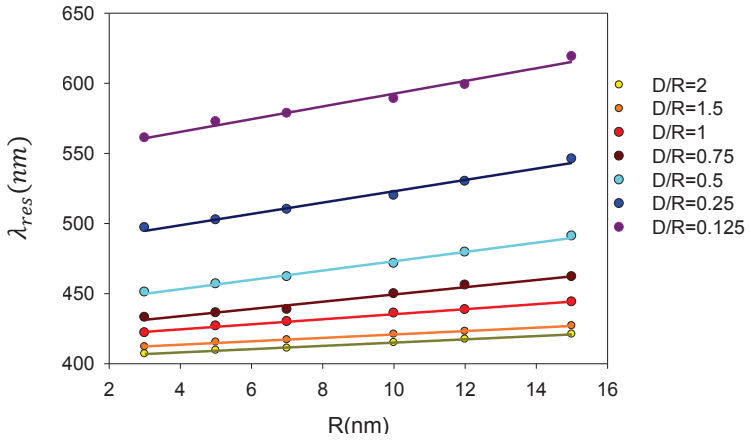

Figure 68| Resonance wavelengths of linear chains at different linear interparticle separations (listed in the legend) as a function of the component sphere radius. The resonance wavelength, at a specific D, red-shifts according to a linear proportion with the component sphere radius.

In order to deduce the sensitivity of the resonance wavelength to the component particles size, the ratio $\frac{\Delta\lambda_{res}}{\Delta R}$ has been investigated at various separations, and found to be exponentially decayed with interparticle spacing scaled by the sphere diameter as represented in Figure 69.

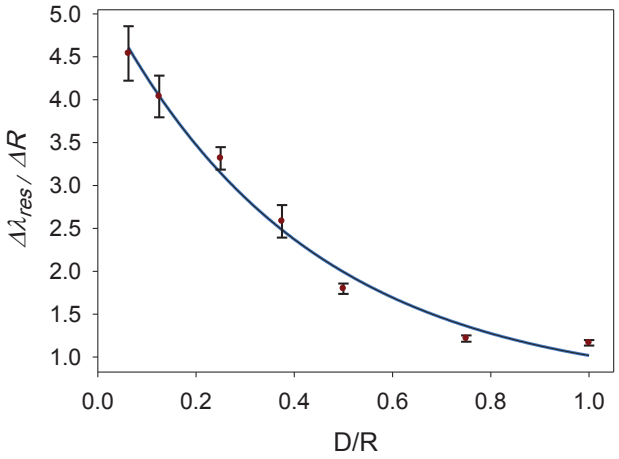

Figure 69| Plasmon resonance sensitivity of a chain to the component sphere size as a function of the interparticle separation in units of component sphere diameter. The sensitivity decays exponentially with $D/2R$ as seen from the fit (solid line) to the single-exponential decay $y = y_0 + a\exp(-x/b)$ where $b = 0.413 \pm 0.082$ and $a = 4.657 \pm 0.282$. The error bars represent the error in the straight line fits in Figure 68.

In summary, the plasmon resonance red-shift is slightly dependent on the particle size at larger separations $D \geq 1.5R$. Decreasing the interparticle spacing D, the sensitivity increases up to 4.54nm per nm change in the sphere radius. Depending on the separation, this portion changes exponentially. Thus, the plasmon resonance wavelength depends on the component sphere size, especially at smaller interparticle separations $D \leq 0.4R$. This result is in contradiction with the universality of the plasmon ruler law derived by Jain et

al. [10], whereas it agrees with Encina et al.'s work [64] illustrating that in a system, composed of silver nanosphere pairs, the fractional plasmon shift and the decay constant depend on the size of the nanoparticle pair.

7.2.2 Bandwidth

Decreasing the interparticle separation in a chain, the plasmon bandwidth gets broadened, due to the overlap of the enhanced local electric fields between coupled neighbouring particles [60].

The dipole plasmon coupling bandwidths, extracted from the absorption spectra illustrated in Figure 67, are plotted in Figure 70 as a function of the component spheres size.

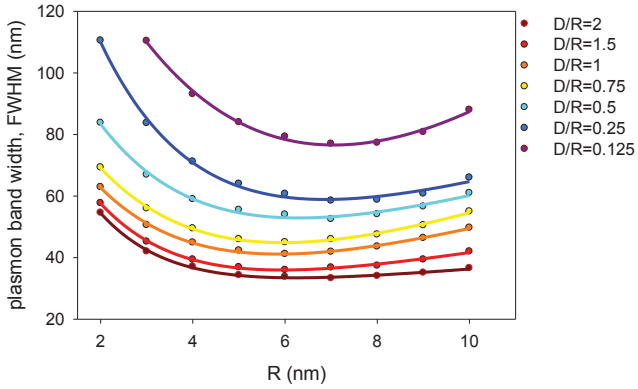

Figure 70| Plasmon bandwidth of the longitudinal plasmon resonance as a function of the component sphere radius, at various interparticle separations (listed in the legend), solid lines are fitted to the exponential linear combination with four parameters.

The lines were fitted according to the exponential linear combination function with 4 parameters $y = y_0 + ae^{-\frac{x}{b}} + cx$.

7.2.3 Bandwidth for smaller component spheres

When the component sphere is restricted to the radius of 7nm or less, the dipole plasmon bandwidth as a function of the particles radius is plotted in Figure 71. The solid lines are fitted to the single exponential decay.

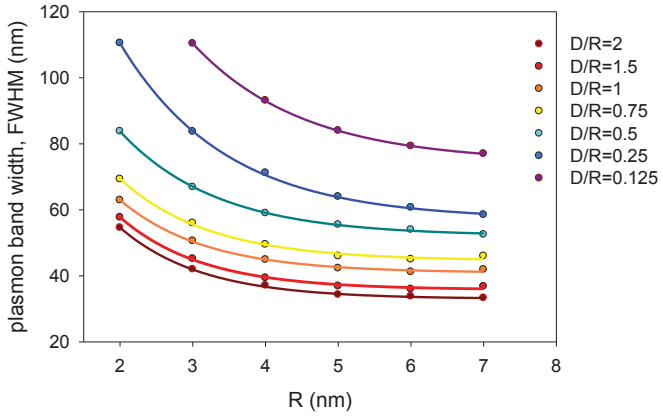

Figure 71| Plasmon bandwidth of the longitudinal dipole plasmon resonance as a function of the component spheres radius at various interparticle separations (listed in the legend).the (solid lines) are fitted to the single-exponential decay with three parameters. The point represents 2nm radius at $D = 2R$ is omitted since the absorption plasmon band was deformed and deviated from the Gaussian bell shape as shown in Figure 67.

According to this size range, the plasmon bandwidth at a specific separation exponentially decays with particle size as can be deduced from the Figure 71.

The lines, plotted in Figure 71, fit the single-exponential decay function $y = y_0 + a\exp(-x/b)$ where y_0, a, b are plotted in Figure 72 as a function of the separation in units of sphere radius.

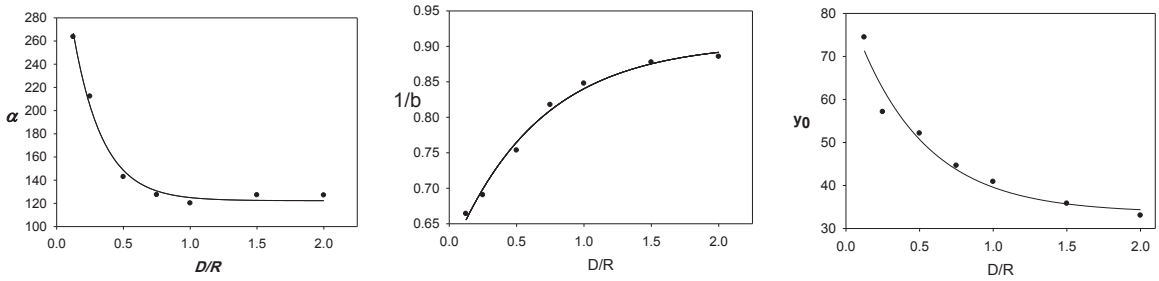

Figure 72| Three parameters of the single-exponential decay function to which the dipole plasmon coupling bandwidths are fitted as a function of the component sphere radius.

7.3 Under perpendicular polarization

The transverse dipole plasmon coupling resonance is excited. The resonance wavelength is blue-shifted to a higher energy with decreasing interparticle spacing. The absorption spectra calculated for different component particle radii are plotted in Figure 73.

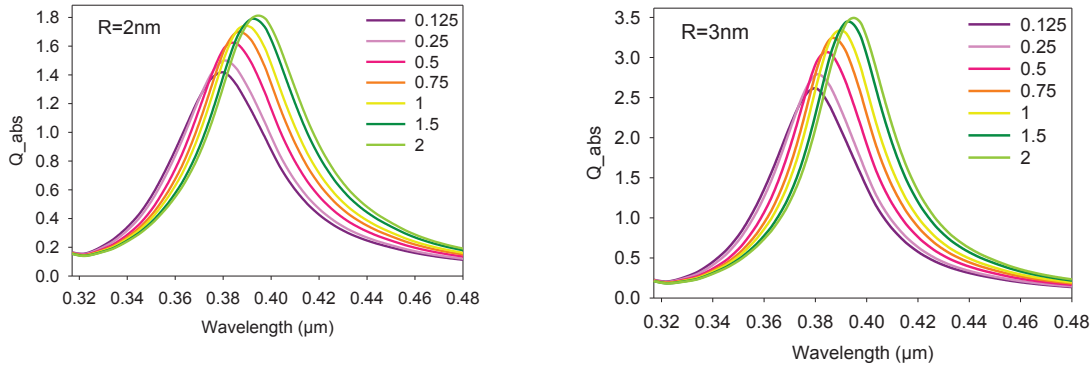

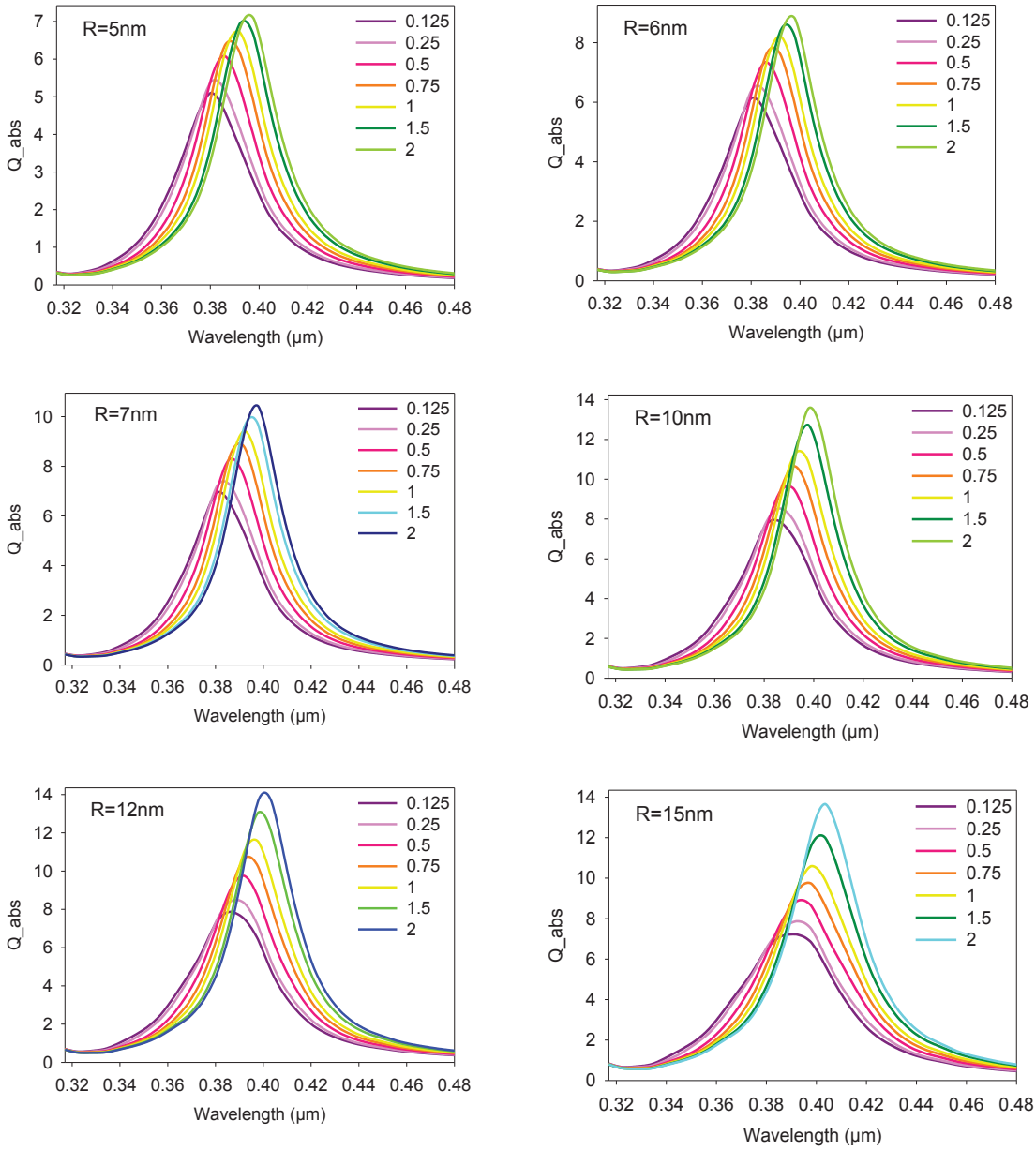

Figure 73| Absorption spectra of a silver linear chain under perpendicular polarization as a function of the wavelength at different interparticle separations D (listed in the legends) and immersed in embedding material of refractive index $n = 1.46$. The component sphere radius is mentioned in each diagram.

The phase retardation is not observed through the spectra. It is worth mentioning that at any interparticle separation, the absorption efficiency gradually increases as the

component sphere radius increases until it reaches a maximum at radius 12nm. Afterwards the efficiencies fluctuate around similar values since the absorption process is reduced in favor of the scattering in the larger particles as can be seen in Figure 74.

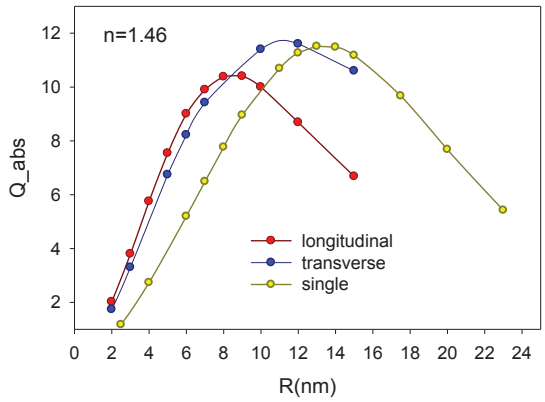

Figure 74| Absorption efficiency of the dipole plasmon resonance as a function of the particle size of: i) a single silver component sphere (yellow) ii) a linear silver chain at the interparticle separation $D = R$, under parallel polarization (red) iii) the chain under perpendicular polarization (blue), in PDMS.

The coupling energy reduces the optimum size corresponding to the maximum absorption. The optimum size of an isolated sphere 13nm is reduced in the chain under perpendicular polarization to 12nm and to 8nm under parallel polarization.

7.3.1 Plasmon resonance wavelength

It has already found that for a specific particle size the plasmon coupling resonance wavelength blue-shifts with decreasing interparticle separation. At any interparticle separation D, the resonance wavelength red-shifts with the component particle size, as shown in Figure 75.

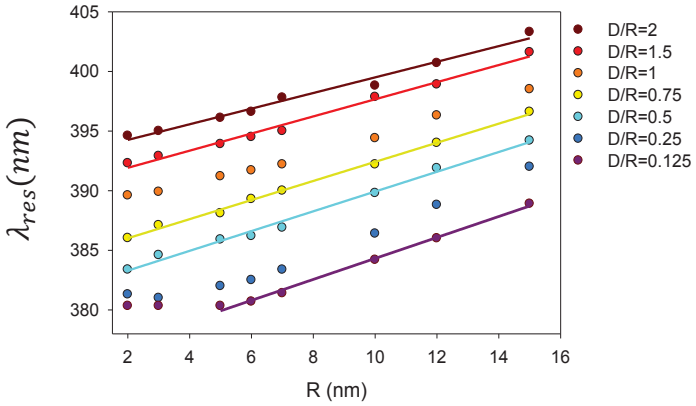

Figure 75| Resonance wavelengths of linear chains at different interparticle separations (listed in the legend) as a function of the component sphere radius. The resonance wavelength, at a specific D, red-shifts according to a linear proportion with the component sphere radius.

The rate of resonance wavelength red-shift is determined by the slope of a straight line, and is found to be slightly reduced with increasing interparticle spacing D. The sensitivity of the resonance wavelength to the component particles size ($\frac{\Delta\lambda_{res}}{\Delta R}$) as a function of the interparticle separation scaled by the particle size is represented in Figure 76.

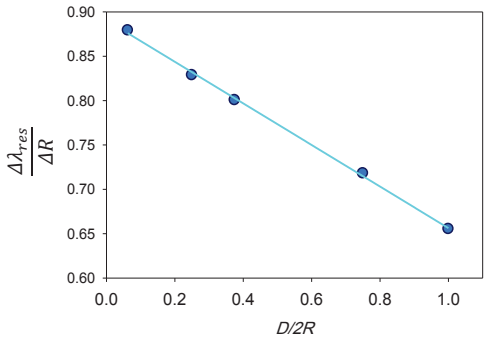

Figure 76| Plasmon resonance sensitivity of a linear chain to the component sphere size as a function of the interparticle separation in units of component sphere diameter.

The plasmon wavelength sensitivity linearly decreases with increasing interparticle separation. Thus, the sensitivity ranges between 0.88nm and 0.65nm per nm change in the spheres radius depending on the separation.

7.3.2 Bandwidth

The dipole plasmon coupling bandwidths, extracted from the absorption spectra of linear chains at various interparticle separations, are depicted in Figure 77 as a function of the component sphere radius. The plasmon bandwidth, over all interparticle separations, decreases with increasing particle size until it reaches a minimum value when $R \approx 7nm$. Afterwards, the bandwidth gradually increases with the particle size according to a rate that is reciprocally proportional to the interparticle separation.

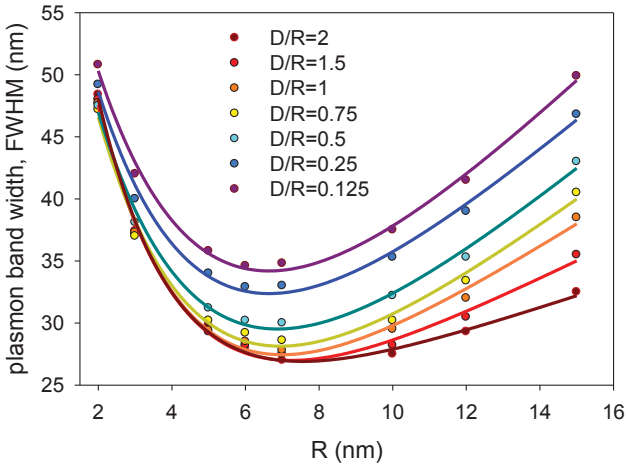

Figure 77| Plasmon bandwidth of the transversel dipole plasmon resonance as a function of the component spheres radius at various interparticle separations (listed in the legend). Solid lines are fitted to the exponential linear combination with four parameters $y = y_0 + a\exp(-\frac{x}{b}) + cx$.

CHAPTER 8

Particles configuration effect on the dipole plasmon coupling resonance in interacting silver nanoparticles

Introduction

Optical responses of various nanoparticle configurations have been studied as follows:

- A planar system composed of linear combinations consisting of well-separated linear chains, placed in arbitrary directions. This system can be modelled by a two-dimensional array, aligned on a square circumference where each particle has two direct neighbouring particles.
- A two-dimensional system composed of 36 identical spheres uniformly arranged in a square area. Each particle is surrounded by four direct neighbouring particles.
- Multilayer targets set up of identical silver ultrafine nanospheres, which are hexagonally close-packed in three-dimensional configurations, and each particle is surrounded by twelve direct neighbouring particles.

8.1 One- dimensional and two-dimensional arrays of spherical silver nanoparticles

A two-dimensional system of silver spheres ($R < 10nm$) that are aligned in a close proximity $D \le R$ only in arbitrary linear directions with a very low percentage of surface coverage. This system can be considered as a combination of well-separated linear chains

distributed randomly on a surface. For incident polarization parallel to the surface, the random orientation of the linear chains relative to the electric field gives equal chance to both parallel and perpendicular electric field components to be received by all of the linear chains composing the system. Therefore, the system can be modelled by the circumference of a square, illuminated by a plane wave light with polarization parallel to the square surface. This is done in order to investigate the near-field interactions and the dipole plasmon coupling resonance yielding the optical properties of such a system.

8.1.1 The DDA target geometry and orientation

20 spheres of radius 8nm, suspended in a host medium of refractive index $n = 1.66$, are aligned according to the circumference with an interparticle separation D, which varies between $\frac{R}{4}$ and $3R$, as illustrated in Figure 78a. The incident electric field oscillates parallelly to the y axis. At any value of φ, the oscillating electric field applied to the chains is divided into two components, parallel and perpendicular to each chain axis.

Rotating the target in the y-z plane, the loss of an electric field component received by a pair of parallel sides will in turns be gained by the other pair, due to the geometrical symmetry of the square. As the optical properties investigated are mainly attributed to the interaction between the electric field and the metallic particles, a random in-plane rotation would not affect the optical response of such a system. This is confirmed by our calculations. The optical response of two-dimensional arrays illustrated in Figure 78b has been already shown to be invariant with respect to any φ [65].

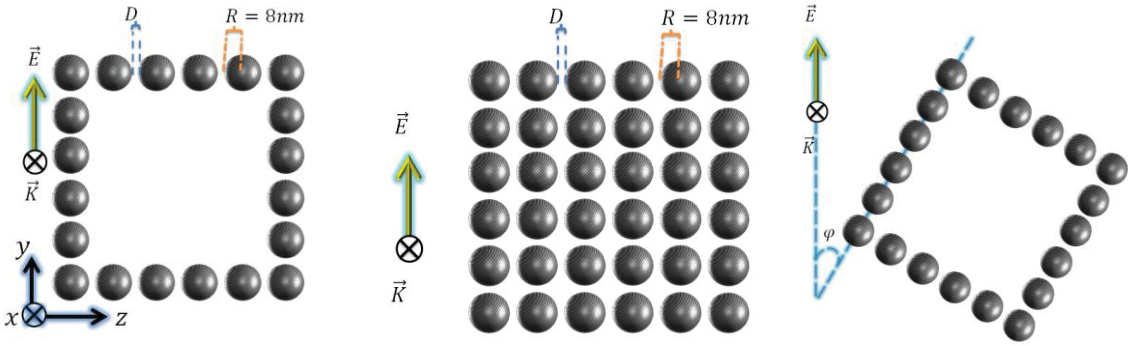

Figure 78| Schematic representation of (a) linear silver chains placed on the a square circumference (b) a planar array of equally separated identical silver nanospheres, (c) the x-y plane is the plane of incidence, the incident electric field is parallel to the y axis. φ is the polarization angle between the electric field and the axis of any reference linear chain.

8.1.2 The effect of the particle configuration on the dipole plasmon coupling

The absorption spectra of the system, depicted in Figure 78a, reveal two well-separated plasmon coupling bands. When $D < R$, the longitudinal plasmon band, attributed to the electric field components parallel to the chains axes, is observed at the lower energy, while the transverse plasmon band, excited by the other perpendicular field components as illustrated in Figure 79a. The difference between those energies as a function of the interparticle separation depends mainly on the longitudinal plasmon energy, as it strongly relies on the interparticle separation (see Figure 50 and Figure 60). By increasing the interparticle separation, both of the plasmon peaks move towards each other until they get incorporated into single plasmon band as demonstrated when $D = 3R$ in Figure 61 d.

Another two-dimensional system, depicted in Figure 78b, is studied. In such an array configuration, both of the electric field components face the same particles distribution.

The aforementioned transverse plasmon mode therefor vanishes as can be seen in Figure 79b. On the other hand, the nearest neighbouring particles to each inner particle are doubled in comparison to the previous system, the near-field interactions between the particles located at direct vicinity are thus improved, which leads to a broadened dipole plasmon resonance band centered at longitudinal resonance wavelength, as illustrated in Figure 79b.

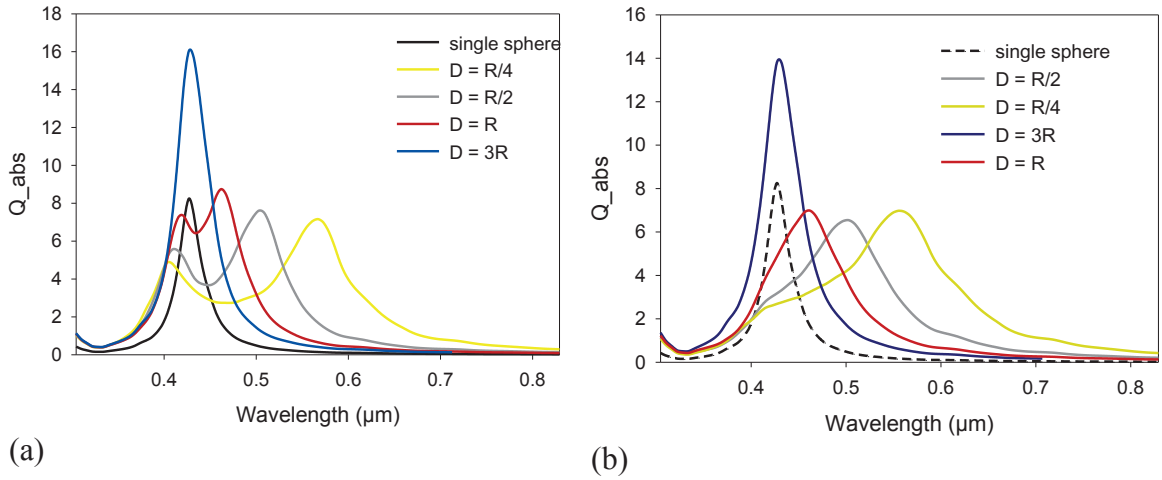

(a) (b)

Figure 79| Absorption spectra of silver nanospheres uniformly placed on: (a) a square circumference (b) a square area, at various interparticle separations (listed in the legends).

In summary, the configuration of the nanoparticles has a crucial effect on the near-field plasmon coupling resonance. The longitudinal and transverse plasmon bands, excited in a linear chain at parallel and perpendicular polarization respectively, were simultaneously observed in a two-dimensional system of well-separated linear chains aligned with arbitrary directions, under p-polarized light. Whereas, a single broadened band is observed in an planar array of spheres distributed in close proximity to each other.

8.2 Two-dimensional planar arrays of spherical silver nanoparticles

The DDA target consists of 36 equal-sized spheres, which are equally spaced in a planar array under p-polarized light as sketched in Figure 78b. But the component particle size ranges between $4nm$ and $28nm$.

8.2.1 Absorption cross-section

The effect of the coupling energy on the contribution of the absorption process to the extinction can be investigated by tracing the optimum size, which corresponds to the highest absorption efficiency of two-dimensional nanoparticles array.

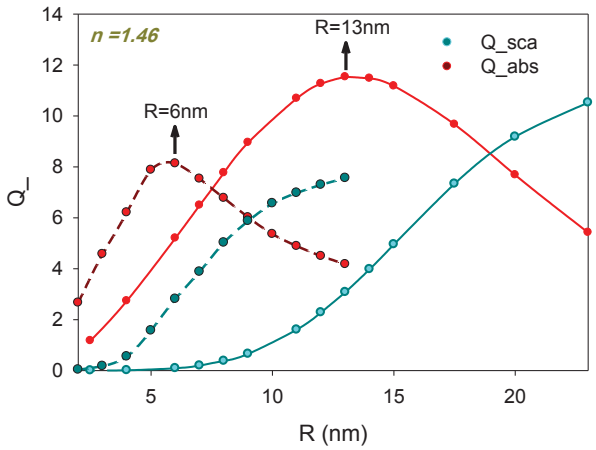

Figure 80| Plasmon absorption and scattering efficiencies (indicated in the legend) as a function of the sphere radius in: i) an isolated sphere (solid lines) ii) a planar array composed of 36 spheres at the interparticle separation $D = R/2$ (dashed lines). The coupling energy reduces the optimum sphere radius producing the highest absorption efficiency.

The coupling energy reduces the component particle size range, where the extinction process is dominated by the absorption as illustrated in Figure 80. The limit of this range is hence reduced from around 18nm to 8nm. Similarly, the optimum size of an isolated sphere $R = 13nm$, immersed in PDMS, is reduced to $R = 6nm$ due to the coupling energy initiated between the interacting particles.

8.2.2 Optimum size and dependence on the interparticle separation

Due to the coupling energy, the phase retardation is stimulated in ultrafine coupled particles at smaller interparticle separations. As a result, the quadrupole plasmon bands are observed in the absorption spectra of the planar arrays composed spheres of 2nm in radius at smaller interparticle separations $D \le R/4$ in a host medium of $n = 1.66$. By increasing the component particles size, the quadrupole plasmon bands eventually get more pronounced as can be seen in Figure 81a,b.

It has been found that the optimum size of an isolated nanoparticle decreases with refractive index of the host medium (see 4.3.1). In this section, the interparticle separation D is studied as another variable affecting the component optimum size in planar systems. Absorption spectra of the planar array, embedded in a host medium of refractive index $n = 1.66$, at various D are plotted in Figure 81.

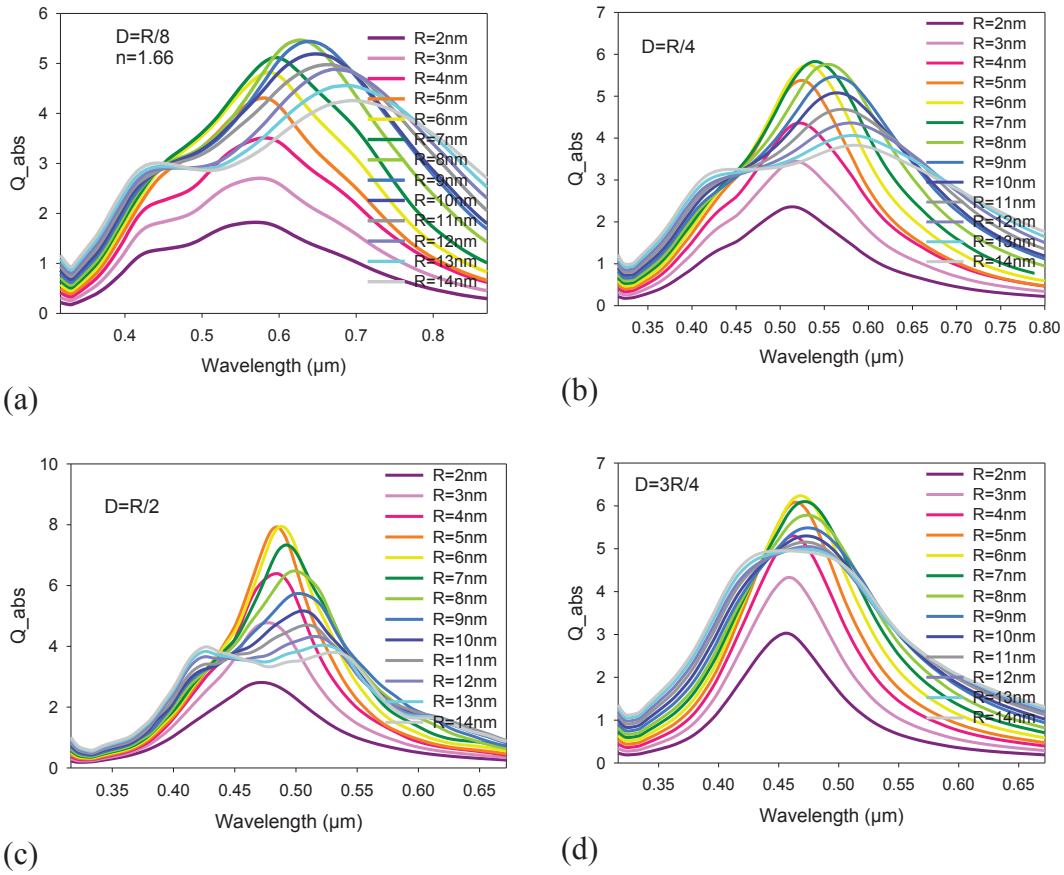

Figure 81| Absorption spectra of silver planar arrays, immersed in a host medium of refractive index $n = 1.66$, under parallel polarization, with various component sphere radius R (listed in the legends) and at different interparticle separation: (a) $D = R/8$,(b) $D = R/4$, (c) $D = R/2$ and (d) $D = 3R/4$.

The absorption efficiencies, extracted from Figure 81, are plotted as functions of the component sphere radius in Figure 82.

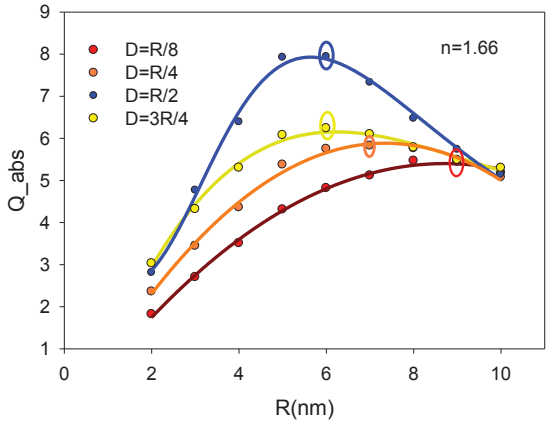

Figure 82| Absorption efficiency of the planar array as a function of the component sphere radius at various interparticle separations (listed in the legend). The dependency of the optimum size on the interparticle separation is effective when $D \le R/2$. A maximum absorption efficiency occurs at the optimum interparticle separation $D = R/2$ (in the near-field region) according to the optimum size $R = 6nm$.

Decreasing the interparticle separation $D \le R/2$, the absorption efficiencies reduce and the optimum size of the component particles increases up to $R = 9nm$ at $D = R/8$.

While a maximum absorption is observed at the optimum interparticle separation $D = R/2$ according to the optimum size $R = 6nm$, the optimum size at $D = 3R/4$ is also $R = 6nm$ but with a lesser absorption efficiency.

8.3 The effect of the dielectric environment on near-field interactions and the dipole plasmon coupling

8.3.1 Absorption cross-section

The maximum coupling is based on the most intense and sharpest plasmon band in the extinction spectrum [35]. Jain et al. reported that the host medium shields the interparticle

plasmon interactions [66], and plasmon coupling gets eventually shielded. On the other hand, the experiments achieved by Kinnan et al. [35] have revealed that the strength of the quadrupole coupling between component particles of a planar array increases in the medium with higher dielectric function. In this section, the effect of the dielectric host medium on the dipole coupling is investigated via absorption spectra of two-dimensional arrays of various nanospheres.

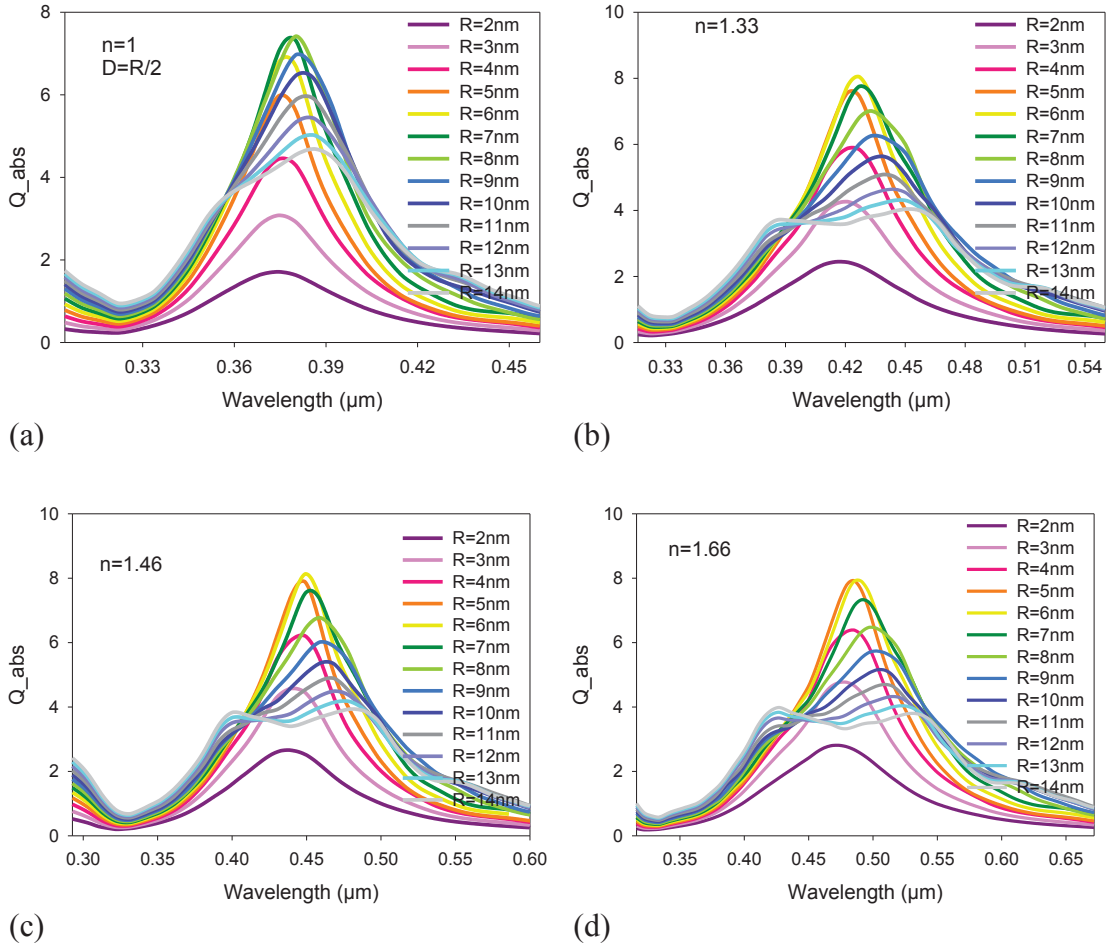

Figure 83| Absorption spectra of the planar arrays immersed in various materials of refractive indices (a) $n=1$ (b) $n=1.33$ (c) $n=1.46$ (d) $n=1.66$. The interparticle separation is set at $D=R/2$ and the component spheres size ranges between 2nm and 14nm (listed in the legends).

The absorption efficiencies of planar arrays of identical silver spheres of radii $2nm \le R \le 14nm$ are calculated at the interparticle separation $D = R/2$ in various host media of refractive indices $n = 1, 1.33, 1.46, 1.66$ as shown in Figure 83. The absorption efficiencies are plotted as a function of the refractive index of the host medium in Figure 84a. They show that the absorption efficiency is proportional to the component particle size when $R \le 4nm$, while it is reciprocally proportional to the component particle size of radius $R \ge 6nm$. When the particles arrays are immersed in a host medium of refractive index greater than unity, linear proportions are marked out as can be seen in Figure 84b when $n \ge 1.33$.

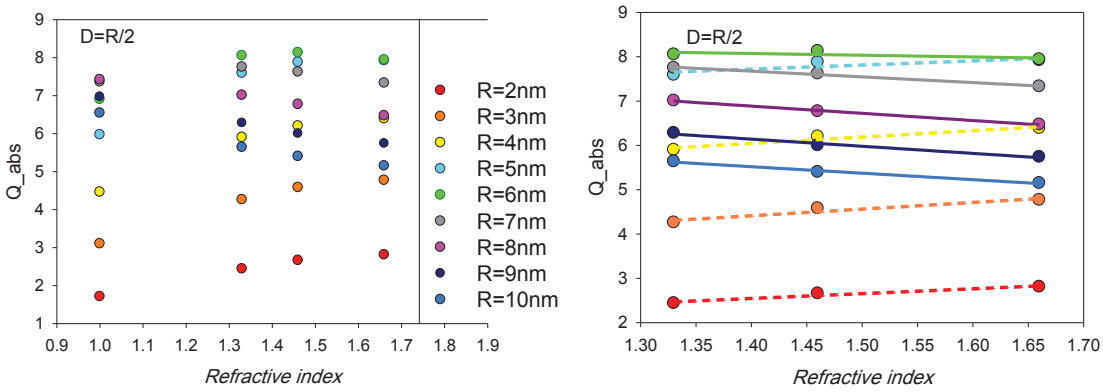

Figure 84| Absorption efficiency of the planar array as a function of the refractive index of the host medium, for different sizes of component nanospheres (listed in the legends). The interparticle separation is set at $D = R/2$.

The sensitivity of the absorption efficiency to the host medium is then plotted in Figure 85 as a function of the component particle size. It is found that the absorption is not uniformly affected by the refractive index n of the host medium over all the component particle sizes.

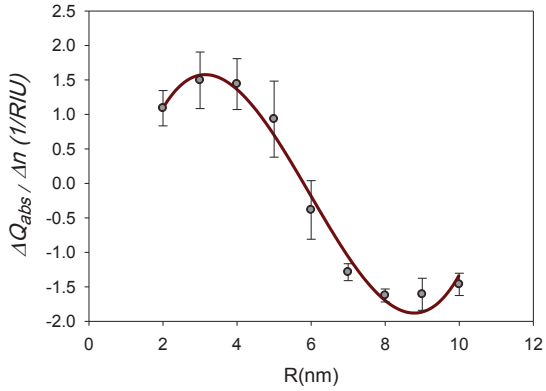

Figure 85| Absorption efficiency sensitivity of the planar array to the surrounding medium as a function of the component particle size. The error bars represent the error in the straight line fits in Figure 84b.

The absorption efficiency increases with n as long as $R < 6nm$, while it decreases for larger particles. In other words, the dielectric medium magnifies the absorption when the component particle radius $R \leq 5nm$ and the absorption cross-section reaches a maximum when $R \simeq 3nm$, which reflects the maximum coupling between particles, a contrary effect is observed when $R \geq 6nm$, where the host medium shields the local electric field and decreases the absorption cross-section to a minimum when $R \simeq 8nm$ as can be seen in Figure 85.

8.3.2 Resonance wavelength and the sensitivity to the host medium

The absorption spectra of the planar array of component spheres $R = 6nm$, immersed in various embedding materials, are calculated under p-polarized light at different interparticle separations. The plasmon coupling red-shift linearly increases with

increasing refractive index of the host medium at any interparticle separation as illustrated in Figure 86.

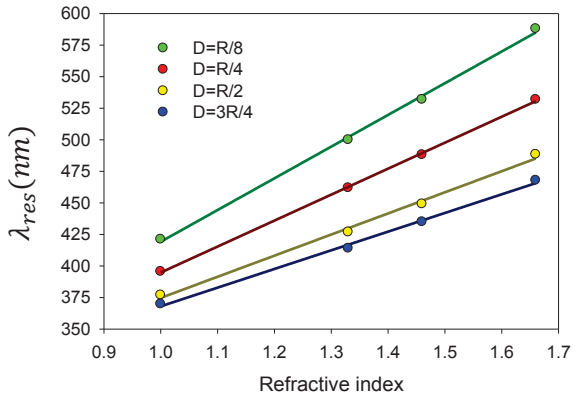

Figure 86| Resonance wavelengths of dipole bands of the planar array at different interparticle separations (listed in the legends) as a function of the refractive index of the host medium.

The slopes of these linear proportions increase inversely with interparticle separation. A larger magnitude of plasmon red-shift is hence exhibited at a smaller interparticle separation in response to a given increment in the medium refractive index.

Figure 87 represents the dipole plasmon resonance sensitivity of the planar array as a function of the interparticle spacing in units of sphere diameter. The sensitivity to the surrounding medium decays exponentially with increasing the interparticle separation, where the decay constant $b = 0.127$.

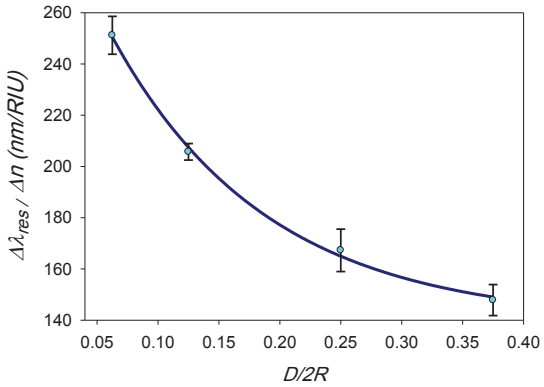

Figure 87| Plasmon resonance sensitivity of the planar array to the host medium as a function of the interparticle separation in units of component sphere diameter. The sensitivity decays near exponentially with $D/2R$ as seen from the fit (solid line) to the single-exponential decay with three parameters given by $y = y_0 + a\exp(-\frac{x}{b})$ where $b = 0.127 \pm 0.019$ and $a = 181.4$. The error bars represent the error in the straight line fits in Figure 86.

8.4 Resonance wavelength and the sensitivity to the component particle size

The sensitivity of the plasmon resonance wavelength to the size of the component spheres is studied in a host medium of refractive index $n = 1.66$ under p-polarized light at various interparticle separations, which are extended in near-field range from $D = R/8$ to $D = 3R/4$.

The dependency of the resonance wavelength of the planar array at different interparticle separations on the component sphere radius is shown in Figure 88.

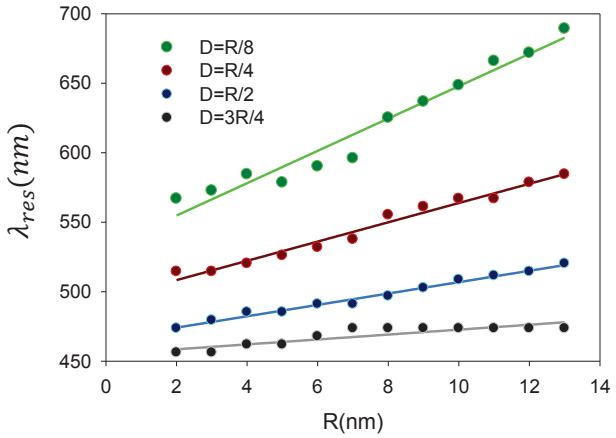

Figure 88| Resonance wavelengths of planar arrays at different interparticle separations (listed in the legend) as functions of the component sphere radius. The resonance wavelength at a specific D red-shifts according to a linear proportion with the component sphere radius, while the resonance wavelength of the array of a specific component sphere size red-shifts with decreasing.

The longitudinal dipole plasmon resonance wavelength of the array of a specific component sphere size is red-shifted to a lower energy with decreasing interparticle separation. The resonance wavelength of the plasmon coupling linearly increases with the component particle size at any interparticle separation D . The rate of the resonance wavelength red-shift is represented by the slopes of these straight lines as illustrated in Figure 88. This rate increases with decreasing interparticle separation D .

In order to deduce the variation of the resonance wavelength sensitivity to the component particles size with the interparticle separation, the ratio $\Delta\lambda_{res}/\Delta R$ is investigated and found to be exponentially decayed with the interparticle spacing scaled by the sphere diameter as can be seen in Figure 89.

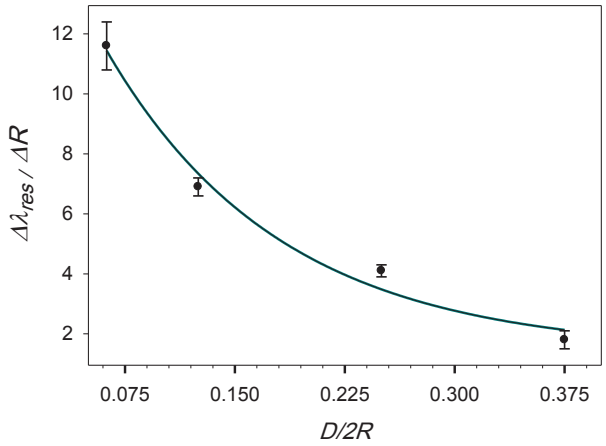

Figure 89| Plasmon resonance sensitivity of the planar array to the component sphere radius as a function of the interparticle separation in units of component sphere diameter. The solid line is fitted to the single-exponential decay $y = y_0 + a\exp(-x/b)$, where $b = 0.119 \pm 0.05$ and $a = 16.96$. The error bars represent the error in the straight line fits in Figure 88.

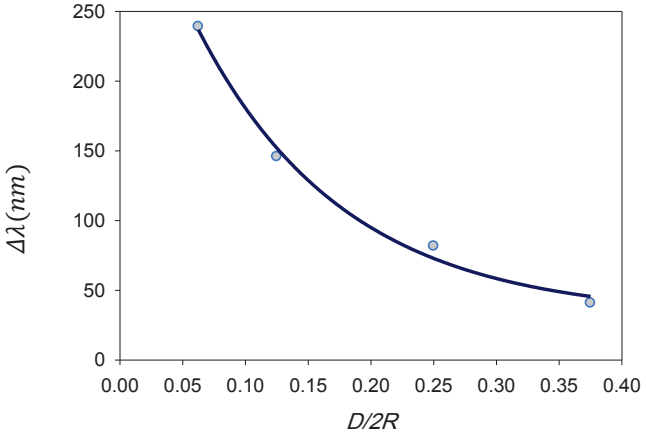

Figure 90| Plasmon shift as a function of the interparticle separation of the planar array in units of component sphere diameter, the chain composed of silver nanospheres of radius $R = 12nm$ is immersed in the host medium of refractive index $n = 1.66$. The solid curve is a regression of single-exponential decay function $y = y_0 + a\exp(-x/b)$ where $b = 0.118 \pm 0.034$, $a = 350$.

The same exponential trend is shown in Figure 90. The decay constant $b = 0.118$ is very close in value to the decay constant of the resonance sensitivity to both the host medium $b = 0.127$ and particle size $b = 0.119$. This result reflects the independency of the plasmon resonance shift from the host medium and the component particle size. By extending this result to other shapes and metals of the component particle we may get a universal scaling behaviour and a new "plasmon ruler" dealing with planar arrays of nanoparticles.

8.5 Two-dimensional and three- dimensional arrays of spherical silver nanoparticles

Introduction

We studied optical properties of three-dimensional multilayer systems [67]. The multilayer targets are set up of identical silver ultrafine nanospheres in such a way that the configuration of close-packed spheres characterizing each layer is still conserved in the cross-section of three-dimensional targets.

8.5.1 The DDA target geometry and orientation

The targets are represented by either a monolayer (planar) system or by a three-dimensional multilayer system. A hexagonal array, composed of 61 identical close-packed spheres of $5nm$ in diameter, stands for each layer as illustrated in Figure 91. The interparticle spacing in all these targets is set to $D = R/2 = 1.25nm$.

With the purpose of quantitatively getting reliable results, the number of dipoles generating each sphere has been ensured to be large enough, 2000 dipoles [68].

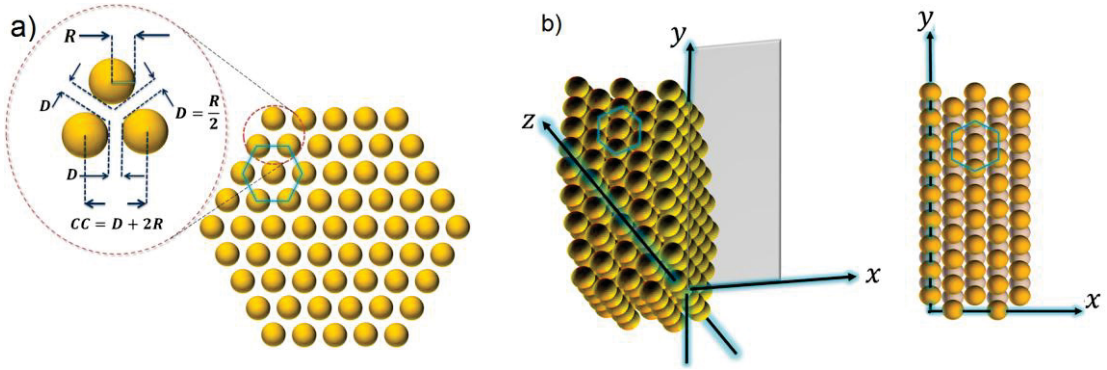

Figure 91| Schematic representation of the geometry of a) the planar target, composed of 61 mono-sized spheres of radius 5nm arranged in a hexagonal array, at interparticle separation $D = R/2$ b) a multilayer three-dimensional target, composed of nanospheres, arranged spatially in five hexagonal planer layers, as illustrated in the cross-section scheme to the right.

The incident light is linearly polarized in the y axis direction while it propagates along the x axis direction as shown in Figure 92. The incident angle can be changed by rotating the target plane around the z-axis.

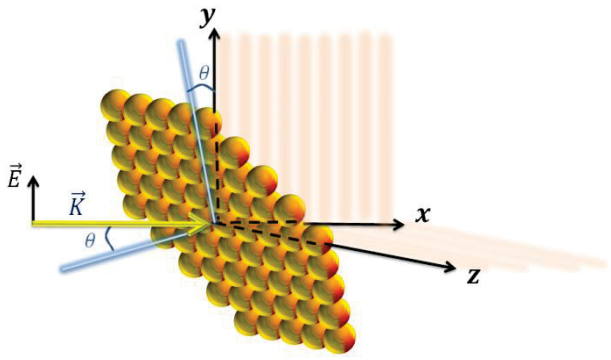

Figure 92| Schematic illustration of the incident light propagation direction ($\vec{K}$) and polarization ($\vec{E}$) with respect to the planar array.

8.5.2 The effect of the three-dimensional particles configuration on the dipole plasmon coupling

At normal incidence ($\theta = 0^o$), the planar target is oriented parallel to the electric field of the incident radiation. Only the longitudinal plasmon band appears at 2.6eV, showing the optical surface isotropy, experienced be the incident electric filed, as illustrated in Figure 93. On the other hand, when the electric field of the incident light is perpendicular to the surface of the monolayer target at the parallel incidence ($\theta = 90^o$), the transverse plasmon band emerges at (3.5 eV) as shown in Figure 93. However, when the incidence angle ranges between $\theta = 0^o$ and $\theta = 90^o$, the two bands arise due to the projections of the incident electric field on both directions; perpendicular and parallel to the planar target. Subsequently, the amplitude of each band depends on the corresponding electric field component received, which is controlled by the angle of incidence. Obviously, as the incident angle progressively increases, the amplitude of the longitudinal band gradually decreases while the amplitude of the other developing band grows.

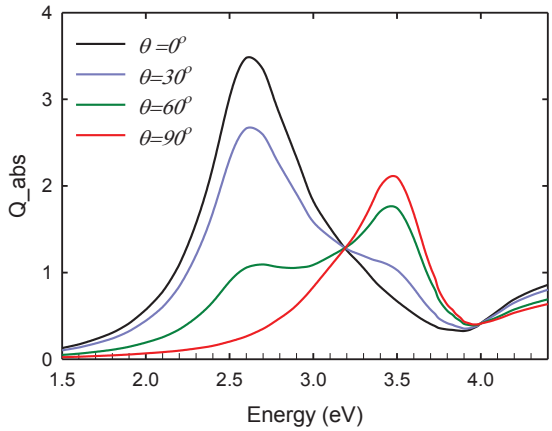

Figure 93| Dependency of absorption spectra on the incident angle (listed in the legend).

Three-dimensional systems of up to ten layers are simulated; the layers are combined together in such a way that the interparticle distance $D = 1.25nm$ was spatially conserved. In comparing with the two-dimensional system, the absorption spectra revealed significant changes on the dipole plasmon resonance bands.

At normal and parallel incidences, Figure 94 shows that the longitudinal plasmon resonance wavelength is blue-shifted while the other is red-shifted in response to expand the target in the third dimension. Both of the resonance wavelengths are displaced towards each other as the size of the target grows in the third dimension and they are expected to reach the same energy while the absorption efficiency of each gradually increases.

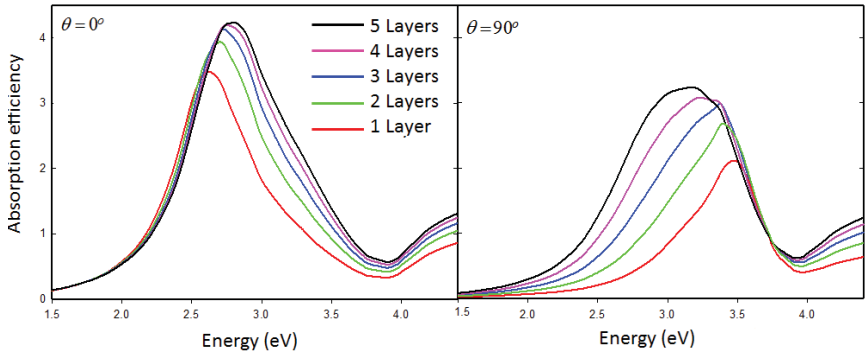

Figure 94| Absorption spectra, calculated at the normal ($\theta = 0^o$) and parallel ($\theta = 90^o$) incidences, of various targets. The monolayer target, composed of a hexagonal array of 61 close-packed silver nanospheres, is afterwards multiplied into multilayer three-dimensional target of 2, 3, 4 and 5 layers (listed in the legend).

Figure 95 shows the behaviour of the longitudinal and transverse plasmon resonance energies at normal and parallel incidences. The longitudinal plasmon resonance undergoes a blue-shift as the target extend in the third dimension until the five-layer target is formed, then peak position remains at the same energy and is not affected by any additional extension. On the other hand, the transverse plasmon resonance energy is progressively affected as the target spatially grows layer by layer. Subsequently, the both of the peaks coincide at the same resonance energy (2.82eV), and a slight deference in the amplitude is observed in favor of the developed longitudinal band due to geometrical considerations.

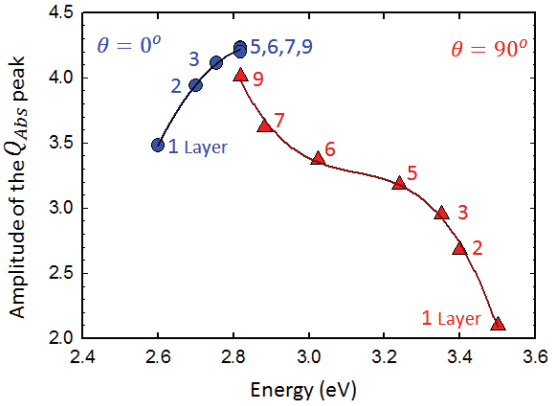

Figure 95| Schematic diagram shows the behaviour of the resonance energy and the absorption efficiency in response to the stepwise expansion of the target in the third dimension under normal (blue circles) and parallel (red triangles) incidences. The blue line is fitted by a polynomial quadratic function whereas the red solid line fits a polynomial cubic function.

At oblique angles of incidence, the two orthogonal components of the electric field are respectively parallel and perpendicular to the surface of two-dimensional target, and change in importance as the angle of incidence grows. The two plasmon resonance bands consequently evolve through the absorption spectrum, providing necessary information on the optical surface isotropy. The features of the two well-separated peaks emerged become less definable after doubling the system size. While the longitudinal resonance energy is blue shifted, the peak related to the transverse band tends to have a slight red shift and the absorption efficiencies of both are considerably increased as shown in Figure 96. Tripling the two-dimensional monolayer target, both of the peaks are integrated into the asymmetrical curve. Both of the peak positions are displaced towards each other and superimposed in a smooth curve as the two-dimensional monolayer target is spatially quadrupled when $\theta = 60^{o}$.

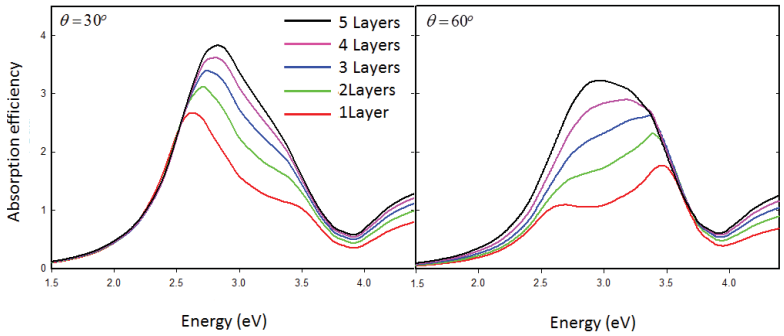

Figure 96| Absorption spectra at oblique angles $\theta = 30^{o}, 60^{o}$ for various targets. The two-dimensional hexagonal array was stepwise multiplied into multilayer three-dimensional targets of up to 5 layers.

While the target is multiplied in the third dimension, the optical anisotropy experienced by the perpendicular electric field component at oblique incidence, observed in a two-dimensional system, diminishes gradually.

CHAPTER 9

Conclusions

We aimed to develop a systematic understanding of the effect of the host medium and the particle size on the plasmon parameters. Assemblies of interacting silver nanoparticles, arranged in one-dimensional and two-dimensional arrays at various interparticle separations, have been studied. The results found in our work offer strong guidelines for relating the different key variables with each other. This provides us with a clear view and a more precise prediction tool for the optical response of a desired system, which can be advantageously exploited for different applications. The effect of the contact area between a deposited single silver nanoparticle and a substrate in particular has been studied in different environments.

9.1 Substrate effect

The dipole plasmon resonance band, excited in an isolated nanosphere, is found to be red-shifted in a sphere-like particle when the cut-facet area increases and the symmetry of the sphere is broken, while a small shoulder emerges at a higher energy in a small plasmon band incorporated into the tail of the dipole plasmon band.

Inserting a substrate, the plasmon resonance band, observed in isolated silver particles, is split into two well-defined and separated plasmon bands: the dipole and shape plasmon bands at lower and higher energy, respectively. In addition, the substrate plasmon band with a small relative intensity emerges due to the bonding between the substrate and the

deposited silver particle. The position of the substrate band is found to be dependent on the contrast between the refractive indices of the substrate and the ambient. For instance, it has been found that when the refractive index of the substrate, $n_{substrate} = 1.92$, is around or less than the refractive index of the ambient, n_{medium}, the substrate plasmon bands are locate at higher energies. Decreasing n_{medium}, the shape plasmon band is blue-shifted until it reaches the substrate band, giving a broadened band when $n_{medium} = 1.48$. Afterwards, the shape plasmon band is progressively blue-shifted and gets separated from the substrate plasmon band, which is now located between the shape and the dipole plasmon bands.

The substrate increases the red-shift of the dipole plasmon band with increasing contact area, which is related to the sphere-like height. The magnitude of this shift is found to change linearly with the height of particles.

However, the shape plasmon band is found to be less sensitive to the contact area, and contrary to the case of the dipole band, it is blue-shifted with increasing contact area. The resonance wavelength of the shape band also changes linearly with the particle height.

The thickness of the substrate does not affect the resonance wavelength of the shape and substrate plasmon bands, whereas the dipole plasmon resonance wavelength is found to red-shift slightly with the substrate thickness.

The effect of the substrate material on the plasmon resonance is investigated for a sphere-like particle, defined by the contact angle $\alpha = 123.06^{o}$, when the refractive index of the host medium is set to unity. The resonance wavelength of the dipole plasmon band is

found to red-shift linearly with the dielectric constant of the substrate, while the corresponding absorption efficiency is reduced linearly with the substrate refractive index.

The substrate effect is revealed in a single band when $n_{medium} < n_{substrate}$. Increasing n_{medium}, the contrast between the refractive indices of the substrate and medium decreases and the resonance wavelength of the shape plasmon band red-shifts faster than that of the dipole band. The spectral range separating them decreases linearly with increasing refractive index of the host medium.

When $n_{medium} > n_{substrate}$, the multipolar excitation due to the substrate effect emerges in two well-separated substrate plasmon bands. The peak position at the higher energy is independent of the refractive index of the host medium while the other substrate plasmon band, located at lower energy, is red-shifted with increasing refractive index of the host medium. The resonance wavelength of the dipole plasmon band red-shifts much faster than that of the shape band, and the spectral range between their peaks increases linearly with increasing refractive index of the host medium.

9.2 One-dimensional linear chain

The resonance wavelength and the width of the dipole band mode in the silver chain, composed of eight spheres, are tested so that the results can be generalized to any linear chain constituting of a larger number of silver nanospheres.

9.2.1 Under parallel polarization

The universal scaling behaviour of the distance decay of plasmon coupling in metal nanoparticle pairs was presented by Jain et al. (see Eq. 50). The universal fractional plasmon shift decay constant $b = 0.23$ was established originally for a pair of gold nanospheres of radii 21nm. The decay constant was considered independent from the nanoparticle size, metal type, shape or the host medium according to the authors. However, in a silver chain the fractional plasmon shift as a function of the interparticle separation in various environments $n = 1, 1.33, 1.46, 1.66$ is found to vary slightly according to the respective decay constants $b = 0.185, 0.206, 0.221, 0.235$.

Based on these observations, the plasmon resonance sensitivity ($\Delta\lambda_{res} / \Delta n$) to the surrounding medium as a function of the interparticle separation in units of component sphere diameter is investigated. While the same universal exponential decay trend was observed, the calculated decay constant $b = 0.268$ is somewhat different from the decay constant of the fractional plasmon shifts. This difference reflects a slight dependency of the resonance plasmon shift $\Delta\lambda$ on the environment. Compared to the sensitivity of the gold nanosphere presented by Jain et al., the sensitivity of the silver chain is enhanced by roughly 1.5 times. The sensitivity of a silver chain at the interparticle separation $D = 0.2R, 3R$ is estimated to be around 257nm, 114nm per unit refractive index (RIU) of the surrounding medium.

The plasmon resonance sensitivity to the component sphere radius ($\Delta\lambda_{res} / \Delta R$) is also fitted to the single-exponential decay as a function of the interparticle separation in units of component sphere diameter. The calculated decay constant $b = 0.413$ is found to be

very different and larger than the one attributed to ($\Delta\lambda_{res}/\Delta n$), which reflects an obvious dependency of the plasmon shift on the component particle size. The sensitivity $\Delta\lambda_{res}/\Delta R$ decays exponentially from 4.5 nm in λ_{res} per nm change in radius to 1.2 nm, when the interparticle separation increased from $D = R/8$ to $D = 1.5R$.

9.2.2 Under perpendicular polarization

We reported that the plasmon resonance sensitivity ($\Delta\lambda_{res}/\Delta n$) decays exponentially with decreasing interparticle separation contrary to the previous trend with a decay constant of $b = 0.45$. The variation of the sensitivity to the host medium with the interparticle separation is favored by an enhancement from 83nm to 103nm, when the interparticle separation $D = 0.2R$ increases to $D = 3R$.

The sensitivity to the component sphere size is found to slightly decrease linearly with the interparticle separation in units of component sphere diameter. The linear decay with the slope $a = -0.2343$ reflects a weak sensitivity $\Delta\lambda/\Delta R$, which linearly decays from 0.88 nm in λ_{res} per nm change in radius to 0.72 nm when the interparticle separation increase from $D = R/8$ to $D = 1.5R$.

For incident polarizations parallel and perpendicular to the chain axis, The dipole plasmon bandwidth ($FWHM$) as a function of the component sphere radius is fitted to an exponential-linear combination involving four parameters $y = y_0 + a\exp(-x/b) + cx$

.

9.3 Two-dimensional planar array

In two-dimensional arrays consisting of 36 identical silver nanospheres uniformly arranged in square areas, the optimum size of the component particle is found to vary with the interparticle separation when $D \le R/2$, i.e., the optimum size increases from $R = 6nm$ to $R = 9nm$ as the interparticle separation decreases from $D = R/2$ to $D = R/8$, while a favourable interparticle separation producing a maximum absorption efficiency is specified at $D = R/2$ in the embedding medium of refractive index $n = 1.66$.

The absorption efficiency is enhanced by the host medium when $R < 6nm$, while it is reduced for larger particles. In other words, the medium magnifies the local electric field between interacting nanoparticles leading to a larger absorption cross-section when the component particle radius $R \le 5nm$, and the absorption cross-section reaches a maximum when $R \simeq 3nm$. However, a contrary effect is observed when $R \ge 6nm$, the host medium shields the local electric and decreases the absorption cross-section to a minimum when $R \simeq 8nm$. This systematic study can be exploited to find the optimum size with the highest absorption cross-section for ultrafine silver nanoparticles applications distributed on a plane.

The resonance wavelength sensitivity to the surrounding medium as a function of the interparticle separation is found to decay near exponentially from 251nm to 148nm as the interparticle separation increases from $D = R/8$ to $D = 3R/4$. The decay constant of the single-exponential decay is $b = 0.127$, which reflects a faster decay rate than that noticed in linear chains ($b = 0.268$).

The resonance wavelength sensitivity to the component sphere radius shows the same exponential trend, and the decay constant $b = 0.119$ is very close in value to that of the fractional plasmon shift $b = 0.118$ and to the host medium sensitivity $b = 0.127$. These similar values express the independency of the plasmon resonance shift from the host medium and the component particle size. If we can extend this result to other shapes and materials of the component particle, we will get a universal scaling behaviour of the distance decay and a new "plasmon ruler" governing planar arrays of nanoparticles.

9.4 Configuration effect

In a planar system composed of well-separated linear chains placed in arbitrary directions, each particle is linearly placed between two direct neighbouring particles, and hence the system can be simplified by a two-dimensional array aligned on a square circumference. The dipole plasmon coupling resonance is revealed through two well-separated plasmon coupling bands when $D \le R$. The longitudinal plasmon band at a longer resonance wavelength is due to the electric field component that is parallel to the chains axis, while the transverse plasmon band, excited by the other perpendicular field component, appears at a shorter resonance wavelength. The spectral distance between those two wavelengths is mainly attributed to the longitudinal resonance wavelength as it is strongly sensitive to the interparticle separation, both of the plasmon peak positions move towards each other until they get incorporated into a single broadened band as demonstrated when $D = 3R$.

Transporting to the two-dimensional system of 36 nanospheres, aforementioned, each inner particle is surrounded by four direct neighbouring particles. The dipole plasmon bandwidth is found to be broadened, centered at the longitudinal resonance wavelength, as the enhanced local fields surrounding the contiguous particles overlap.

In three-dimensional systems consisting of ultrafine spherical silver particles that are hexagonally close-packed, each particle is surrounded by twelve direct neighbouring particles. When the target spatially grows layer by layer, the longitudinal plasmon band undergoes a blue-shift, while the transverse plasmon band is progressively red-shifted. Eventually, the longitudinal and transverse plasmon bands, observed in a one layer, are incorporated into one broadened well-defined dipole plasmon resonance band.

9.5 Future work

The work in this thesis can be easily extended to include other metals of interest such as gold, copper, tin and aluminium. It can also be applied to other shapes of particles, in particular nanorods, nanocubes, nanobars, nanoellipsoids and nanotriangles. In fact, we already had extended the calculations to gold and silver nanocubes and nanobars and some results are presently in press [69]. The results found will help us understand better the interaction of light with these nanostructures and their various configurations. They will also be an excellent basis for optimization of optical properties for applications such as biosensing [70] and solar cells [71].

BIBLIOGRAPHY

[1] Truong, V. V.; Scott, G. D. J. Opt. Soc. Am. 1977, 67, 502-510.

[2] Truong, V. V.; Scott, G. D. J. Opt. Soc. Am. 1976, 66, 124-131.

[3] Noguez, C. J. Phys. Chem. C 2007, 111, 3806-3819.

[4] Malinsky, M. D.; Kelly, K. L.; Schatz, G. C.; Van Duyne, R. P. J. Am. Chem. Soc. 2001, 123, 1471-1482.

[5] Yang, P.; Portalès, H.; Pileni, M. J . Phys. Chem. C 2009,113, 11597-11604.

[6] Gunnarsson, L.; Rindzevicius, T.; Prikulis, J.; Kasemo, B.; Kall, M.; Zou, S. L.; Schatz, G. C. J. Phys. Chem. B 2005, 109, 1079-1087.

[7] Bouhelier, A.; Bachelot, R.; Im, J. S.; Wiederrecht, G. P.; Lerondel, G.; Kostcheev, S.; Royer, P. J. Phys. Chem. B 2005, 109, 3195-3198.

[8] Zou, S. L.; Janel, N.; Schatz, G. C. J. Chem. Phys. 2004, 120, 10871-10875.

[9] Bader, G.; Ashrit, P. V.; Girouard, F. E.; Truong, V. V. J. Appl. Phys. 1990, 68, 1820-1824.

[10] Jain, P. K.; Huang, W. Y.; El-Sayed, M. A. Nano Lett. 2007, 7, 2080-2088.

[11] Jain, P. K.; El-Sayed, M. A. Nano Lett. 2008, 8, 4347-4352.

[12] Jain, P. K.; El-Sayed, M. A. J. Phys. Chem. C 2008,112, 4954-4960.

[13] Mie, G. Ann. Physik IV 1908, 25, 377-445; an English translation of this paper was provided by the British Library.

[14] Kreibig, U.; Vollmer, M. Optical Properties of Metal Clusters; Springer Series in Materials Science 25; Springer-Verlag: New York, 1995, p.23.

[15] Willets, K. A.; Van Duyne, R. P. Annu. Rev. Phys. Chem. 2007, 58, 267-297.

[16] Kelly, K. L.; Coronado, E.; Zhao, L. L.; Schatz, G. C. J. Phys. Chem. B 2003, 107, 668-677.

[17] Gonzalez, A. L.; Reyes-Esqueda, J. A.; Noguez, C. J. Phys. Chem. C 2008, 112, 7356-7362.

[18] Zhang, J. Z.; Noguez, C. Plasmonics 2008, 3,127-150.

[19] Hodak, J. H.; Henglein, A.; Hartland, G. V. J. Phys. Chem. B 2000, 104, 9954-9965.

[20] Noguez, C. Opt. Mat. 2005, 27, 1204-1211.

[21] Sönnichsen, C.; Franzl, T.; Wilk, T.; Von Plessen, G.; Feldmann, J.; Wilson O.; Mulvaney, P. Phys. Rev. Lett. 2002, 88, 077402, 1-4.

[22] Kreibig, U.; Vollmer, M. Optical Properties of Metal Clusters; Springer Series in Materials Science 25; Springer-Verlag: New York, 1995, p 33.

[23] Link, S.; El-Sayed, M. A. J. Phys. Chem. B 1999, 103, 4212-4217.

[24] Coronado, E. A.; Schatz, G. C. J. Chem. Phys. 2003, 119, 3926-3934.

[25] Moroz, A. J. Phys. Chem. C 2008, 112, 10641-10652.

[26] El-Sayed, M. A. Acc. Chem. Res. 2001, 34, 257-264.

[27] Ashcroft, N. W.; Mermin, N. D. Solid State Physics. Philadelphia; Saunders College, 1976, P 3-6.

[28] Kreibig, U.; Vollmer, M. Optical Properties of Metal Clusters; Springer Series in Materials Science 25; Springer-Verlag: New York, 1995, p 14-15.

[29] Kreibig, U.; Vollmer, M. Optical Properties of Metal Clusters; Springer Series in Materials Science 25; Springer-Verlag: New York, 1995, p 31.

[30] Kumbhar, A. S.; Kinnan, M. K.; Chumanov, G. J. Am. Chem. Soc. 2005, 127, 12444-12445.

[31] Evanoff, D. D.; Chumanov, G. J. Phys. Chem. B 2004, 108, 13948-13956.

[32] Evanoff, D. D.; Chumanov, G. J. Phys. Chem.B 2005, 6, 1221-1231.

[33] Evanoff, D. D.; Chumanov, G. J. Phys. Chem. B 2004, 108, 13957-13962.

[34] Bohren, C. F.; Huffman, D. R. Absorption And Scattering of Light by Small Particles; Wiley: New York, 1983; p 145.

[35] Kinnan, M. K.; Kachan, S.; Simmons, C. K.; Chumanov, G. J. Phys. Chem. C 2009, 113, 7079-7084.

[36] Novo, C.; Funston, A. M.; Pastoriza-Santos, I.; Liz-Marzan, L. M.; Mulvaney, P. J. Phys. Chem. C 2007, 112, 3-7.

[37] Malynych, S.; Chumanov, G. J. Opt. A: Pure Appl. Opt. 2006, 8, S144 - S147.

[38] Yang, P.; Portalès, H.; Pileni, M. P. Phys. Rev. B 2010, 81, 205405, 1-8.

[39] DeVoe, H. J. Chem. Phys. 1964, 41, 393-400.

[40] Purcell, E. M.; Pennypacker, C. R. Astrophys. J. 1973, 186, 705-714.

[41] Yung, Y. L. Appl. Opt. 1978, 17, 3707-3709.

[42] (a) Draine, B. T.; Goodman, J. J. Astrophys. J. 1993, 405, 685-697.

(b) Draine, B. T.; Flatau, P. J. Program DDSCAT; Scripps Institute of Oceanography, University of California: San Diego, CA.

[43] http://code.google.com/p/ddscat/

[44] Draine, B. T.; Flatau, P. J. J. Opt. Soc. Am. A 1994, 11, 1491-1499.

[45] Sosa, I. O.; Noguez, C.; Barrera, R. G. J. Phys. Chem. B 2003,107, 6269-6275.

[46] Draine, B.T.; Flatau, P.J. User Guide for the Discrete Dipole Approximation Code DDSCAT7.1 2010, http://arxiv.org/abs/1002.1505v1.

[47] (PBCGS2) is based on the Ph. D. thesis by:

(a) Sleijpen, G. L. G.; van der Vorst, H. A.; Fokkema, D. R. "BiCGStab(L) and Other Hybrid Bi-CG Methods", Numerical Algorithms 1994, 7, p 75-109.

(b) Sleijpen, G. L. G.; van der Vorst, H. A. "An Overview of Approaches for the Stable Computation of Hybrid BiCG Methods", Applied Numerical Mathematics: Transactions f IMACS 1996,19, p 235-54.

[48] Draine, B. T.; Goodman, J. J. Astrophys. J. 1993, 405, 685-697.

[49] Purcell, E. M. Electricity and Magnetism; Mc Graw-Hill: New York, 1963.

[50] Goodman, J. J.; Draine, B. T.; Flatau, P. J. Opt. Lett. 1991, 16, 1198-1200.

[51] Kreibig, U. J. Phys. F: Met. Phys. 1974, 4, 999-1014.

[52] Coronado, E. A.; Schatz, G. C. J. Chem. Phys. 2003, 119, 3926-3934.

[53] Ehrenreich, H.; Philipp, H. R. Phys. Rev. 1962, 128, 1622-1629.

[54] Johnson, P. B.; Christy, R. W. Phys. Rev. B 1972, 6, 4370-4379.

[55] http://www.philiplaven.com/mieplot.htm

[56] McFarland, A. D.; Van Duyne, R. P. Nano Lett. 2003, 3, 1057-1062.

[57] Refractive Index Database <http://refractiveindex.info>. Retrieved on Jan. 01, 2011.

[58] Bass, M.; DeCusatis, C.; Li, G.; Mahajan, V. N.; Enoch, J.; Stryland, E. V. Handbook of Optics; 3rd edition, Vol. 4. McGraw-Hill: New York, 2009.

[59] Gluodenis, M.; Foss, C. A. J. Phys. Chem. B 2002, 106, 9484–9489.

[60] Wang, S.; Pedersen, D. B. J. Phys. Chem. C 2010, 114, p 2861-2866

[61] Reinhard, B. M.; Siu, M.; Agarwal, H.; Alivisatos, A. P.; Liphardt, J. Nano Lett. 2005, 5, 2246-2252.

[62] Pinchuk, A. O.; Schatz, G. C. Mater. Sci. Eng. B 2008, 149, 251-258.

[63] Pinchuk, A. O.; Schatz, G. C. Appl. Phys. B 2008, 93, 31-38.

[64] Ezequiel, R. E.; Coronado, E. A. J. Phys. Chem. C 2010, 114, 3918-3923.

[65] Russier, V.; Pileni, M. P. Surf. Sci. 1999, 425, 313-325.

[66] Jain, P. K.; Eustis, S.; El-Sayed, M. A. J. Phys. Chem. B 2006, 110, 18243-18253.

[67] Wahbeh, M.; Alsawafta, M.; Misra, S. K.; Truong, V. V. Proc. SPIE 2011, 8007, 80071I.

[68] Portales, H.; Pinna, N.; Pileni, M. P. J. Phys. Chem. A 2009, 113, 4094-4099.

[69] Alsawafta, M.; Wahbeh, M.; Truong, V. V. Journal of Nanomaterials 2011. In Press.

[70] See, for example, Fida, F.; Varin, L.; Badilescu, S.; Kahrizi, M.; Truong, V. V. Plasmonics, 2009, 4, 201-207.

[71] See, for example, Mamoud, A.; Zhang, J. ; Baral, J. ; Izquierdo, R.; Ma, D.; Packirisamy, M.; Truong, V. V.; Proc. SPIE 2011, 8007, 80071V.